THE MICROMECHANISMS OF CEMENTED CARBIDE CUTTING TOOL WEAR

By

SHRIHARSHA SHARADCHANDRA INGLE

A Thesis

Submitted to the School of Graduate Studies

in Partial Fulfilment of the Requirements

for the Degree

Doctor of Philosophy

McMaster University

THE MICROMECHANISMS OF CEMENTED CARBIDE CUTTING TOOL WEAR

"I hate quotations"

... Ralph Waldo Emerson

Dedicated to my parents,

Sharadchandra and Jyotsna Ingle.

DOCTOR OF PHILOSOPHY (1993) McMASTER UNIVERSITY

(Materials Engineering) Hamilton, Ontario

TITLE : The Micromechanisms of Cemented Carbide Cutting Tool Wear

AUTHOR : Shriharsha Sharadchandra Ingle, B.Tech.
(Banaras Hindu University)

SUPERVISORS : Dr. D.A.R. Kay
Dr. S.V. Subramanian

NUMBER OF PAGES : xv, 202

ABSTRACT

Instrumental Neutron Activation Analysis has been used to measure the materials loss from the cutting tools during machining. Using this technique, the contributions from mechanical and dissolution wear have been individually quantified, and the dominance of dissolution wear during the high speed machining of a medium carbon steel using uncoated tungsten carbide-cobalt tools has been established.

SIMS analysis of the chip material next to the tool-chip interface showed concentration profiles of tungsten and cobalt to a depth of about 0.5 micron. The maximum concentration of tungsten is seen to increase with cutting speed, in agreement with the principle of dissolution wear. There is a consistency between the results of the two independent analytical techniques (INAA and SIMS), used to study the dissolution wear process.

The microstructure of the secondary shear zone of the chips was studied by Scanning Electron Microscopy and Transmission Electron Microscopy. In the immediate vicinity of the tool-chip interface of water quenched chips, a changed ultrafine equiaxed grain structure (0.2 μm) was observed. Enhancement of the diffusivity of tungsten resulting from this ultrafine structure was estimated and incorporated into a thermokinetic model for dissolution

wear. However, the dissolution wear predicted by the model was lower than the experimentally measured values at all the speeds; e.g. the predictions based on complete austenitization and a 0.2 μm grain size in the immediate vicinity of the tool-chip interface accounted for 34.7% of the experimentally measured value at 240 m/min. It is proposed that entire dissolution wear could possibly be accounted for by the thermokinetic model based on further enhancement in diffusivity due to grain boundary migration or the presence of approximately 10nm size grains during the tool-chip contact.

The joint role of solubility of the tool material into the chip and the enhanced diffusivity has been shown to be important in determining dissolution wear, and the performance of HfN coated tools is discussed in light of the above model.

The 'hard' alumina inclusions lead to an increase in the mechanical wear rate of the cutting tool, and this effect is demonstrated quantitatively by the INAA technique.

ACKNOWLEDGMENTS

The author wishes to express sincere thanks to his supervisors, Drs. D.A.R. Kay and S.V. Subramanian, and the members of his supervisory committee, Drs. G.R. Purdy and R. Sowerby for their guidance and support throughout the course of this project. Useful communications from Dr.E.M. Trent, University of Birmingham, UK are gratefully acknowledged.

The help extended to me by Ms. Alice Pidruczny in radioanalytical work deserves a special mention. Help from Dr. M.V. Ravichandran in electron analytical work is gratefully acknowledged. I would also like to thank Mr. David Buryta and Mr. Paul Gatt for their assistance in carrying out the wear tests. Thanks are also due to Mr. Gary Mount for help with the SIMS analysis. Helpful discussions with Dr. Om Prakash are also thankfully acknowledged.

The author is grateful to Lake Ontario Steel Company, Whitby, Ontario for supplying the steel and to Teledyne Cutting Tools, USA for providing the HfN tool coatings.

I would like to thank the Manufacturing Research Corporation of Ontario for funding this work. Graduate scholarship offered by the Department of Materials Science and Engineering is also thankfully acknowledged.

Finally, and most importantly, I would like to thank my parents for their kind support, despite being far away.

TABLE OF CONTENTS

List of Figures

List of Tables

CHAPTER 1 : INTRODUCTION

The wear of cutting tools has been one of the most extensively researched fields in engineering for the last 40 years. The study of tool wear involves a fundamental understanding of the mechanics of machining, the dynamic plasticity of materials, thermodynamics, kinetics and heat transfer. In recent years new tool materials and wear resistant coatings have been developed. The literature is full of studies outlining the performance of a variety of cutting tools under various cutting conditions, but the rationalization of results is inadequate. In most of these studies tool wear is defined in terms of crater wear, described by the maximum crater depth (d_{max}), and flank wear, described by the width of flank wear land (V_B). Most crater and flank wear models are based on these parameters, which, although easy to measure, are indirect. The technique used in this investigation was based on the premise that measurements of actual amounts of material lost from the tool were essential to the establishment of a reliable tool wear database.

To generate such a database, a basic K-11 grade uncoated carbide tool (97 % WC, 2.6 % Co, 0.4 % Ta(Nb)C) was selected to machine a Ca-treated AISI 1045 grade steel

workpiece material at high cutting speeds. Ca-treated steel was used to minimize the mechanical wear of the cutting tools. Material lost from the tool and transferred into the chips was quantitatively measured by Instrumental Neutron Activation Analysis (INAA) after irradiation of the chips in McMaster University's nuclear reactor. Since, significant crater wear of K-11 grade tool occurs rapidly, the duration of wear tests could be as short as 30 seconds. Thus, the total quantity of chips to be collected and analyzed using INAA was considerably reduced. The analysis of experimental data showed that dissolution wear was the dominant wear mechanism at high cutting speeds. The performance of HfN coated tools and the Ta(Nb)C alloyed K-11 tools were also studied, and their performance related to the dissolution wear model. These results are presented in Chapter 4.

While a diffusional hypothesis for crater wear of cemented carbide tools was proposed many years ago, experimental evidence of the presence of tool constituents in atomic form in the chip material and an in-depth analysis of their concentration profiles was missing. In this investigation, the concentration profiles of tungsten and cobalt in the chip have been obtained using a Secondary Ion Mass Spectrometer [SIMS]. The Analysis of the SIMS results has been presented in Chapter 5, which deals with the thermokinetic modeling of dissolution wear. A critical comparison between the thermokinetic models based on

enhanced diffusivities of tungsten next to the interface and the convective model for the transport of tungsten away from the tool-chip interface is presented in Chapter 6 (Discussion). In the same chapter, the choice of the experimental technique used to generate the quantitative tool wear database has been justified and the analysis of dissolution wear mechanism is given.

Conclusions based on this investigation are given in Chapter 7. A description of the method used to calculate average interface temperatures is given in Appendix I, and the possible effect of surface roughness on the experimentally obtained concentration profiles of tungsten and cobalt is discussed in Appendix II.

CHAPTER 2 : LITERATURE REVIEW

Reviewing even the most relevant literature in the cross-disciplinary field of metal cutting is quite an exhaustive and daunting task. In this brief review, attention has primarily been paid to reviewing the materials issues in machining. Accordingly, the review has been divided into the following sections :

A) Chip Formation

- Mechanism of Chip Formation
- Mechanics of Chip Formation

B) Temperatures in Metal Cutting

C) Tool Wear

- Wear Characteristics of Cutting Tools
- Micromechanisms of Tool Wear

D) Improved Machinability Through Inclusion Engineering

2-A : Chip Formation

The entire process of chip formation consists of severe plastic deformation of the workpiece material (primary shear) in front of the cutting edge where the chip body is delineated from the bulk of workpiece material and further deformation of the chip (secondary shear) as it

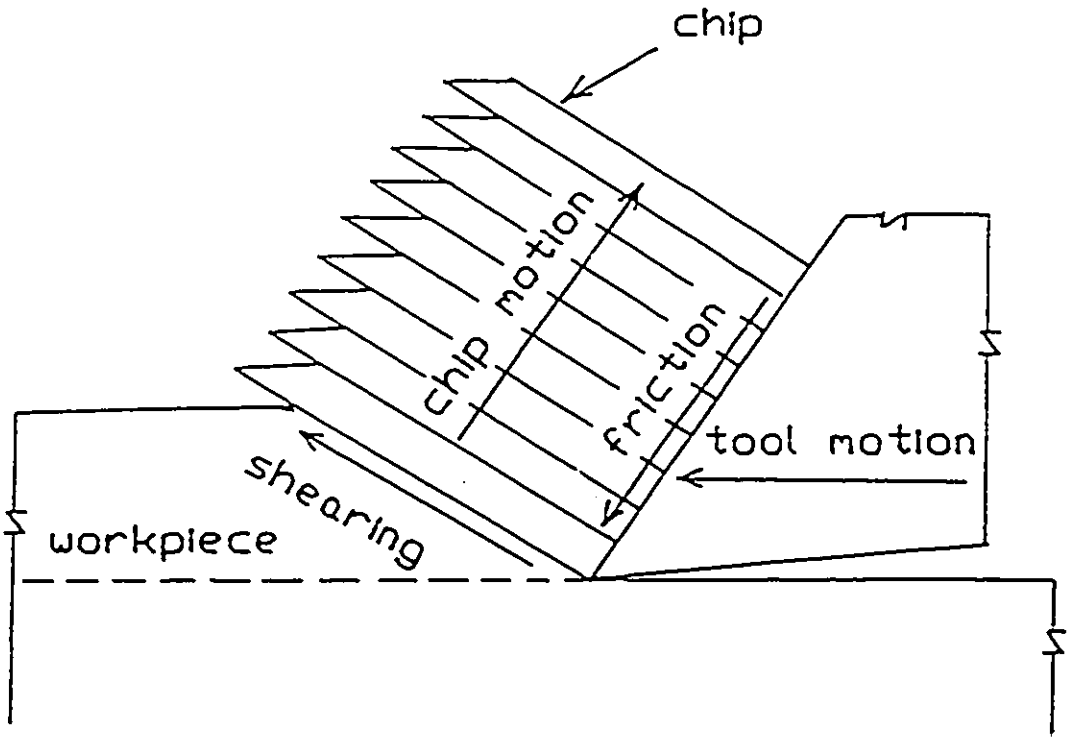

Fig.2.1 An idealized model of chip formation.

slides over the rake face of the tool and finally separates by a fracture process. The flow properties of the workpiece material under the existing conditions determine the relative ease of the chip formation process. The size and shape of the chips are known to vary a great deal and are controlled by a number of factors such as the ductility of the workpiece, inclusion characteristics and the cutting conditions.[1] The study of chip formation process is difficult due to the small scale of the phenomena to be observed. However, high speed cine-photography of the cutting process using a transparent sapphire tool [2] has given a good idea of chip formation. The technique of freezing the cutting process by means of a quick-stop device also gives an idea of the chip formation process as the chip remains attached to the workpiece under the conditions which approximately exist during cutting. Various quick stop devices, based on different techniques of suddenly disengaging the tool, are described in references [3-7].

2-A·1 : Mechanism of Chip Formation

The principal mechanism of chip formation has been recognized to be shear. As a direct consequence of plastic deformation, chip thickness is seen to be greater than the thickness of the uncut layer. An idealized model of chip formation was proposed by Piispanen, [8] and is shown in Fig.2.1. In this model the process of chip formation is

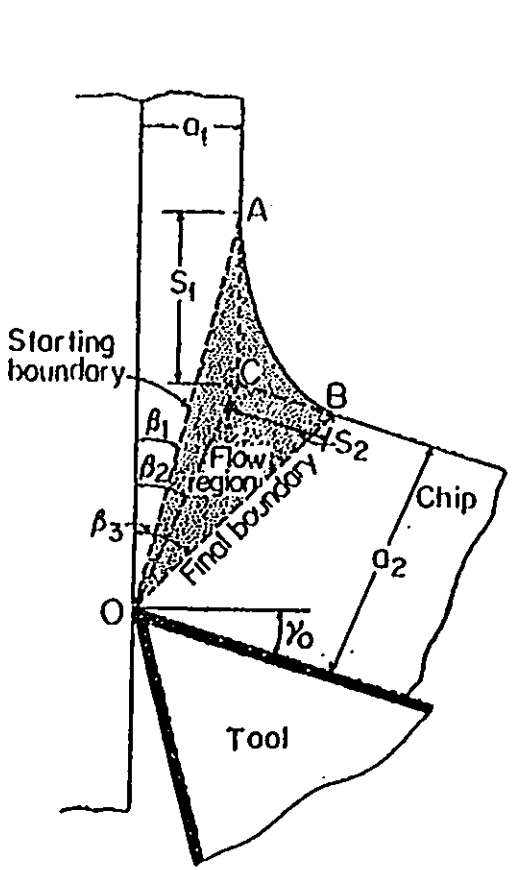

(a) The Okushima and Hitomi model

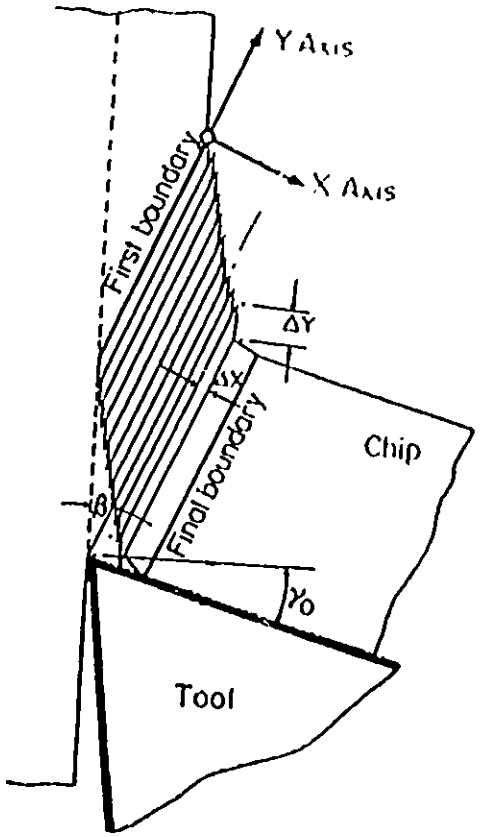

(b) The Oxley and Welsh model

Fig.2.2 Primary shear zone models

represented as a process of successive slip of workpiece material along a well-defined plane called the shear plane. However, a single shear plane implies an infinite rate of change of velocity of the material, as it passes across the shear plane. The concept of a zone of severe plastic deformation was therefore introduced. Okushima and Hitomi [9] assumed a flow region of the type shown in Fig.2.2(a) and showed that for cutting speeds higher than 150 m/min the width of the primary shear zone is only a few microns. Thus, the shear zone approaches a shear plane. Oxley and Welsh [10], on the other hand, assumed the primary shear zone to be bound by parallel sides as shown in Fig.2.2(b). It was shown that the parallel sided shear zone theory predicted trends in shear angle and cutting forces with a variation of cutting speed and feed, which agreed well with the experimental results.

The secondary shear zone typically extends into the chip to about 10% of the chip thickness for steels. It is a direct result of the quasi-static seizure between tool and chip over the sticking part of the contact length, which has been well documented by Trent.[11] The flow of the chip material is retarded due to seizure and the resultant velocity profile is shown in Fig.2.3. This retardation leads to shear between two adjacent layers of the chip material. The shear strain as well as the strain rate can be calculated from the observed retardation of flow lines. The

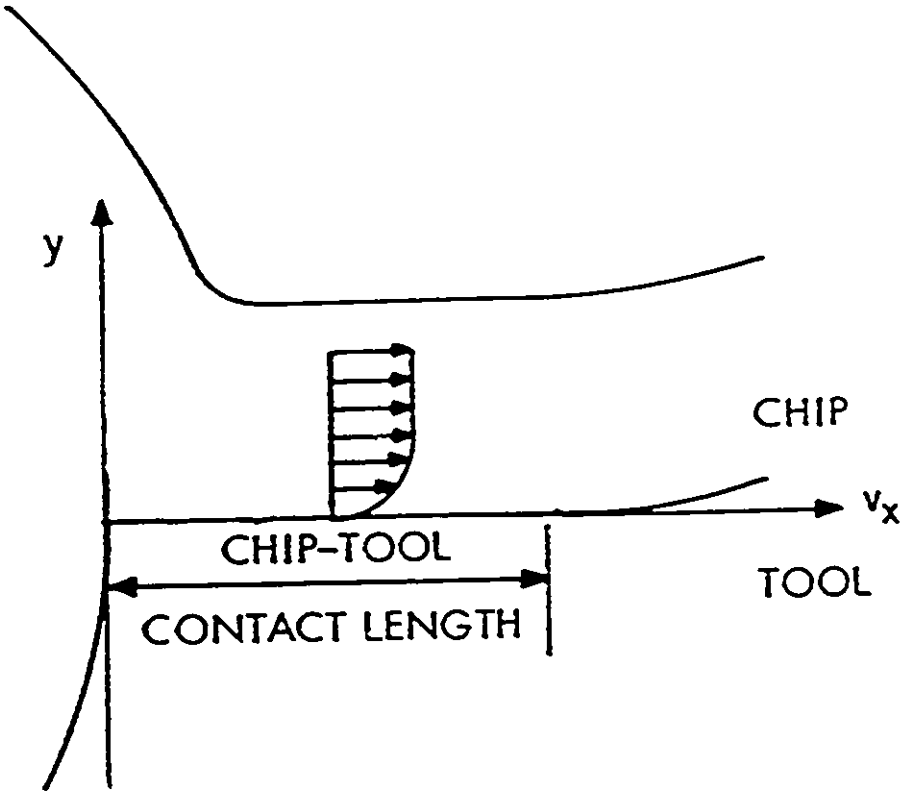

Fig.2.3 The velocity profile in the secondary shear zone.

strain rates so calculated are typically of the order of 10^4 per s and hence, the process of secondary shear is thought to be adiabatic in nature.[12] An adiabatic plastic deformation process in medium and high carbon steel at such high strain rates leads to the formation of transformed shear bands whose microstructure consists of submicron size equiaxed grains. Similar structures have been reported by Shelbourn [13] and Hau-Bracamonte [14] in the secondary shear zone of steel chips.

The secondary shear zone introduces an important heat source at the tool-chip interface. It was first incorporated into the model for obtaining interface temperatures by Boothroyd [15]. The adiabatic heating of the material in secondary shear zone leads to interface temperatures in excess of $1000^{o}C$ while cutting steels at medium cutting speeds of about 150 m/min. Thermally activated processes can occur at appreciable rates at these elevated temperatures and thus, tool life can decrease appreciably due to processes taking place in secondary shear zone.

2-A·2 : Mechanics of Metal Cutting

An analysis of the mechanics of the metal cutting process allows the prediction of cutting forces and temperatures from the mechanical and thermal properties of the workpiece material. Optimum cutting conditions can thus,

be selected based on the predictions of this analysis.

Forces : Merchant [16] considered the chip above the shear plane as a rigid body moving with a constant velocity. Thus, the resultant of the forces acting on the chip from the tool, R, and from the workpiece, R', is zero as shown in Fig. 2.4(a). The forces R and R' can be resolved into their components and the force balance can be represented in a convenient way by means of Merchant's circle diagram, shown in Fig.2.4(b). The relationships between various forces can easily be derived from this diagram and are given in Appendix I. This representation is valid for orthogonal cutting operations only, where the radial force is zero and only the cutting force, F_C and the feed force, F_T make up the total force exerted on the (sharp) tool. However, if the nose radius is a significant fraction of the depth of cut, (restricted cutting) the radial force is not negligible due to the contribution from the secondary cutting edge. The magnitude of the radial force is determined by the deviation of the chip flow direction from the orthogonal direction (ψ) which depends on the ratio of feed to the depth of cut [17]. If the cutting edge in a restricted cutting operation is perpendicular to the feed direction, the following relationship between the forces is observed :

$$F_R = \sqrt{(F_T^2 + F_R^2)} \cdot \cos(\pi/2 - \psi) \qquad (2.1)$$

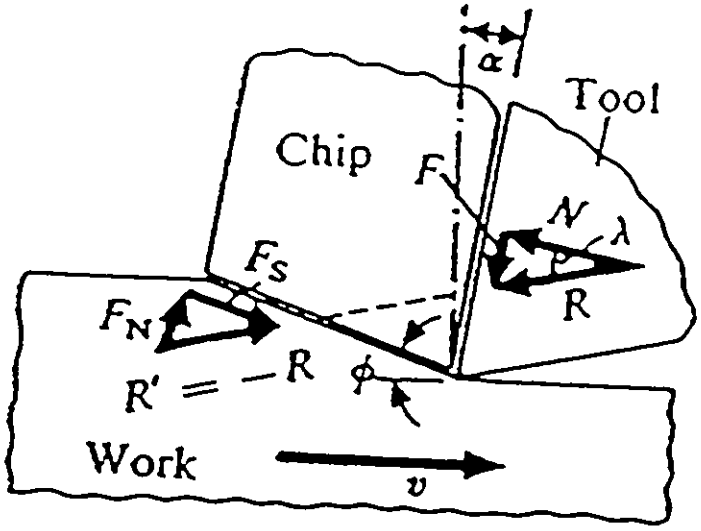

Fig.2.4(a) The forces acting on a tool-chip system.

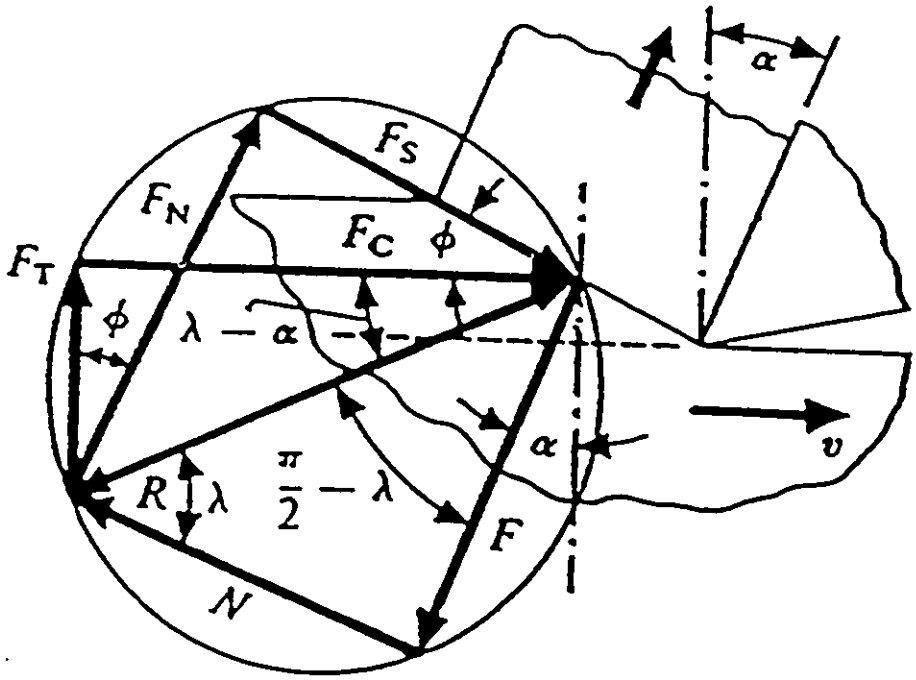

Fig.2.4(b) A Merchant diagram showing the equilibrium of forces involved in orthogonal cutting.

The development of wear land on the flank face of the tool introduces additional forces on the tool as a result of frictional contact between the flank face and the workpiece material. The flank force cannot be easily separated from the measured values of the total force acting on the tool. Micheletti *et al.* [18] considered the total force acting on the tool to be composed of two components, one applied on the rake face and the other on the flank face of the tool. Force measurements carried out with a series of tools having known widths of flank wear land showed that the forces increase linearly with the width of flank wear land. The increase in forces was considered to be due to flank wear only, and flank force calibration curves were obtained as a function of flank wear at a given cutting speed. The increase in forces due to flank wear has been utilized in adaptive control for on line measurements of tool wear [19].

Stresses : Conventional materials testing data is of very limited value in predicting the flow stress to be expected in metal cutting, as the flow conditions are entirely different than those met in conventional testing. There is no test which can simulate high plastic strains at strain rates of the order of $10^4 s^{-1}$, under high hydrostatic pressures under a flow constraint (tool). Thus, the shear stress of the material, as the force along the shear plane divided by the shear plane area, has to be obtained from the

cutting tests themselves. In general, the shear strength of metals and alloys has been found to vary only slightly over a wide range of cutting speeds and feeds[20].

Strains : The strain associated with the shear process occurring in the primary shear zone, γ, is given by a relatively simple relationship involving the rake angle, α, and the shear angle, ϕ, as given below :

$$\gamma = \frac{\cos \alpha}{\sin \phi \cdot \cos(\phi - \alpha)} \qquad (2.2)$$

The shear angle ϕ, is fixed by the system and the machinist has no control over it. The shear strain created in both the primary and the secondary shear zones can be calculated from the magnitude and direction of grain elongation. It is observed [21] that the direction of maximum grain elongation is not the same as the shear plane direction, and a number of models have been developed for the determination of the shear angle. A comparison between these models can be found in reference 1. The equations derived based on these theories have been summarized in Table 2.1. The Lee and Shaffer theory serves as a lower bound, whereas the Merchant theory serves as an upper bound for shear angle calculations.

Table 2.1

Collection of the equations for shear angle determination [1]

Theory	Equation for Shear angle
Ernst & Merchant	$\phi=\frac{\pi}{4}+\frac{\alpha}{2}-\frac{\beta}{2}$
Lee & Shaffer	$\phi=\frac{\pi}{4}+\alpha-\beta$
Stabler	$\phi=\frac{\pi}{4}+\frac{\alpha}{2}-\beta$
Hucks	$\phi=\frac{\pi}{4}+\alpha-\frac{\tan^{-1}(2\tan\beta)}{2}$
Kronenberg	$\phi=\frac{\pi}{4}+\frac{\alpha}{2}-\beta(0.75+0.0045\alpha)$
Oxley	$\phi=\alpha-\beta+\tan^{-1}\left(\frac{1}{2}+\frac{\pi}{4}-\phi+\frac{\cos2(\phi-\alpha)}{2\beta}-\frac{\sin2(\phi-\alpha)}{2}\right)$

2-B : Temperatures in Metal Cutting

The important role played by cutting temperatures in determining tool life was recognized by Taylor [22] as early as in 1907 in his famous paper, 'On the art of cutting metal'. This is still being investigated in the 1990s, e.g. by Matthews [23]. This demonstrates the importance and complexity of the problem. The primary shear zone, the secondary shear zone and friction at the tool-chip interface represent the three sources of heat in metal cutting using a sharp tool, whereas, the chip, the workpiece and the tool represent the heat sinks. The solution of the heat transfer problem to determine the temperature distributions arising from the non-uniform heat generation rates in the two shear zones, is complex. The experimental and theoretical approaches to determination of cutting temperature are described below.

2-B·1 : Experimental Approach

Trigger [24] measured the tool temperatures using the principle that an emf is generated at the interface of two dissimilar metals (tool-chip interface in this case) when the temperature at the interface changes. While this technique is relatively simple to apply, it has its limitations. This method measures the mean temperature of the tool including both the flank and the rake face. Also,

in the presence of a built-up-edge, the results can be misleading. Using this technique, it was demonstrated by Trigger that the equilibrium values of temperatures are reached almost instantaneously after the start of a cut.

Thermocouples embedded in cutting tools at various locations have been successfully used by Kusters [25]. However, this technique is extremely tedious. The cavity in which the thermocouple is placed must be small in relation to the contact area of 1-2 mm^2 to avoid any effect on the temperature field to be mapped. The results obtained using this technique successfully showed that the maximum temperature occurred on the rake face some distance away from the cutting edge.

Boothroyd [15] heated the workpiece to about 600^{o}C and photographed the infrared radiation from the workpiece, HSS tool and the chip during orthogonal cutting. On comparing the observed intensities of infrared radiation with standard calibration curves, the temperature distribution shown in Fig.2.5 was obtained. The required heating of the workpiece limited the maximum cutting speed which could be studied using this technique. The main difficulty with radiation techniques is that they are generally limited to the accessible surfaces. These difficulties have been overcome to some extent by drilling small holes in the tool or the workpiece[26].

Wright and Trent [27] studied the microstructural

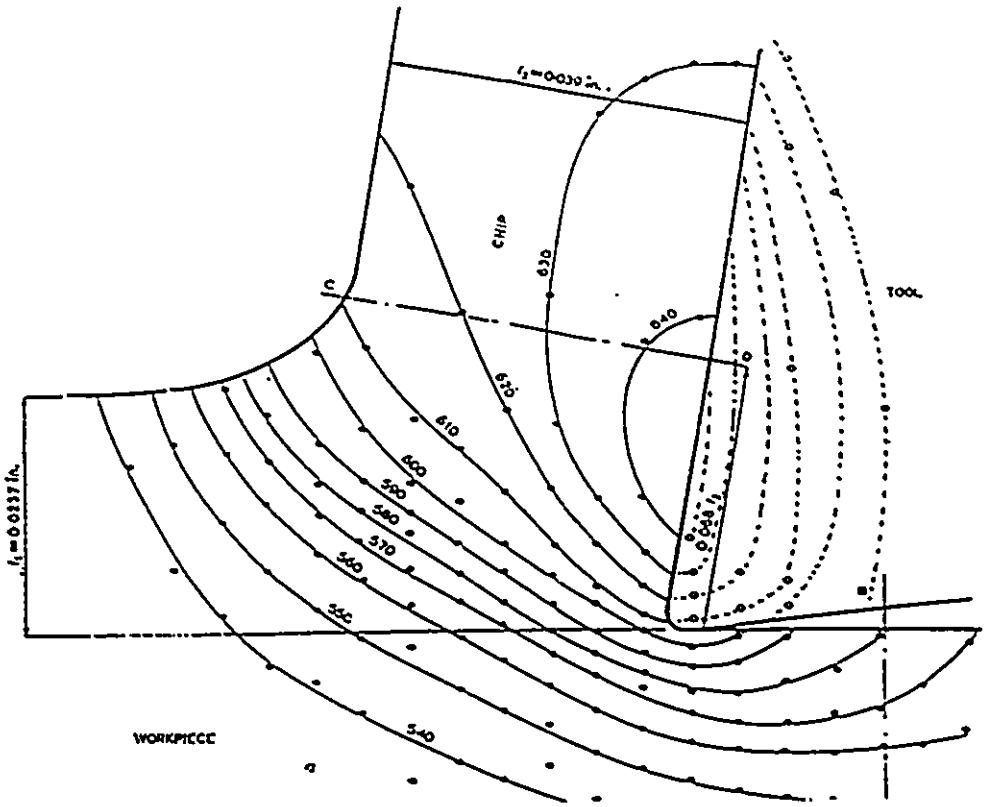

Fig.2.5 A typical experimentally obtained temperature distribution. (Boothroyd [15])

changes as well as the changes in the microhardness of a HSS tool after 30 second of cutting and succeeded in mapping the temperature distribution. They reported the uncertainties of $\pm 25^{o}C$. After the 30s wear test, the tool was sectioned halfway through the depth of cut, polished and etched. The changes in structure were observed and interpreted with the help of calibrated samples. The calibration samples were thin plates of tool material that were held in a salt bath at a known temperature for 30 second and quenched in water. However, there were no sharp temperature gradients in the plates. These are invariably present in the cutting tool. The effect of sharp temperature gradients on the microstructure of the tool was neglected. The same technique was successfully applied by Dearnly and Trent [28] to study the temperature distribution using iron bonded carbide tools. However, this method cannot be used for cobalt bonded carbide tools because no observable structural changes occur in the heat affected zone during cutting.

2-B·2 : Analytical Approach

The heat transfer process occurring during orthogonal machining is described by the following steady state, two dimensional energy equation :

$$\rho S \cdot \left(U \frac{\partial T}{\partial x} + V \frac{\partial T}{\partial y} \right) - K \cdot \left(\frac{\partial^2 T}{\partial x}^2 + \frac{\partial^2 T}{\partial y}^2 \right) - Q = 0 \qquad (2.3)$$

where ρ, S, K, T are the density, specific heat, thermal conductivity and temperature respectively. Q is the heat generation rate per unit volume, x and y are the Cartesian coordinates, and U and V are the velocity components in X and Y directions. The region in which this equation is to be solved is shown in Fig.2.6 along with the boundary conditions. In addition to these boundary conditions, assumptions regarding the heat sources are required to solve the problem. Rapier [29] assumed that the heat sources in both the primary and secondary shear zones are planar and uniform. The maximum temperature along the tool-chip interface was found to be at the end of the planar heat source. It was shown by Rapier that most of the heat generated in the frictional heat source was carried away by the chip and thus, the thermal properties of the cutting tool had little influence on the temperatures generated at the tool-chip interface. Boothroyd determined the temperature distribution experimentally and showed that the experimental values were considerably lower than the values predicted by the Rapier model[15]. He attributed this discrepancy to the existence of a distributed heat source along the contact length rather than a planar heat source as assumed by Rapier. The temperature distribution was shown to be a function of the size and shape of this distributed heat source. Tay [30] successfully applied finite element analysis to calculate the temperature field generated in the

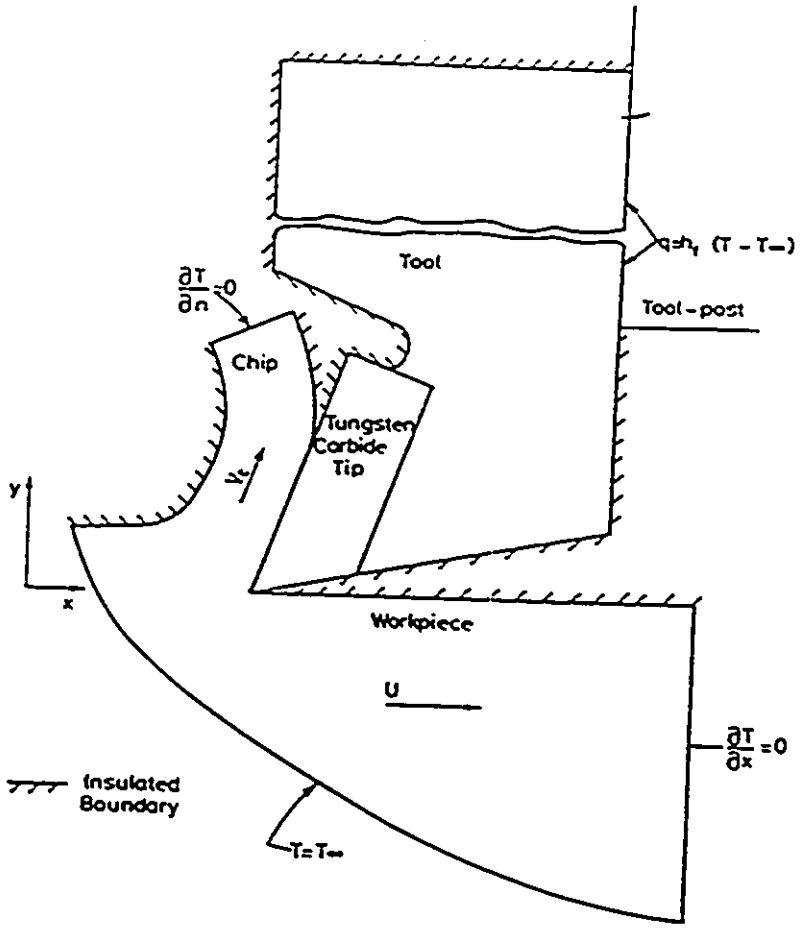

Fig.2.6 The problem region showing the boundary conditions for analytical determination of the temperature distributions.

workpiece, chip and the tool during orthogonal machining. The measured values of the cutting forces and the experimentally determined flow fields obtained by the printed grid technique were used as input. This solution takes into account the actual chip the tool geometries, the measured velocity and heat source distributions within the primary and secondary shear zones, the variations in thermal properties with temperature and the variation of flow properties of the workpiece with strain, strain rate and temperature. A typical temperature distribution obtained using this technique is shown in Fig.2.7. While this technique enables variable material properties to be included in the analysis, the results depend on the values fed into the program. Also, this technique is not predictive, since it requires input that must be obtained from machining tests. Nevertheless, this analysis is the most comprehensive treatment of the problem available in the literature.

By studying the temperature distributions obtained under several cutting conditions, Tay *et al.* [31] and Hastings *et al.*[32] have found some empirical relationships which are useful in the calculation of the average tool-chip interface temperatures. Calculations of average tool-chip interface temperatures are described in detail in Appendix I. Average interface temperatures increase parabolically with cutting speed, and a typical experimental result is

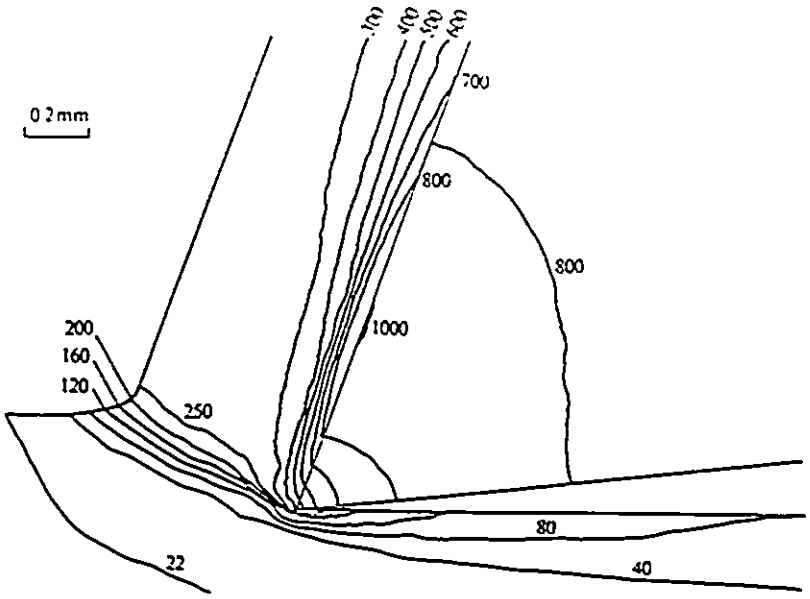

Fig.2.7 Temperature distribution obtained by the finite element method.(Tay et al[30])

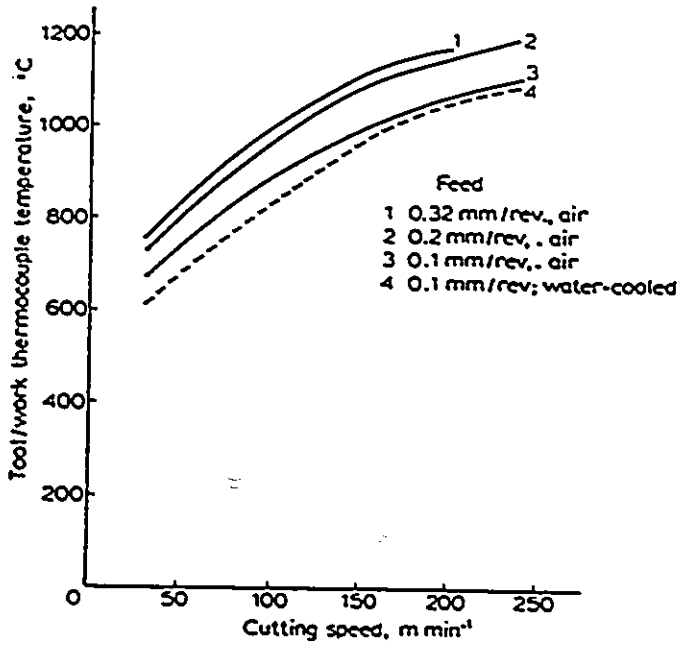

Fig.2.8 The variation of average interface temperatures with cutting speed.[96]

shown in Fig.2.8.

2-C·1 : Wear Characteristics of Cutting Tools

Flank wear is usually measured in terms of the width of wear land, V_B. Flank wear leads to unwanted rubbing between the clearance face of the tool and the workpiece material. The frictional heating in this process causes an increase in temperature at the cutting edge. Flank wear characteristics are shown in Fig.2.9(a). Both HSS and cemented carbide tools show similar behaviour. Point A in the figure indicates the end of tool life. It can be seen that tool life (T) decreases when the cutting speed (V) is increased. The relationship between V and T is called the Taylor equation :

$$V \cdot T^n = C \qquad (2.4)$$

where, n and C are constants for a given tool-workpiece combination. The value of n increases as the tool material becomes more refractory[33].

Tool Material	Value of n
High speed steel	0.1
Tungsten carbide	0.2
Alumina	0.4

Flank wear is usually measured microscopically, but it can

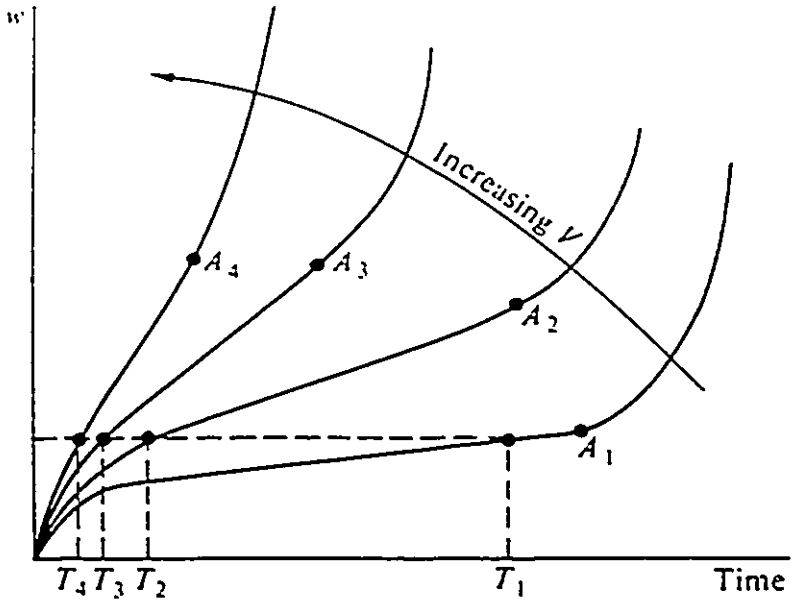

Fig.2.9(a) The flank wear characteristics of tools.

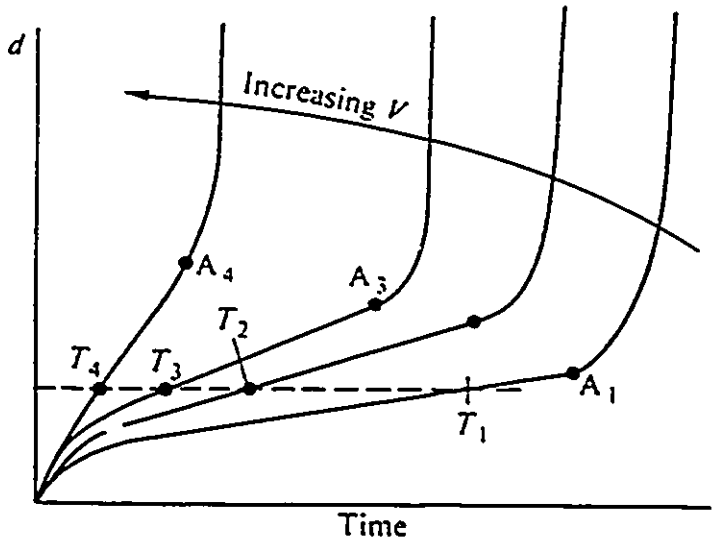

Fig.2.9(b) The crater wear characteristics of tools.

also be monitored using adaptive control[19].

Crater wear is conventionally specified by reporting the maximum depth of crater formed on the rake face of the cutting tool. Crater depth is usually determined by using a profilometer. Crater wear characteristics of a cutting tool are shown in Fig.2.9(b). It can be seen that the crater wear rates (and hence tool lives) are strongly influenced by an increase in cutting speed. Tool life, as determined by crater wear, can be taken just short of tool destruction when the crater becomes large and the load can no longer be supported by the cutting edge. A Taylor type equation with different values of n and C also holds for tool life based on crater wear. The influence of cutting speed on crater wear rates is mainly through the increase in tool-chip interface temperatures. Based on this observation, Usui *et al.* [34] proposed the following characteristic equation for crater wear :

$$\frac{1}{\sigma_t}\left(\frac{dW}{dL}\right) = C_1 \cdot \exp(-C_2/\theta) \qquad (2.5)$$

where, dW = Wear volume per unit contact area.

dL = Sliding distance.

σ = Normal stress on the contact surface.

θ = Tool-chip interface temperatures.

C1 and C2 are empirical constants.

The conventional method of specifying crater wear does not

give the volume of crater or the weight of material removed from the rake face. In the present investigation, Instrumental Neutron Activation Analysis has been used to determine these, which are then used in quantitative calculations of crater wear rates.

2-C·2 : Micromechanisms of Tool Wear

Tool wear is not a result of one unique mechanism, but rather a result of variety of mechanisms, each one of which can become a dominant wear mechanism under certain cutting conditions. The major micromechanisms of tool wear are adhesive wear, abrasive wear, chipping, plasticity dominated wear, corrosive wear, dissolution wear and oxidation wear. A detailed description of these mechanisms is given below.

1) Adhesive Wear : It has been pointed out that the chip flowing over the rake face of the tool cleans the surface so that virgin surfaces free from any contaminants and oxides are created[35]. In the presence of large stresses, there is a potential for these virgin surfaces to become one continuous adhesive junction. It has been found, especially during machining of austenitic stainless steel [20] that when this junction is broken due to the flow of chips, some part of the tool material is removed. It has been found that the ratio of wear of the two materials is $(H_s/H_h)^2$, where H_s

and H_h are the hardnesses of the soft and the hard material respectively. With more brittle cemented carbide tools, the adhesive junction can result in the whole carbide particle being plucked from the tool. Trent has termed this process as attrition wear[36].

2) **Abrasive Wear** : Abrasive wear involves the removal of tool material by the scoring action of hard phase particles or inclusions in the workpiece material. These particles act as miniature tools. Ramalingam and Wright [37] have described in detail, the mechanism involved in such a process. They have shown that the process of abrasive wear can be perceived as microchipping of the tool due to sudden increases in force exerted over a localized area. Machining experiments with materials of controlled microstructure have shown a clear correlation between increased tool wear and increased amounts of abrasive particles in the work material in accordance with the abrasive wear model[2].

3) **Chipping** : Cutting tools inherently suffer from low fracture toughness, and hence are susceptible to severe damage by cracking or chipping when subjected to sudden loads or thermal shocks. A comprehensive model developed by Sigl and Fishmeister [38] for the evaluation of the toughness of cemented carbides shows that the toughness is strongly influenced by binder composition. Using this model

it was shown that the toughness of WC-Co is superior to that of TiC-Ni. The problem of tool failure due to chipping is particularly severe for alumina based tools, but zirconia additions markedly improve their toughnesses[39]. In order to establish a basis for comparison between the toughness of various tool materials, the following equation was proposed by Evans and Charles [40]:

$$K_H = 0.113\ H \cdot D^{1/2} (1+C_L/2D)^{-3/2} \qquad (2.5)$$

where, K_H is the indentation fracture toughness

H is the Vickers hardness in GPa

D is the indentation diagonal in micron

C_L is the total length of cracks developed at the corners of indentation in micron

Chipping leads to catastrophic failure during practice and can not be tolerated.

4) Plasticity Dominated Wear : It has been shown that the chip can exert sufficient shear stress on the surface layers of the tool and may cause it to deform at low strain rates thereby dragging the tool material from the crater region. This type of wear is significant for HSS tools operated near the limits of their endurance. The most serious form of wear involves thermal weakening of the cutting edge and large

scale deformation under the existing stresses. The resultant rubbing of the tool against the workpiece generates additional heat leading to catastrophic failure. This wear mechanism mainly decides the maximum allowable cutting speed for a given tool-workpiece combination.

5) Chemical or Corrosive Wear : Chemical wear is a result of actual chemical reaction at the tool-chip interface. Dissolution wear, a result of dissolution of the tool material into the chip is treated as a separate wear mechanism. Brandt[41] showed that layers of calcium aluminosilicate inclusions are formed on the rake face of cutting tools over a range of cutting speeds. If alumina tools are used to machine calcium treated steels, the observed wear rates are high. This was shown to be due to the formation of a soft phase due to a chemical reaction between the alumina tool and the inclusion layer. A similar layer of lead over the rake face of cemented carbide cutting tools is suspected to lead to some crater wear despite a lowering in the interface temperatures resulting from its presence[42,43].

6) Dissolution Wear : When the tool-chip interface temperatures are high, such as those reached during the high speed machining of steels, the tool material from the rake face dissolves in the chip material leading to crater wear.

[44-47] The crater wear process, under these circumstances, is shown to be markedly temperature sensitive[48]. The fact that crater wear rate increases with the solubility of tool material in the chip supports the principle of dissolution wear.

Analysis of dissolution wear is based on the assumption that a thermodynamic equilibrium exists at the tool-chip interface at all times. Thus, during the machining of steel using a cemented WC tool, the concentration of tungsten in the first atom layer of the chip is maintained constant during the cutting operation (if the temperature remains constant) and can be calculated from the solubility product of tungsten carbide in the chip material. When some tungsten is carried away into the chip from the first atom layer, additional tool material dissolves to maintain the equilibrium value, and in the process leads to more crater wear. However, with regard to the mechanism of transport of dissolved tool material away from the interface, there is a great deal of controversy in the literature.

The diffusion model assumes that a diffusional flux of the dissolved tool constituent in response to the existing concentration gradient is the mechanism of solute removal from the first atom layer of the chip. A detailed description of the quantitative thermokinetic model based on this concept are given in Chapter 5.

The convective flow model, on the other hand,

considers a convective flow of material next to the tool-chip interface in the vertically upward direction to be responsible for the transport of dissolved tool constituents away from the first atom layer of the chip[47]. The velocity profile corresponding to various layers of chip material in the flow zone is shown in Fig.2.3. The existence of sharp velocity gradients in the chip material within the flow zone was argued by Kramer [49] to be analogous to the velocity gradients existing in a liquid flowing over a solid in a turbulent manner. Based on this similarity, boundary layer theory was considered appropriate for the problem. The following mass balance equation (valid for incompressible fluids exhibiting the above velocity gradients) was applied to the chip material in the flow zone :

$$\frac{\partial V_x}{\partial x} + \frac{\partial V_y}{\partial y} = 0 \qquad (2.6)$$

As shown in Fig.2.3, the material very near the interface slows down. Thus, the gradient of the X component of velocity, $\partial V_x/\partial x$ is negative. The mass balance equation requires that $\partial V_y/\partial y$ be positive. This positive velocity component normal to the interface, V_y can transport away the material dissolved at the interface. Thus, the steady state wear rate was expressed as follows :

$$\dot{V} = \int K \cdot \left(-D\frac{\partial C}{\partial y} + C_s \cdot V_y \right) dA \qquad (2.7)$$

where, $\dot{V}$ = the wear rate of the tool material being dissolved.

K = the ratio of the molar volume of the tool material to that of the deforming workpiece.

D = the diffusivity of the slowest diffusing tool constituent in the flow zone.

C = the concentration of the dissolved tool constituent in the chip material.

C_o = the above concentration at the interface.

V_y = the bulk velocity of the chip material at the interface in the Y direction.

A = the interfacial area.

Kramer argued that the diffusion flux term (the first term on the right hand side of the above equation) is much smaller than the second term when sharp velocity gradients are present in the flow zone. The crater wear rate is expressed as follows :

$$V_c = K \cdot C_o \cdot V_y \qquad (2.8)$$

where, V_c is the rate of increase of the depth of crater.

The difficulty in calculating the values of V_y precludes any computation of either the crater wear rate or the dissolution wear amount for a given tool-workpiece combination at a given cutting speed. However, if V_y is taken to be the same when a given material is slid against various tool materials with similar characteristics, then the ratios of crater wear rates in the two cases can be obtained as follows :

$$\frac{(V_c)_1}{(V_c)_2} = \frac{(K \cdot C_o)_1}{(K \cdot C_o)_2} \qquad (2.9)$$

It was shown that the expected ratios of wear rates based on the above equation agree with the experimentally observed ratios of the wear rates.

The above controversy regarding the mechanism of solute transport is discussed in the light of the analysis of results obtained in this investigation in Chapter 6.

7) Oxdidation Wear : The high temperatures reached during metal cutting creates a potential for oxidation wherever oxygen can penetrate within the tool-chip contact area. There is evidence of the continuous formation and breaking down of adhesive junctions between the oxides formed at high temperatures and aluminum oxide (sapphire) tool[2]. Such

oxidation process has been shown to take place at the extremity of depth of cut and immediately behind the nose radius, where adhesion between the oxides is responsible for tool wear.

2-D : Improved Machinability Through Inclusion Engineering

Van Vlack [50] reported as early as in 1952, that the machinability rating of resulphurized Bessemer steel correlated strongly with the MnS inclusion characteristics. Higher inclusion count and a length to width ratio close to unity improved the machinability rating considerably. The aspect of machinability most clearly influenced by these inclusions is chip formation. Micro-examination of quick stop sections has shown that sulphides are elongated in the direction of shear. However, it was shown that the free machining qualities of resulphurized steels resulted primarily from effects occurring in secondary shear zone, e.g. by Stevenson [51]. Many workers have reported the formation of a stable film of MnS on the rake face of the tool [52-56]. This film would certainly have the effect of reducing crater wear, but its presence does not necessarily explain the avoidance of a built-up-edge generally observed. The power requirements during machining of resulphurized steels are reported to be lower than the corresponding steels of low sulphur content. It was shown by Fenton and

Oxley [57] that reduction in shear stress at the tool-chip interface would lead to an increase in shear angle and a decrease in tool force. Dines [56] observed a reduction in tool-chip contact lengths in the presence of thin MnS films on the rake face and a corresponding decrease in power requirements. Milovic [43] has shown that the rake face temperature is lower while cutting a high sulphur steel as compared with the corresponding steel of low sulphur content. Soft and deformable MnS inclusions are shown to have a beneficial effect on flank wear characteristics of the cutting tools also [58].

In contrast to soft deformable MnS inclusions, hard and non-deformable alumina inclusions cause rapid abrasive tool wear. Machining experiments with materials of controlled microstructure have shown a clear correlation between increased amounts of abrasive particles in the workpiece and increased flank wear rates [2]. Numerous studies sparked by the first successful result obtained in Germany, [59] have shown that problems in machining due to alumina inclusions can be overcome by calcium treatment during ladle deoxidation. Calcium treatment leads to the formation of soft calcium aluminosilicate inclusions under suitable conditions. The thermochemical conditions which must be maintained in the ladle in order to form the desired soft anorthitic or gehlenetic inclusions during calcium treatment can now be calculated, e.g. Kay *et al.* [60]. These

inclusions are known to form protective layers on the rake face of the tool similar to those due to MnS inclusions, and this phenomenon has been investigated thoroughly [61-63]. In general, tool life is improved by the presence of calcium aluminosilicate inclusions in the workpiece. However, during high speed machining with alumina tools, exactly opposite results are reported by Brandt [41]. Calcium aluminosilicate was shown to chemically react with alumina tools to form a soft phase which resulted in rapid crater wear. Steels containing hard alumina inclusions, on the contrary resulted in better tool lives due to the absence of this reaction.

Using the concept of critical accumulated damage for fracture, Subramanian *et al.* [64] argued in favour of designing of clean steels for improved mechanical properties with high speed machining. The chip formation process was shown to be facilitated by increased damage rates and strain localization due to the high strain rates characteristic of high speed machining. It was concluded by the authors, that at high strain rates, it may not be necessary to promote ductile fracture by decreasing the distance between the inclusions (and hence voids) through the use of free cutting additives.

Thus, in summary, the free cutting behaviour of a given steel is seen to improve by increasing the number of soft and deformable inclusions which are also chemically inert with respect to the cutting tool material. However,

inherent disadvantage of this approach is the loss of through thickness ductility of steel with an increase in inclusion content. Therefore, inclusion optimization, geared for the specific requirements of the material, is necessary.

Chapter 3 : Experimental Procedures

In a research project dealing with the analysis of tool wear, measurements of material loss from the tool are obviously involved. In addition to this, the parameters influencing tool life must be measured experimentally. The variation of these parameters, if any, during the course of a wear test must also be established. A critical examination of the tool-chip interface is necessary to develop crater wear models. These objectives have been reached by means of a series of experiments employing various analytical techniques as described below.

A) Materials Characterization : The matrix and inclusions of the workpiece materials were characterized using optical microscopy and electron microprobe analysis.

B) Wear Testing : A continuous speed MAZAK lathe was used for semi-orthogonal cutting of steel bars.

C) Dynamometry : A 3-component piezoelectric transducer type dynamometer was used to determine forces exerted on the tool during a wear test.

D) Quantification of Tool Wear: Instrumental Neutron Activation Analysis [INAA] was used to measure the concentration of tungsten in the chips. The results were used to quantify the amount of tool material transferred to the chips as a result of the wear process.

E) Determination of Tool-Chip Contact Lengths/Areas: The tool-chip contact lengths and contact areas were determined from photographs of the rake face of the tool, obtained using an optical microscope at a magnification of 32X.

F) Microstructural Study of the Secondary Shear Zone : Scanning Electron Microscopy [SEM] and Transmission Electron Microscopy [TEM] were used to study the microstructure of the secondary shear zone, especially the zone in the immediate vicinity of the tool-chip interface.

G) Chemical Study of the Secondary Shear Zone : Secondary Ion Mass Spectrometry [SIMS] was used to study the concentration profiles of tungsten and cobalt in the chips next to the tool-chip interface.

3-A: Materials Characterization

3-A·1 : Workpiece Material

A calcium treated AISI 1045 grade steel (Steel 1) was used as the workpiece material in most of the cutting tests. The other workpiece materials used were an AISI 1045 grade steel, produced without calcium treatment during deoxidation (Steel 2), and an AISI 316L grade austenitic stainless steel (Steel 3). The effect of 'hard' alumina inclusions on mechanical wear was studied using Steel 2, which is silica killed-aluminum grain refined. Steel 3 was used to study the concentration profiles of tungsten and cobalt in austenite. Table 3.1 gives the chemical

Table 3.1

Chemical composition of the workpiece materials

Element	AISI 1045 Steel with Ca-Treatment (Steel 1)	AISI 1045 Steel without Ca-Treatment (Steel 2)	AISI 316L Stainless Steel (Steel 3)
C	0.45	0.45	< 0.080
Si	0.21	0.288	0.350
Mn	0.76	0.862	1.321
P	0.007	0.034	0.032
S	0.005	0.020	0.024
Al	0.013	0.028	0.017
W	0.0011	0.0005	0.050
Co	0.0062	0.0010	0.117
Ca	0.0017	0.0004	0.0018
Ni	0.0700	-	10.08
Cr	0.0900	0.0320	16.33

compositions of the three steels.

3-A·1.1 : Matrix Characterization

Fig.3.1(a) and (b) show the microstructure of Steels 1 and 2, respectively. The ferrite-pearlite microstructure characteristic of the hot rolled medium carbon steels is observed in both the cases.

3-A·1.2 : Inclusion Characterization

The following types of inclusions were observed in Steel 1:

1) Globular inclusions with a ring around them, Fig.3.2(a).
2) Globular duplex inclusions, Fig.3.2(b)
3) Highly elongated inclusions, Fig.3.2(c)

The compositions of the inclusions 1 and 2 were determined by Electron Microprobe Analysis at CANMET, Ottawa. Inclusion #3 was identified as MnS, based on the morphology and the EDX spectrum. The raw elemental microprobe analysis of inclusion #1, obtained from the interior (region A) and the outer ring (region B) are given in Table 3.2(a). Based on the deoxidation practice, only aluminum, calcium, silicon, oxygen and sulphur are expected to be present. The other elements in the raw data are assumed to arise from the matrix, and were ignored. The normalized compositions corresponding to regions A and B of inclusion #1 are given in Table 3.2(a). The elemental

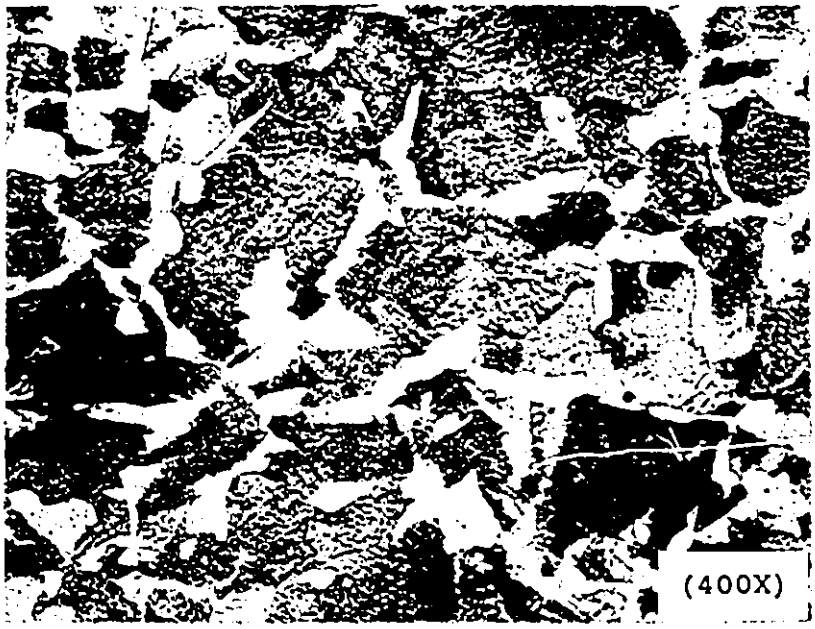

(a) Steel 1

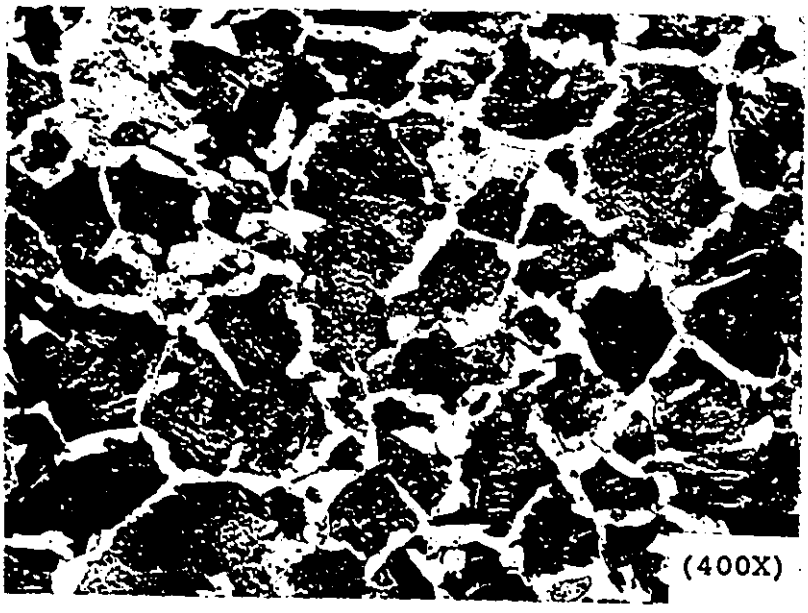

(b) Steel 2

Fig.3.1 Microstructure of the workpiece materials

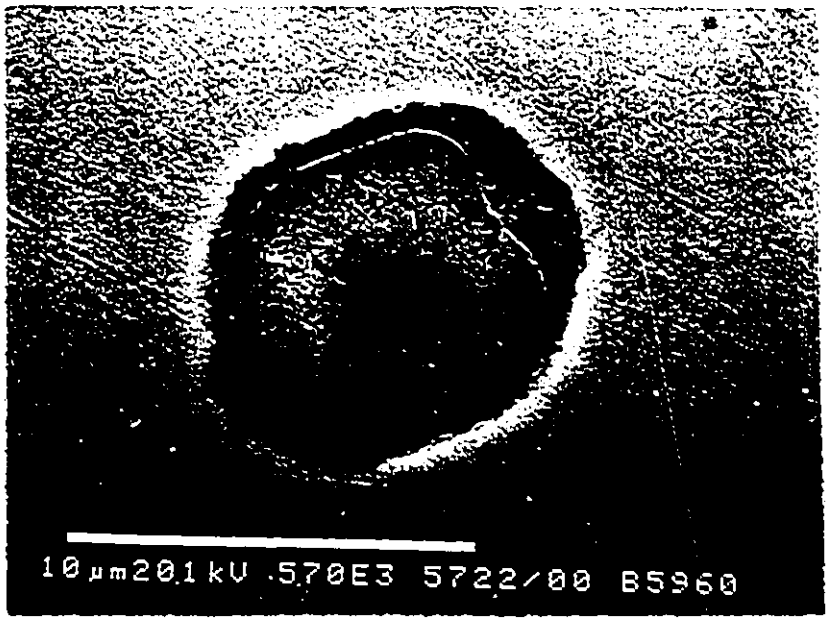

(a) Inclusion #1

(b) Inclusion #2

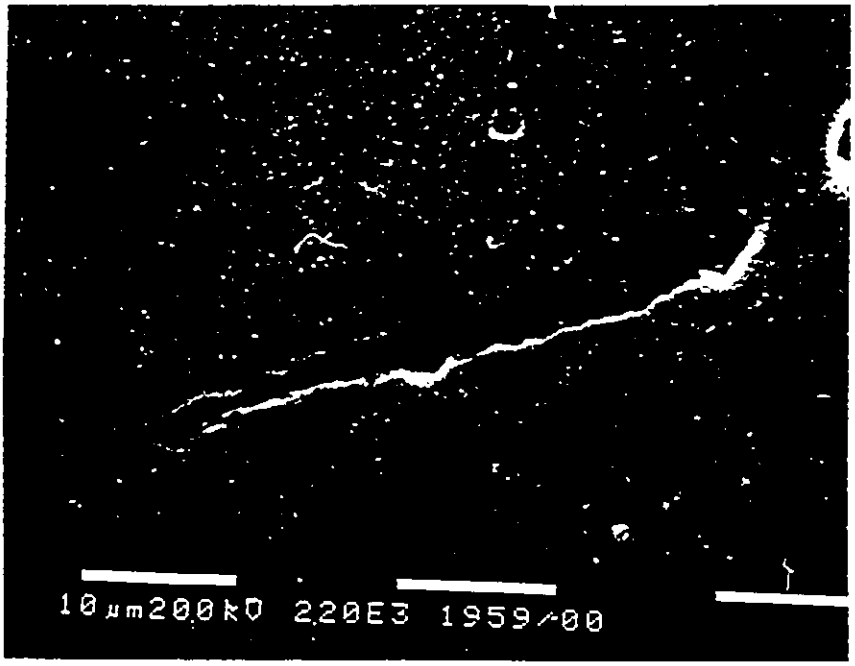

(c) Inclusion #3

Fig.3.2 Inclusion types present in Steel 1

Table 3.2 (a)
The elemental analysis and the normalized composition of inclusion 1.

Element	Area A (Raw Data)	Normalised Composition	Area B (Raw Data)	Normalised Composition
Al	33.38		7.65	
Si	1.35	28.2% CaO	0.42	
Ca	18.49		21.06	
S	0.31		14.69	
Mn	0.40	3.2% SiO_2	2.03	100% Cas
Mg	3.04		0.86	
P	0.26		0.273	
Fe	0.0	68.6% Al_2O_3	46.04	
O	42.78		6.98	

Table 3.2 (b)
The elemental analysis and the normalized composition of Inclusion 2.

Element	Area A (Raw Data)	Normalised Composition	Area B (Raw Data)	Normalised Composition
Al	28.7		1.61	
Si	1.92	40.85% CaO	0.28	
Ca	28.81		47.1	
S	0.61		34.5	
Mn	0.0	4.16% SiO_2	0.11	100% CaS
Mg	2.01		0.08	
P	0.36		0.466	
Fe	0.0	55.00% Al_2O_3	14.0	
O	37.56		1.78	

microprobe analysis of inclusion #2, from the interior (region A) and from one of the small globules at the periphery (region B) are given in Table 3.2(b). Elements other than aluminum, calcium, silicon, oxygen and sulphur were ignored as before, and the normalized compositions of the two regions of inclusion #2 were calculated, which are given in Table 3.2(b). It is seen from the normalized inclusion compositions, that the core is a calcium-aluminosilicate whereas, the outer ring and the globular chunks at the periphery are calcium sulphide. These inclusions are desirable for improved tool performance in machining.

The following types of inclusions were observed in Steel 2:

1) Highly deformed inclusions.

2) Small inclusions with sharp edges.

Based on the morphology, the highly deformed inclusions (Type 1) were identified as MnS. Fig.3.3(a) shows one of the small inclusions (Type 2) with sharp edges. Fig.3.3(b) shows the EDX spectrum obtained from this inclusion, indicating that it is alumina.

3-A·2: Tool Materials

In most of the cutting tests, Kennametal Grade K-11 tools were used. Some cutting tests were also carried out with Kennametal grade K-1 tools, and K-11 tools coated with

Fig.3.3(a) Inclusion #2 present in Steel 2

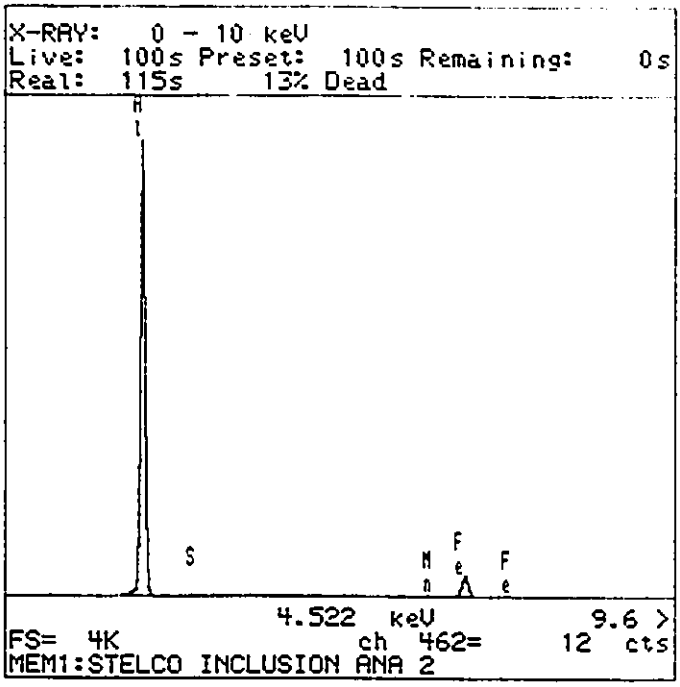

Fig.3.3(b) An EDX spectrum corresponding to Inclusion #2, present in Steel 2

HfN. The 10 micron thick hafnium nitride coatings on the K-11 substrates were provided by Teledyne Cutting Tools Inc., USA. The compositions of the two grades of tools[65], expressed in wt.% , are as follows:

Grade	WC	Ta(Nb)C	Co
K-11	97.0	0.4	2.6
K-1	85.0	4.0	11

Figs.3.4(a) and (b) show the SEM photographs of a K-11 tool and a K-1 tool, respectively. The particle size is in the range of 1-3 μm.

3-B : Wear Testing

Wear tests were carried out on a continuous speed MAZAK lathe under the following conditions :

Cutting Speed : Varied from 150 to 240 m/min.

Depth of cut : 2.01 mm

Feed : 0.173 mm/revolution.

Rake angle : + 5 degrees

Test duration : 30 second.

The cutting edge was kept perpendicular to the feed direction to approach orthogonal cutting conditions. However, the nose radius of the inserts used in the wear tests was equal to 0.79 mm which represents about 40 % of the depth of cut. Consequently, the cutting conditions were

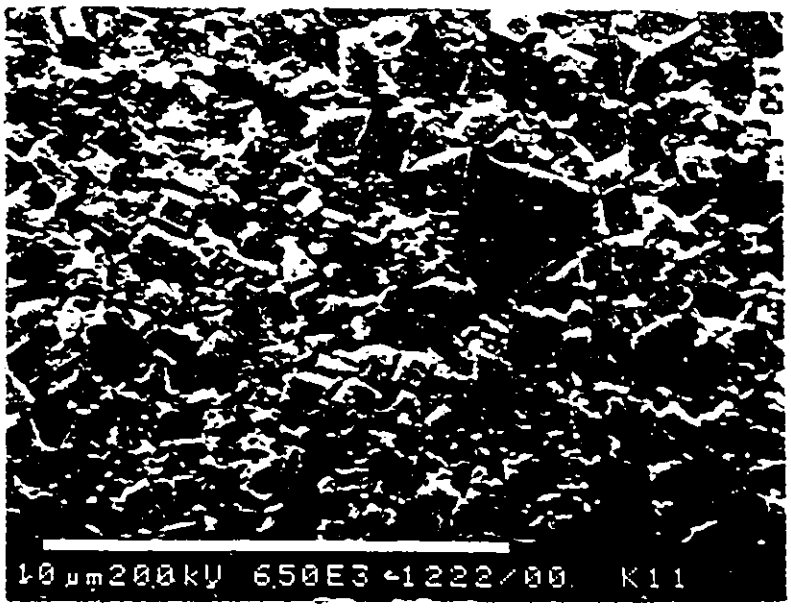

(a) K-11 Grade Tool

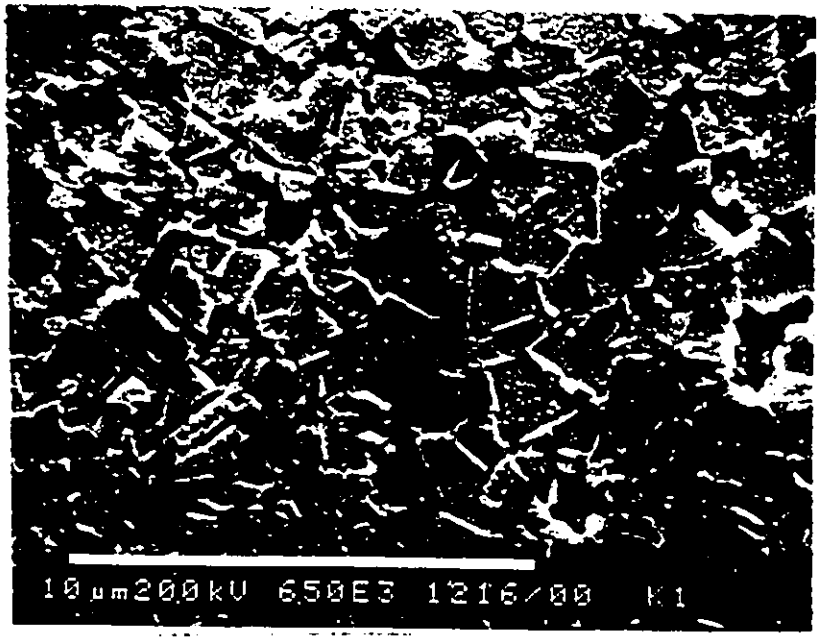

(b) K-1 Grade Tool

Fig.3.4 SEM photographs of the tool materials

only semi-orthogonal (restricted cutting) and the chips were observed to flow over the rake face of the tool at an angle of 70 degrees to the cutting edge rather than at 90 degrees for perfectly orthogonal conditions. This semi-orthogonality was accounted for by including the radial force in temperature calculations and by considering the tool-chip contact length in the direction of chip flow in thermokinetic calculations.

The lathe was surrounded by sheets of plastic during the wear tests. The hot chips got stuck onto these sheets, rather than bouncing off. This helped in chip collection during wear tests. All the chips were used in Instrumental Neutron Activation Analysis to quantify the amount of tool wear, and thus, the possibility of analyzed samples, not being representative of total sample was avoided.

3-C : Force Measurements - Dynamometry

This term is used to describe the techniques used for measuring the forces exerted on a cutting tool insert during a wear test. Various sensors can be used to determine the magnitude of forces during a cutting operation[33]. Strain gauges or piezo-electric crystals, for example, can be used. Accordingly, there are many types of dynamometer, each utilizing a particular sensing technique. The details regarding construction of various types of dynamometers are described elsewhere [1,33]. In the present work, a 3

component piezoelectric transducer type dynamometer, developed at McMaster University by C.T. Lai [66], was used.

Piezoelectric crystals possess a permanent electric dipole because the centers of the positive and negative charges are not located at the center of the unit cell of the crystal lattice. When force is applied to piezoelectric crystals, displacement of ions takes place leading to a change in the length of the electric dipole. When the crystal is under compression, such as during metal cutting, there is an excess of charge density on the two ends of the quartz crystal. The total amount of charge developed is proportional to the applied force and the constant of proportionality is the piezoelectric constant. Piezoelectric transducers have charge collectors attached to each side. Design of the dynamometer is such that whenever there exists a force acting on the bearing surface of the transducer, it is automatically resolved into its components, F_x, F_y and F_z. Each of these forces induces charges proportional to its respective magnitude. These charges are picked up by electrodes and are given as the output of the dynamometer.

The output of the dynamometer requires conditioning in order to convert it in a usable form. This is achieved electronically as shown in Fig.3.5. The charges generated by the piezoelectric crystal corresponding to the X,Y and Z force components are very small in magnitude, and are fed to charge amplifiers. Along with amplification, the charges are

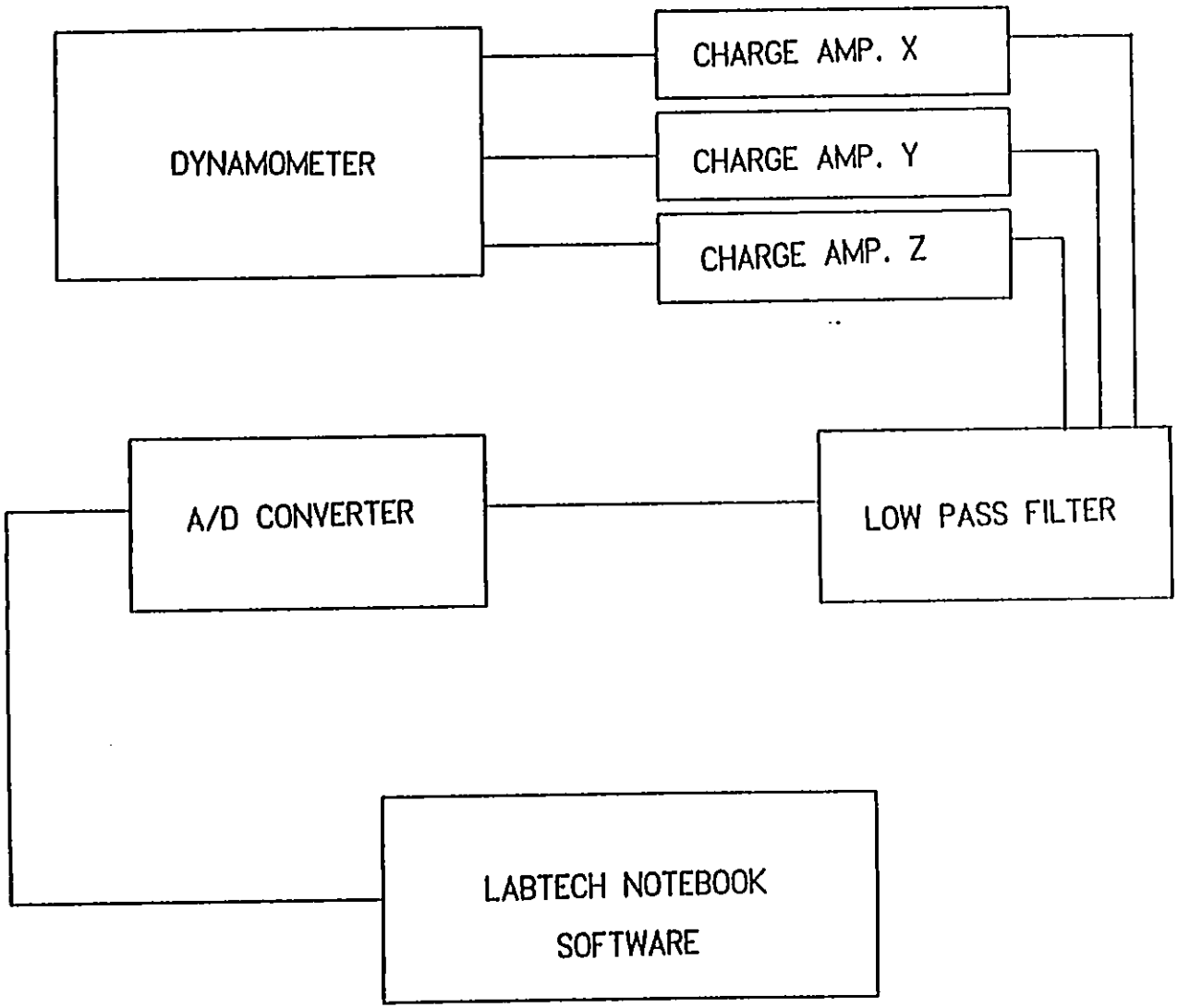

Fig.3.5 A schematic diagram showing the data acquisition set-up.

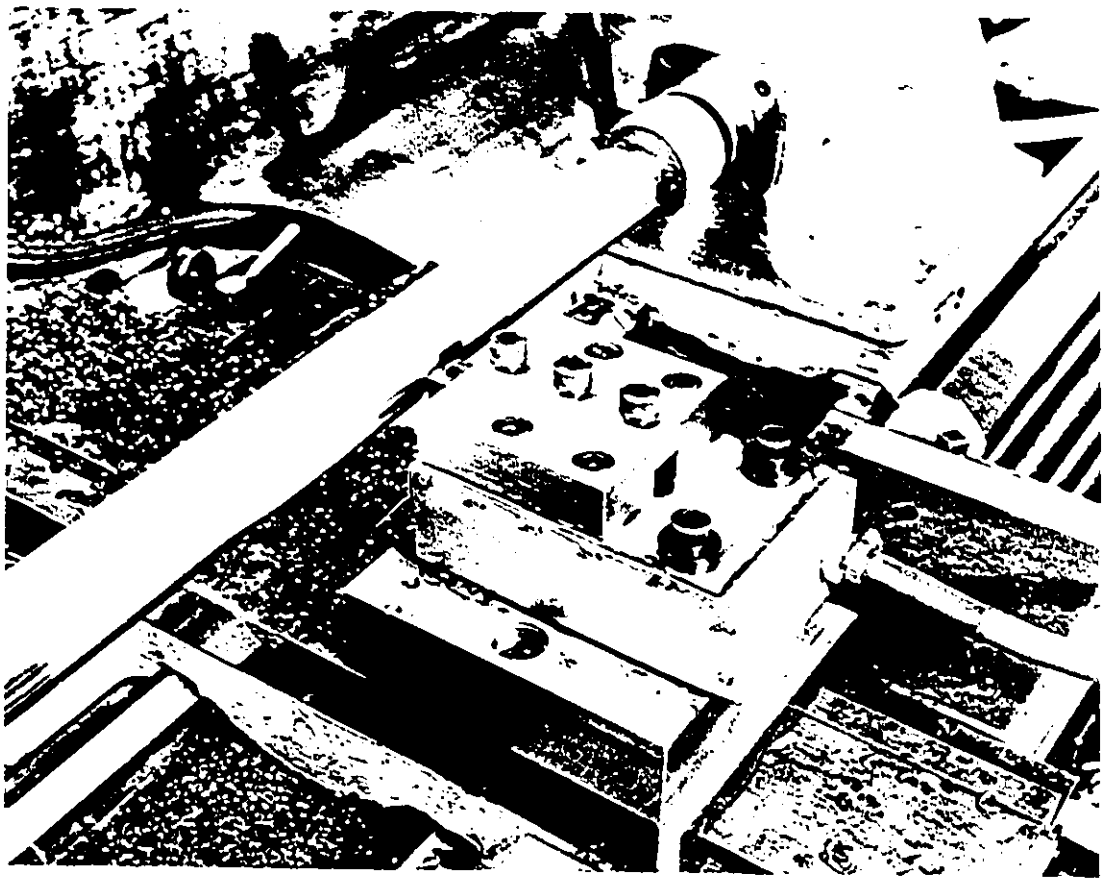

Fig.3.6 The 3-component piezoelectric dynamometer, used for force measurements.

also converted here into the corresponding voltage signals. The output of the charge amplifiers is fed to an analogue to digital converter through a low pass filter. During the cutting operation, because of the machine vibrations a lot of noise is generated along with the required signal. These unwanted signals are filtered out by means of the low pass filter, operating at a cut-off frequency of 50 Hz. The filtered signal is converted into a proportional digital signal by means of analogue to digital converter (ADC). Data acquisition was accomplished using the LABTECH NOTEBOOK software. The selection of a suitable acquisition frequency is important to get the best results. The maximum speed of operation of the lathe was about 1500 RPM which is equivalent to a frequency of 25 Hz. An acquisition frequency equal to 4 times this value, i.e. 100 Hz was selected for optimum data acquisition. Fig.3.6 shows a photograph of the dynamometer used for force measurements.

3-D : Quantification of Tool Wear: The INAA technique is well-established, and is used in this investigation to quantify tool wear. With recent developments in Nuclear Instrumentation, very good analytical accuracies, precisions and the detection limits have been achieved [67].

The concentration of tungsten and cobalt, inherently present in the workpiece material, was determined by INAA of 14 samples cut from different locations of the steel bars.

The average of these 14 values was considered in all further calculations. Maximum possible chips, generated during the wear tests, were collected. The tungsten and cobalt amounts present in the chips were determined by INAA. The tungsten amount includes the contributions from both the elemental (dissolved) and the chemically combined tungsten (WC fragments). The increase in the amount of tungsten, over that present in the workpiece material of the same weight, was taken to be the tool material transferred into the chips. Tool wear was determined by calculating the corresponding loss of tungsten carbide plus cobalt. To separate the embedded WC fragments, the chips were dissolved in hydrochloric acid and the solution was filtered through 0.2 μm filters. The filters were analyzed by INAA to determine the mechanical wear component.

3-D 1: The McMaster Nuclear Reactor and INAA Scheme

Chips collected during the wear tests were encapsulated in specially prepared polyethylene vials, which were subsequently packed in bundles and inserted in irradiation core for activation by thermal neutrons. Tungsten and cobalt standards, weighing 100 microgram each were also included in each bundle. The stack of vials was rotated about a vertical axis to ensure uniformity of the neutron flux, at a given depth in the irradiation core. There was some variation in neutron flux along the depth of

irradiation core. This variation was established using cobalt flux wires and the results were normalized to account for this variation. After irradiation, the chips were allowed to cool for 5 days and then the γ activity of the tungsten and cobalt isotopes of interest was determined, from which the corresponding concentrations were calculated. Cobalt concentrations were primarily determined for cross checking the results, as they were expected to increase only slightly over the baseline value corresponding to the cobalt concentration in the workpiece. Following conditions were maintained uniformly during all analyses :

Type of neutrons used : Thermal
Neutron flux : 10^{12}neutron/cm^2 s
Irradiation time : 90 min.
Cooling time : 5 days
Counting time : 900 second.

When subjected to a neutron flux, the elements present in the chip sample form their respective radioactive isotopes by a process of neutron absorption. The activity of a specific isotope produced in an irradiation time t, is given by the following equation :

$$A = N \phi \sigma (1-\exp(-\lambda t)) \qquad (3.1)$$

where, A is the activity of the nuclear species.

N is the number of atoms of that element.

ϕ is the irradiation flux.

σ is the neutron cross section.

λ is the decay constant of the isotope.

Thus, for a given element, e.g. tungsten, with the specific values of above parameters, the following relationship holds good :

$$\frac{^{187}W \text{ activity of standard}}{^{187}W \text{ activity of sample}} = \frac{\text{Amount of tungsten in standard}}{\text{Amount of tungsten in sample}} \qquad (3.2)$$

This is the underlying principle of Instrumental Neutron Activation Analysis. The activities involved in the above equation were measured using a sophisticated detection and counting system which is described in the next section.

3-D 2: Detection and Counting System

These are very important aspects of the technique, and primarily determine the quality of results. A block diagram representing the complete energy spectroscopy system used at the McMaster University Nuclear Reactor is shown in Fig. 3.7.

Detection System : A high purity germanium detector supplied by EG&G ORTEC was used to detect the γ rays (photons) emitted by various activated radio-isotopes. Fig.3.8 is a photograph, showing a chip sample mounted for γ counting

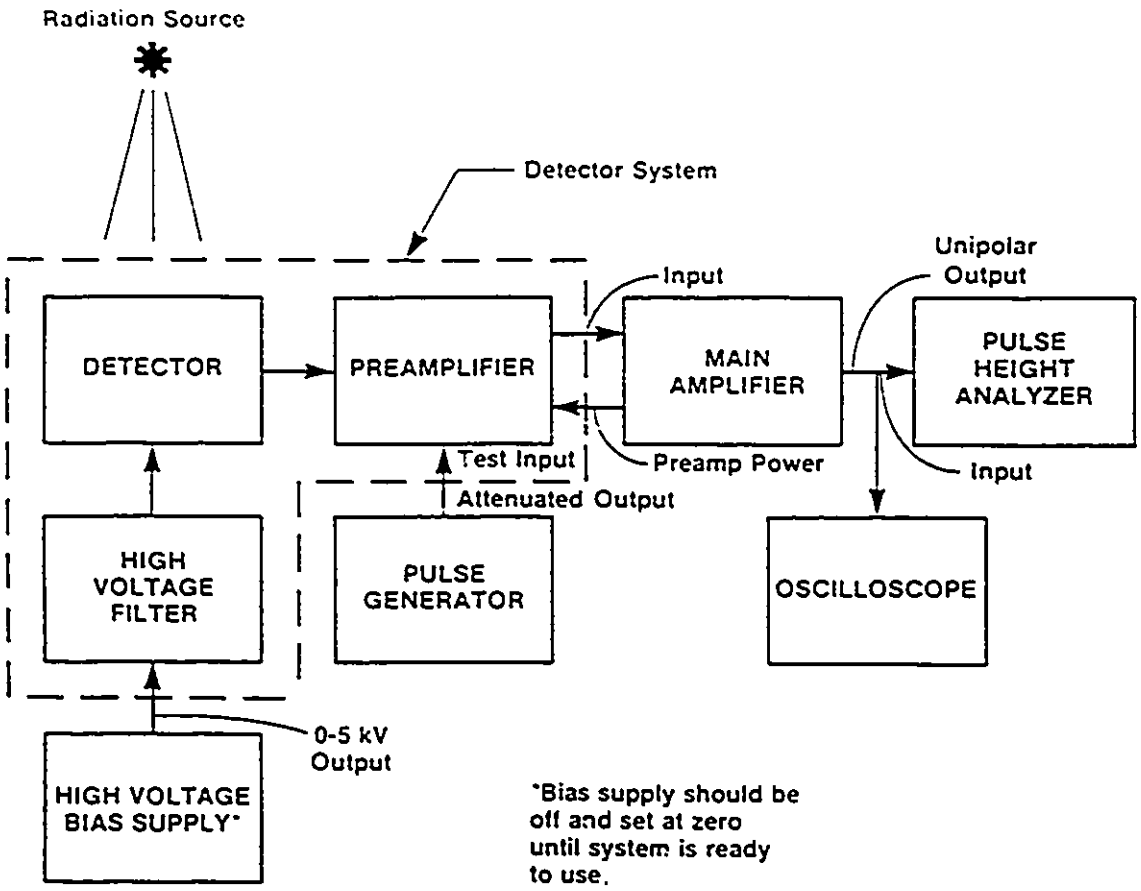

Fig.3.7 A schematic diagram showing the complete energy spectroscopy system used in INAA.

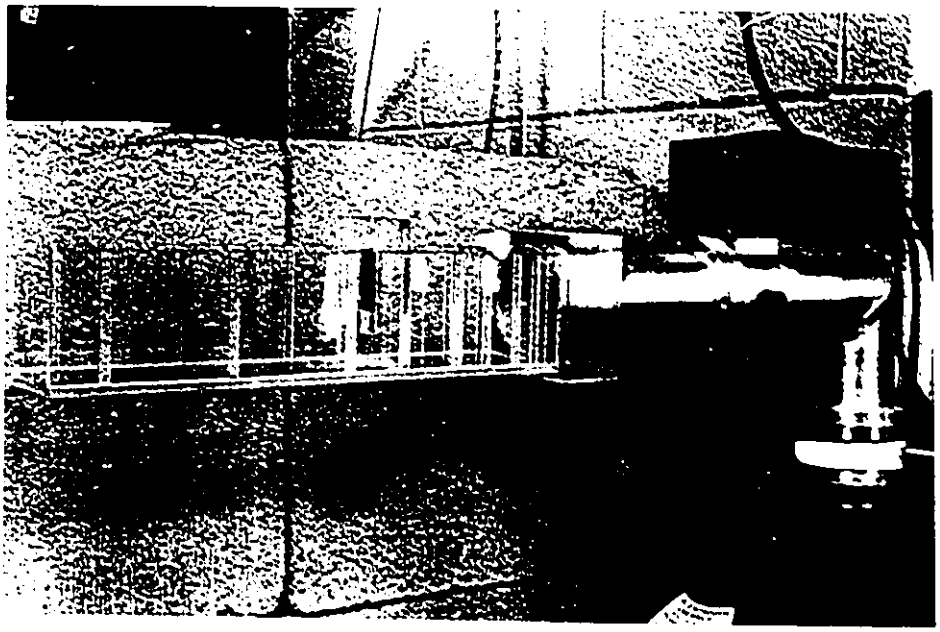

Fig.3.8 A high purity germanium detector used in INAA. A chip sample mounted in front of the detector can also be seen.

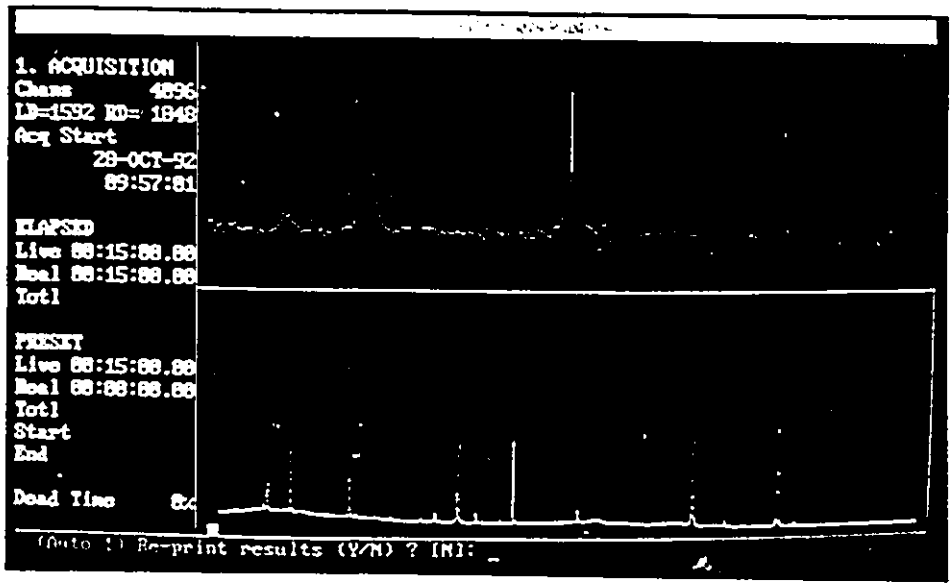

Fig.3.9 A typical γ spectrum obtained in INAA of a chip sample.

using the above detector. The photon detection system consists of the following parts:

1) Semiconductor detector element.
2) A cryostat which maintains the detector in vacuum.
3) A liquid nitrogen dewar.
4) A low noise charge sensitive preamplifier and a high voltage filter.

When a γ ray, i.e. a photon, enters a detector, it interacts with the ultra high purity germanium single crystal and produces a large number of electron hole pairs, depending on the energy of the photon. Under the influence of an applied voltage the electrons and holes move in opposite directions giving rise to a current pulse. The current pulse is integrated by a charge sensitive preamplifier producing an output pulse whose height is proportional to the incident photon energy. Each γ ray is, thus, registered as a voltage pulse with peak height proportional to the energy of the γ ray.

Detector resolution is an important consideration in the spectroscopic analysis. Ideally a sharp line is expected in the spectrum at the channel number corresponding to the energy of the γ ray, but the system noise and the inherent randomness of the electron-hole formation process results in line broadening. The resulting peak is spread over a few channels, and this spread determines the detector resolution. The resolution of a detector at a given γ ray

energy is expressed as the full width at half maximum (FWHM) of the observed peak as a percentage of the photon energy. The resolution of the detector used in the analysis was 1.75 keV at the 1.33 MeV peak of ^{60}Co.

Counting System : In all the experiments, a ND599 Loss Free Counting System, developed by Nuclear Data Inc., was used. When the rate of incoming γ rays is high, as in this case, an ordinary counting system is busy processing the signal corresponding to a given detection event for a substantial time during which counts will not register. Loss Free Counting system corrects for the system dead time. The ND599 system incorporates the Virtual Pulse Generator Technology, developed by Westphal, [68] which corrects for the dead time in real-time. This counting procedure is known as real time counting, and by using this procedure, counting times can be maintained short with good analytical precision. This counter can cope up with the rates of incoming γ rays up to 700 kHz. More details about the Virtual Pulse Generator technique for live time correction are given in ref.69.

Acquisition of Spectrum : When a γ ray interacts with the detector a current pulse is generated. Upon integration of the current pulse, a voltage pulse is obtained and is shaped by the amplifier. There may be a further amplification and pulse shaping by an additional amplifier. The output pulse

from this amplifier is fed to the pulse height analyzer where it is directed to an analogue to digital converter (ADC). The height of each incoming pulse is measured and a digital signal is produced which is proportional to the pulse height. The pulse height analyzer sorts the pulses and stores them by channel numbers according to their pulse heights. By this procedure, the entire energy spectrum corresponding to γ decay of the chip samples is obtained. Fig.3.9 shows a spectrum obtained using the above system.

3-E : Determination of Tool-Chip Contact Lengths/Areas

Tool-chip contact length and contact area at the end of a given machining time t, were determined from a photograph of the rake face of the cutting tool insert, used in the continuous cutting test for time t. The photograph was taken with an optical microscope at a magnification of 32X. Fig.3.10 shows a photograph of the rake face of the cutting tool insert, after a 7 second cutting time. The tool-chip contact area is clearly seen as the dark area in the photograph, and is determined graphically. The dark area in the photograph represents the projected tool-chip contact area. However, as the depth of the crater is very much lower than the other two dimensions, the projected area is approximately equal to the actual tool-chip contact area. An error of less than 10% is introduced by making this approximation. The shape of the crater is not perfectly

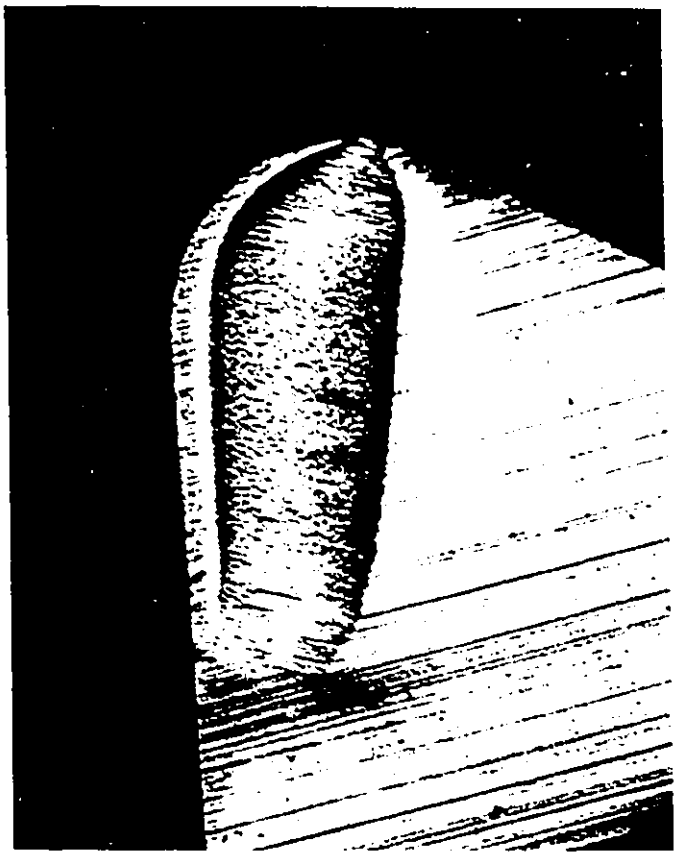

Fig.3.10 The rake face of a K-11 grade cutting tool used to machine Steel 1 for 7 seconds at 240 m/min. (Magnification : 32X)

ellipsoidal. Thus, the calculations of actual contact area, assuming a perfectly ellipsoidal shape are likely to lead to a higher error than 10% .

The width of the crater, used to determine the tool-chip contact length, was found to be somewhat non-uniform. It was measured at seven locations, and the average value was considered in the calculations of contact length. As stated previously, the chip flow direction made an angle of 20^{o} with the direction perpendicular to the cutting edge. The length of tool-chip contact in the direction of chip flow was taken to be the tool-chip contact length.

3-F : Microstructural Study of the Secondary Shear Zone

No special sample preparation was required for SEM examination, and as produced chip samples were used, after adequate cleaning. Special sample preparation for TEM examination is required, as the samples must be electron transparent. TEM samples of the material in the vicinity of tool-chip interface were prepared by the procedure of back polishing. The as produced chip samples were mounted in wax, and the bulk of the chip material removed by polishing, starting from the rough top surface of the chip. At the end of fine polishing using diamond paste, the sample thickness was about 60 micron. Further thinning was accomplished by conventional ion milling. In this technique, Argon ions

bombard both sides of the rotating sample at an angle, (12° to the sample surface in this case) thereby sputtering the surface. The final thickness of the electron transparent sample used for TEM analysis is about 150 nm.

3-G : Chemical Study of the Secondary Shear Zone

Concentration profiles of tungsten and cobalt next to the tool-chip interface were determined using Secondary Ion Mass Spectrometry [SIMS]. Water quenched chips were used for SIMS analysis. The pool of water was kept covered for the first 3 seconds of cut, and then the chips were collected in water for the next 2 seconds. The in flight time of the chips is estimated to be about 0.5 second.

SIMS is a well established surface analysis technique, especially known for its high sensitivity[70]. The following operating conditions were used :

Primary ions	: Oxygen
Angle of incidence	: 30° to surface normal
Rastered area	: 150 μm × 150 μm
Ion collection area	: 60 μm in diameter
Primary current	: 1280 nA
High voltage	: 13.7 kV

The quantification of SIMS data was accomplished in this investigation using an NBS standard. The following

composition of the standard was certified by NBS:

Element	Wt. %
C	0.163 + 0.001
Si	0.40
V	0.041
Ti	0.085
Nb	0.30
Ta	0.21
W	0.20
Co	0.30
Sb	0.012
Fe (Base)	95.477

CHAPTER 4 : EXPERIMENTAL RESULTS

4-A : Tool Wear Specification During Machining

The conventional way of describing the extent of crater wear during machining is by specifying the maximum depth of the crater which is formed on the rake face of the tool. A plot of maximum depth of crater versus the sliding distance (or time of cut) represents the crater wear characteristics of a given tool-workpiece combination. Fig.4.1(a) shows such crater wear characteristics of a K-11 (97 % WC) tool while machining Ca-treated AISI 1045 grade steel at 150 m/min. Fig.4.1(a) shows that the K-11 tool failed due to extensive cratering after 210 seconds of use which corresponds to a sliding distance of 22877 cm. It can be noted that no information regarding the weight of the material loss resulting in crater wear or regarding the volume of the crater can be derived from Fig.4.1(a) because of the geometric irregularity of the shape of the crater.

As explained in Chapter 3, the technique of INAA can be used to quantify the extent of tool wear during machining. Fig.4.1(b) represents the wear characteristics of the same tool-workpiece combination as before at the same cutting speed, but by using the method of INAA. Tool wear was quantified over a period of 120 seconds using all the

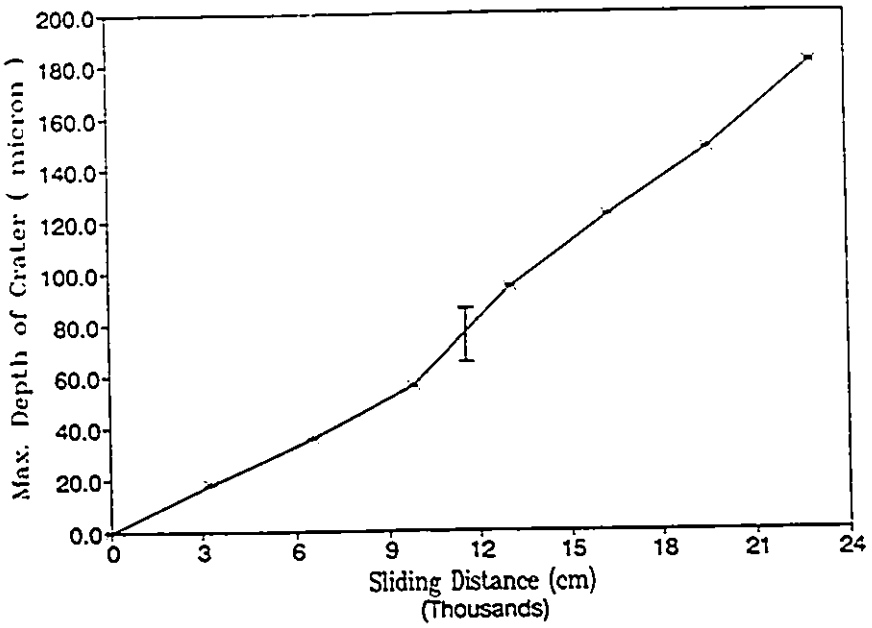

(a) Conventional method

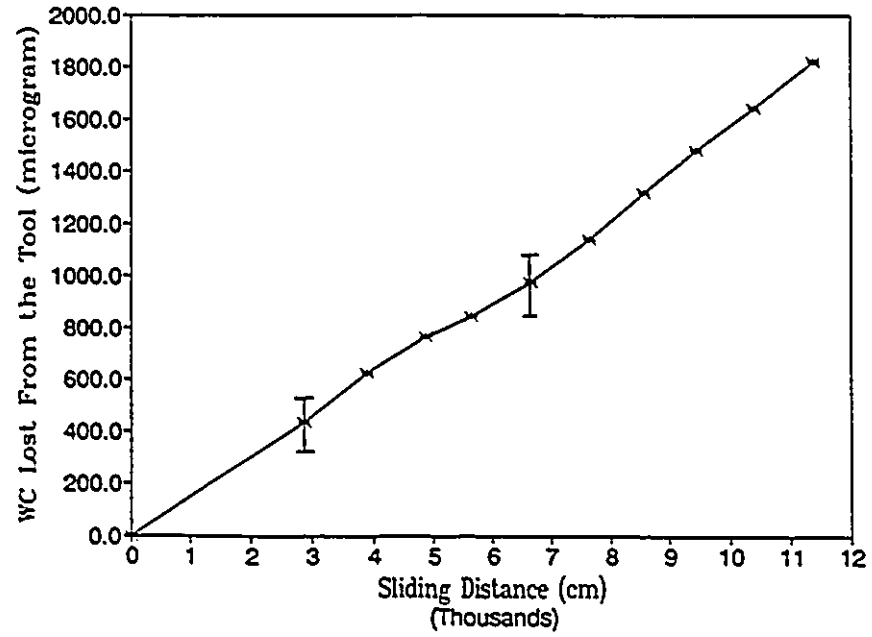

(b) INAA method

Fig.4.1 Determination of crater wear.

chips that could be collected during machining operation.

Comparison of Fig.4.1(a) and (b) shows that the two methods of tool wear measurement give compatible results. However, the INAA method gives a quantitative measure of the weight of the tool material lost as a result of wear. Under the conditions where crater wear is much higher than flank wear, the material lost from the rake face of the tool is very nearly equal to the total amount of tool loss. The tool-workpiece combination was selected in the present series of experiments on high speed machining whereby the above approximation could be justified. Quantification of crater wear in this manner laid the foundation for the development and evaluation of the quantitative model for dissolution wear to be described later.

4-B : Quantitative Database on Crater Wear

Table 4.1 shows the quantitative database generated using INAA. The amount of tool loss incurred during a wear test of 30 seconds using a K-11 tool and Ca-treated AISI 1045 grade steel workpiece combination is seen to be of the order of a few milligrams.

Table 4.2 shows the values of tool flank wear during these wear tests. By comparing the tool loss as a result of flank wear at each speed to the total amount of tool loss (flank + crater), it is easily seen that the dominant mode of tool wear for this tool-workpiece combination is crater

Table 4.1

Materials loss from the K-11 grade tools after machining a Ca-treated 1045 steel (steel 1) for 30 seconds.

Cutting speed (m / min)	Wt. of the chips collected (gm)	Average increase in conc. of W of the chips (ppm)	Loss of Tool (μgm)
150	179.8	2.3 ± 0.5	444 ± 97
180	232.8	5.0 ± 0.5	1230 ± 124
200	249.2	6.3 ± 0.5	1726 ± 138
220	262.8	8.6 ± 0.5	2478 ± 141
240	294.4	11.2 ± 0.5	3708 ± 158

Table 4.2

Contributions of flank wear to the tool loss.

Cutting speed (m / min)	Flank Wear V_b (mm)	Tool loss (μgm)	Tool loss due to Flank Wear (μgm)
150	0.06	444 ± 97	11.0
180	0.06	1230 ± 124	11.0
200	0.11	1726 ± 138	37.2
220	0.12	2478 ± 141	44.2
240	0.13	3708 ± 158	51.9

wear. Hence, as a first approximation, tool loss due to crater wear is taken to be equal to total tool loss.

Table 4.3 gives the crater volumes calculated from the weights of the material removed from the rake face of the tools during each wear test. It can be noted that these volumes are of the order of 10^{-5}cc. These small numbers underscore the difficulty in measuring the volume of craters by other means. It can also be noted from the database generated, that tool wear is greater at a higher cutting speed during wear tests of fixed time duration.

4-C : Mechanical Wear Versus Dissolution Wear

The total amount of tool wear was separated into a mechanical wear component and a dissolution wear component, as described in the previous chapter. Table 4.4 shows the amounts of mechanical wear and dissolution wear at each cutting speed. The major contribution to tool wear is clearly seen to arise from dissolution wear. The data of Table 4.5 show that the percentage contribution of dissolution wear toward the total tool wear increases with increasing cutting speed. At the highest cutting speed investigated (240 m/min), the percentage contribution of dissolution wear is as high as 93.4 % of the total tool wear. Thus, the dominance of a dissolution wear mechanism at high cutting speeds can be quantitatively established using INAA.

Table 4.3

The K-11 grade tool crater volumes after machining Steel 1 for 30 seconds

Cutting Speed (m/min)	Distance slid (cm)	Volume of Crater X 10^{-6} (cm^3)
150	2870	29 ± 6
180	3843	77 ± 7
200	4156	112 ± 9
220	4372	160 ± 9
240	4962	225 ± 10

Table 4.4

Contributions of the mechanical and the dissolution wear to the total crater wear.

Cutting speed (m/min)	Total WC lost from the tool (μgm)	WC loss due to mechanical wear (μgm)	WC loss due to dissolution wear (μgm)
150	432 ± 97	145 ± 1	287 ± 97
180	1238 ± 124	150 ± 1	1088 ± 124
200	1682 ± 134	187 ± 1	1495 ± 134
220	2415 ± 141	220 ± 1	2193 ± 141
240	3517 ± 158	234 ± 1	3283 ± 158

Table 4.5

Percentage contributions of the mechanical and the dissolution wear to the total crater wear

Cutting Speed (m/min)	% Mechanical wear	% Dissolution wear
150	33.6	66.4
180	12.1	87.9
200	11.1	88.9
220	9.2	90.8
240	6.6	93.4

4-D : Influence of Cutting Speed on Wear Rates

A normalized crater wear rate is defined as the volume lost as a consequence of the wear process per unit length of the chips slid over the rake face of the tool. (Units: cc/cm) Normalized crater wear rates were calculated from the quantitative database generated by INAA and were used to study the influence of cutting speed on crater wear processes. Cutting speed has a profound influence on the normalized crater wear rates, as can be seen from Fig.4.2(a). The total wear rate has been separated into the contributions resulting from mechanical wear and that from dissolution wear. These two types of wear mechanisms are seen to respond very differently to an increase in cutting speed. This difference in the two mechanisms is discussed further in Chapter 6.

The amounts of mechanical wear and dissolution wear can be used to calculate the average increase in the tungsten concentration of the chips as a consequence of the two types of wear mechanisms. This gives another way of comparing the crater wear rates at the five speeds investigated. The results are shown in Fig.4.2(b). This representation of the crater wear rates makes the wear rates easy to perceive. It can be seen that Fig.4.2(a) and (b) differ only by a scale factor, as they are two different ways of looking at the same process.

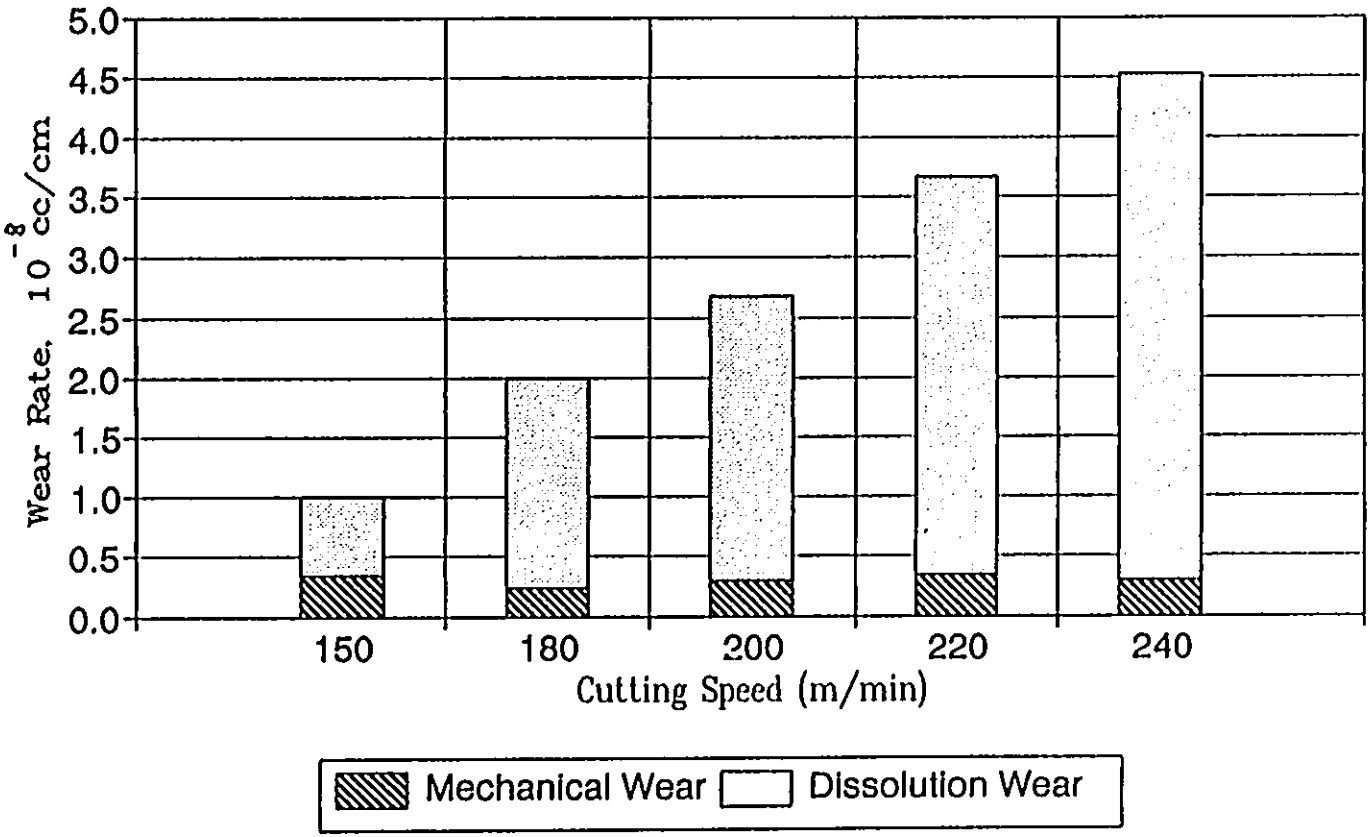

Fig.4.2(a) The normalized crater wear rates of the K-11 grade tools while machining Steel 1 at various speeds.

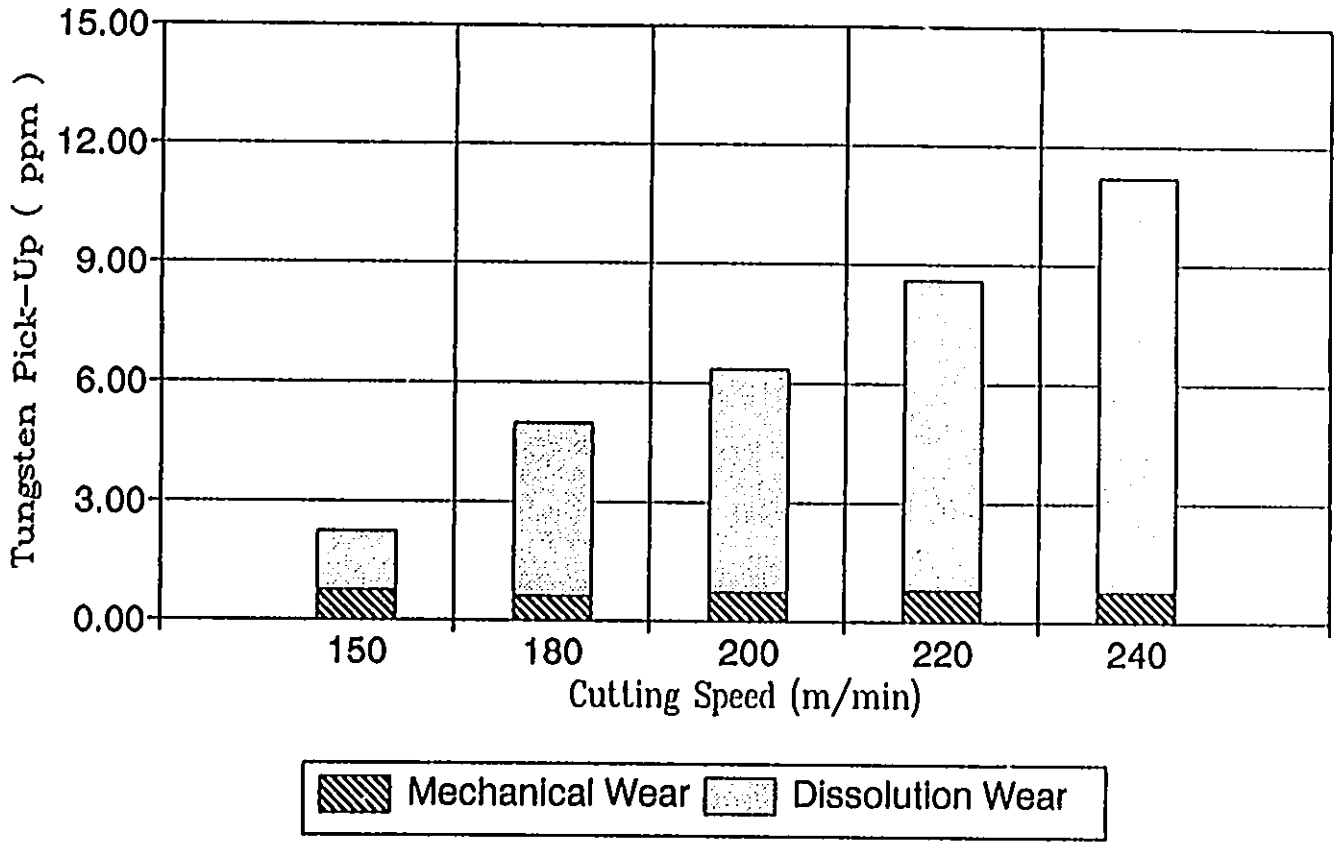

Fig.4.2(b) The average increase in the tungsten concentration of the chips produced by machining Steel 1 with the K-11 tools.

4-E : Average Tool-Chip Interface Temperatures

4-E.1 : Role of Interface Temperatures

It is known that the tool-chip interface temperatures increase with an increase in the cutting speed. Fig.4.3 shows the variation of average tool-chip interface temperatures existing at the start of the cutting operation, as a function of the cutting speed. Boothroyd's model for temperature distributions and the empirical relationships suggested by Hastings *et al.* were used in the calculations of the average tool-chip interface temperature. The details of these calculations are given in Appendix I. The increase in the tool-chip interface temperatures and the accompanying sharp increase in dissolution wear clearly indicates the involvement of thermally activated processes in the dissolution wear of cutting tools. Therefore, the establishment of tool-chip interface temperatures during machining must be the first step in the development of a quantitative model for dissolution wear.

4-E.2 : Temperature Rise During Wear Tests

It has been pointed out that crater wear is very rapid when a K-11 tool (97 % WC) is used to machine an AISI 1045 grade steel at high cutting speeds. Consequently, the tool-chip contact lengths and the forces exerted on the tool increase appreciably during the course of a 30 second wear test. These parameters directly influence the temperatures

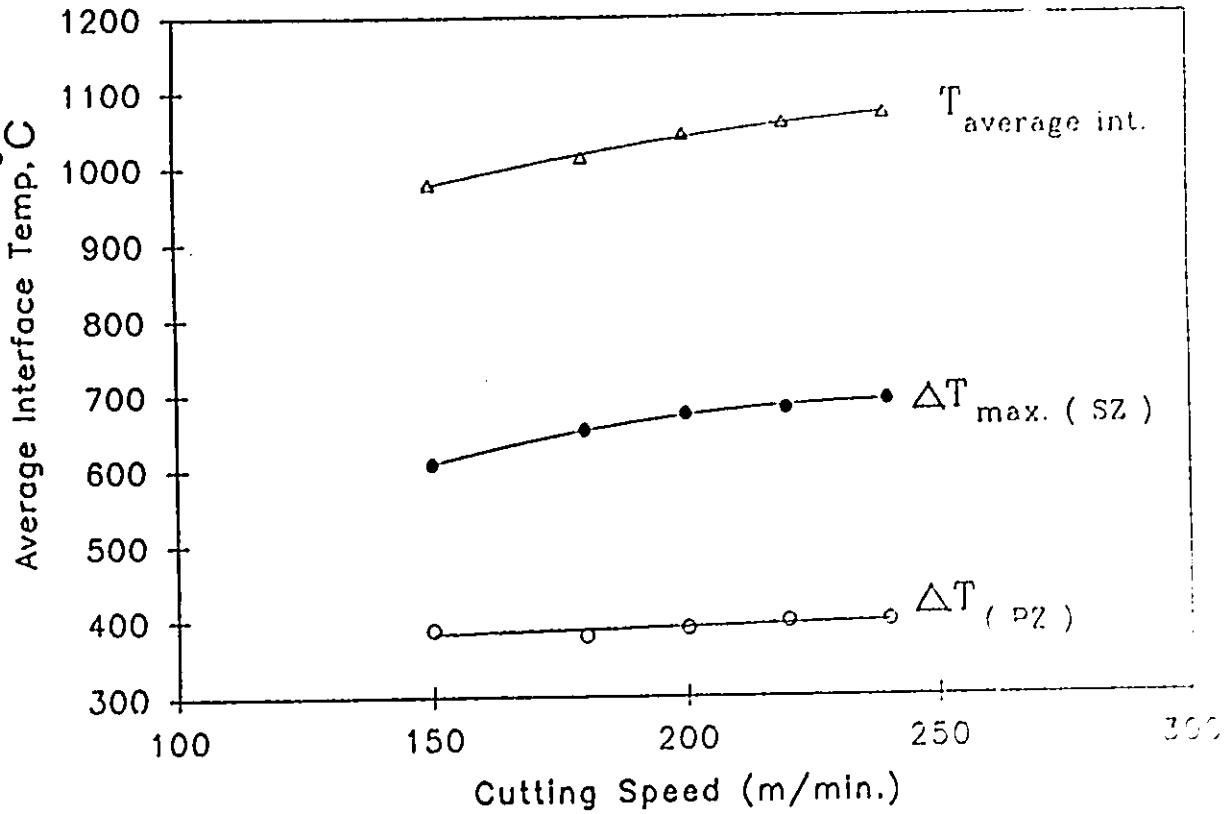

Fig.4.3 Influence of cutting speed on temperatures of importance in metal cutting.

at the tool-chip interface. It is, therefore, necessary to study the behaviour of these two parameters and establish the tool chip interface temperatures over the entire duration of a wear test.

Fig.4.4(a) to (e) show the cutting, feed and radial forces exerted on the tool during wear tests conducted at the cutting speeds of 150 m/min to 240 m/min. Force measurements were carried out with a 3 component piezoelectric dynamometer using the procedure outlined in Chapter 3. The increase in forces during the course of a 30 second wear test is seen to be quite significant.

Fig.4.5 shows the increase in tool-chip contact length during the course of wear tests conducted at cutting speeds of 150 m/min to 240 m/min. This increase in contact length reflects itself in a corresponding increase in the tool-chip contact areas, as shown in Fig.4.6. Consequently, there is an increase in the force opposing the motion of chip over the rake face of the tool. In other words, the increase in forces shown in Figs.4.4(a) to (e) is due to an increase in the tool-chip contact length. As reported previously, flank wear in each wear test is almost negligible. Therefore, the observed increase in forces during the course of a wear test can not be attributed to flank wear.

The ratio of the width of the secondary shear zone to the thickness of the chip, denoted by δ, is an important

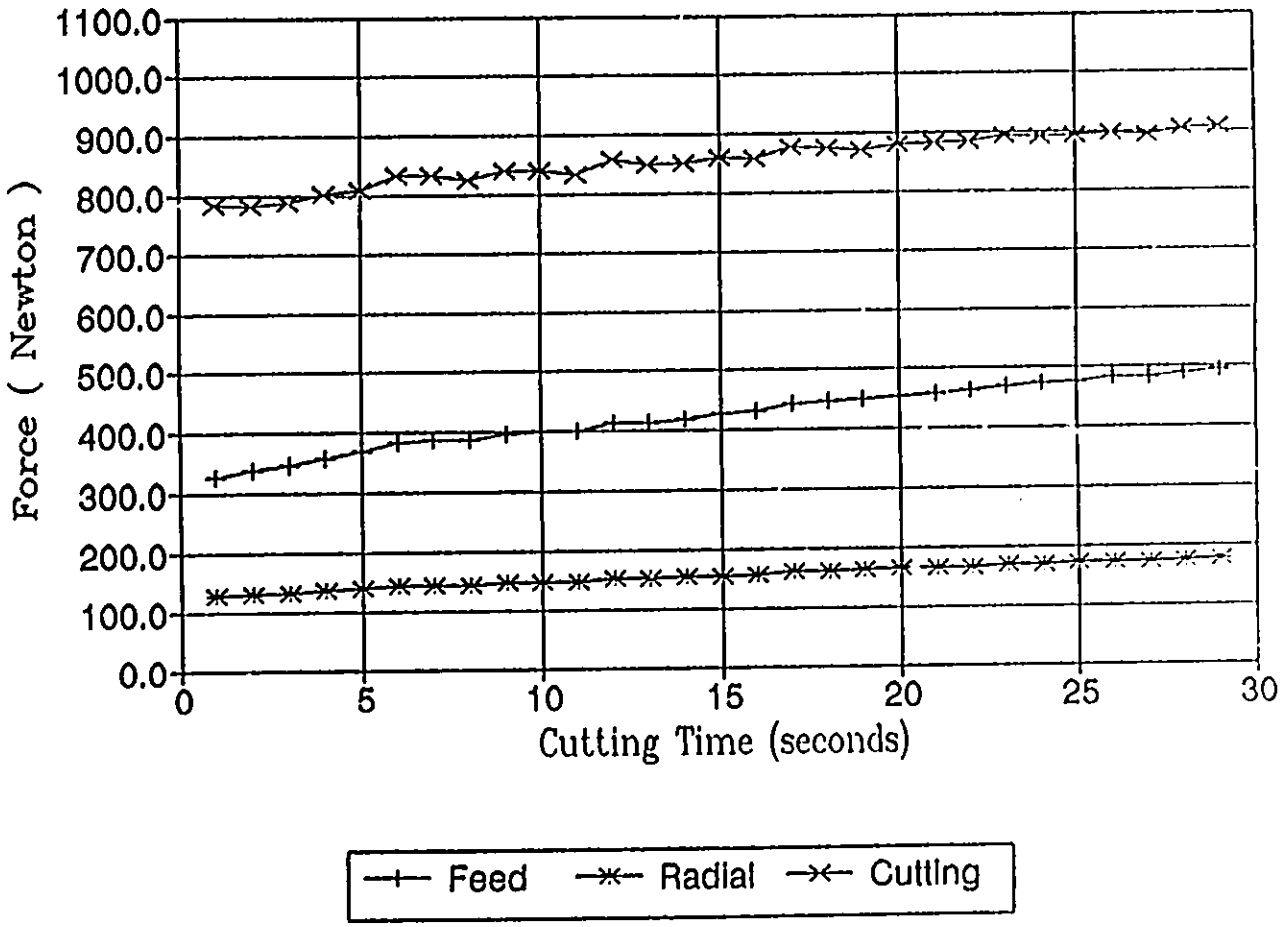

(a) 150 m/min

Fig.4.4 (a)-(e) The Variation of experimentally measured forces while machining Steel 1 with the K-11 grade tools from 150 to 240 m/min.

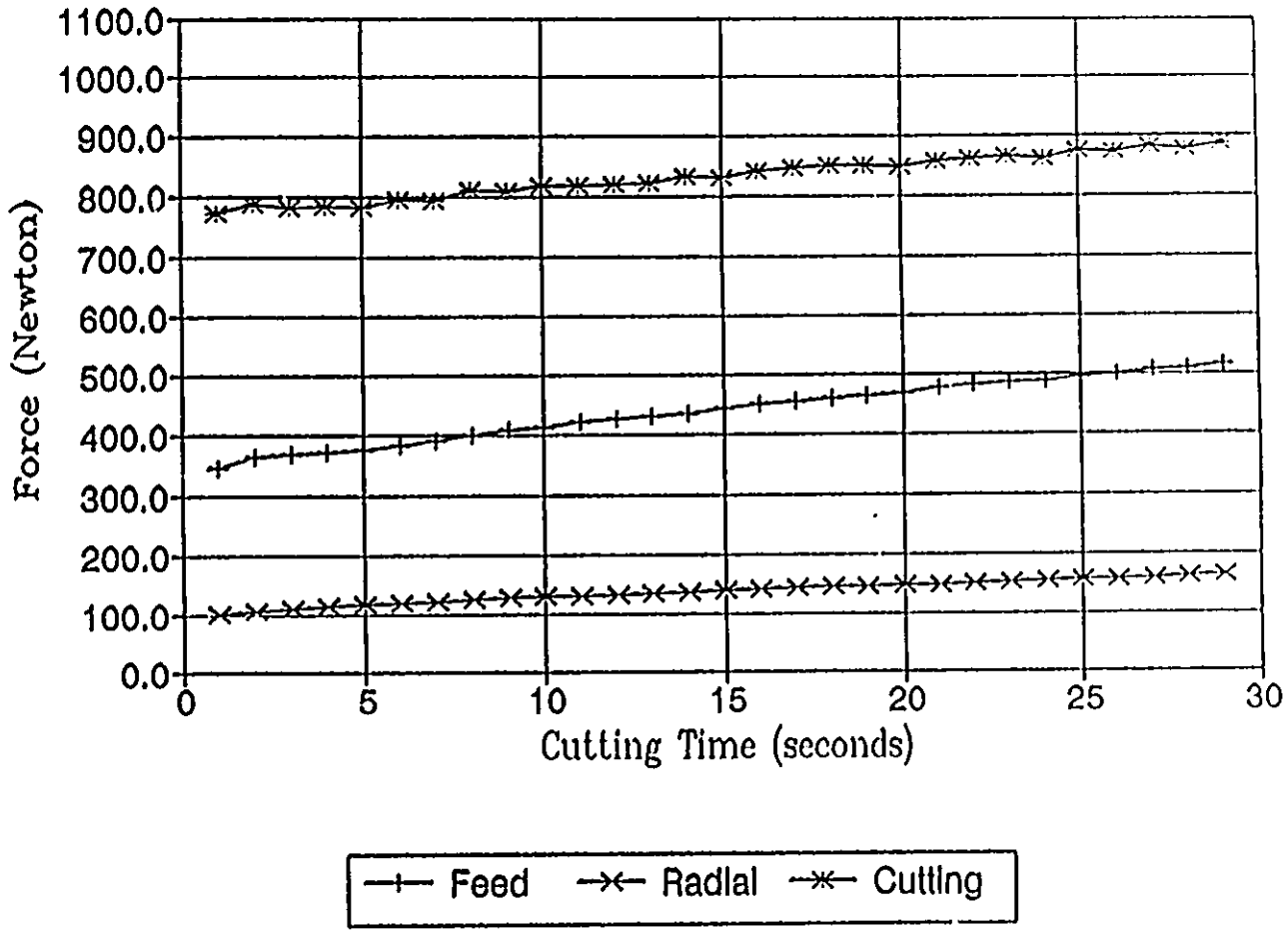
1100.0
1000.0
900.0
800.0
700.0
600.0
500.0
400.0
300.0
200.0
100.0
0.0
Force (Newton)
0
5
10
15
20
25
30
Cutting Time (seconds)
Feed
Radial
Cutting

(b) 180 m/min

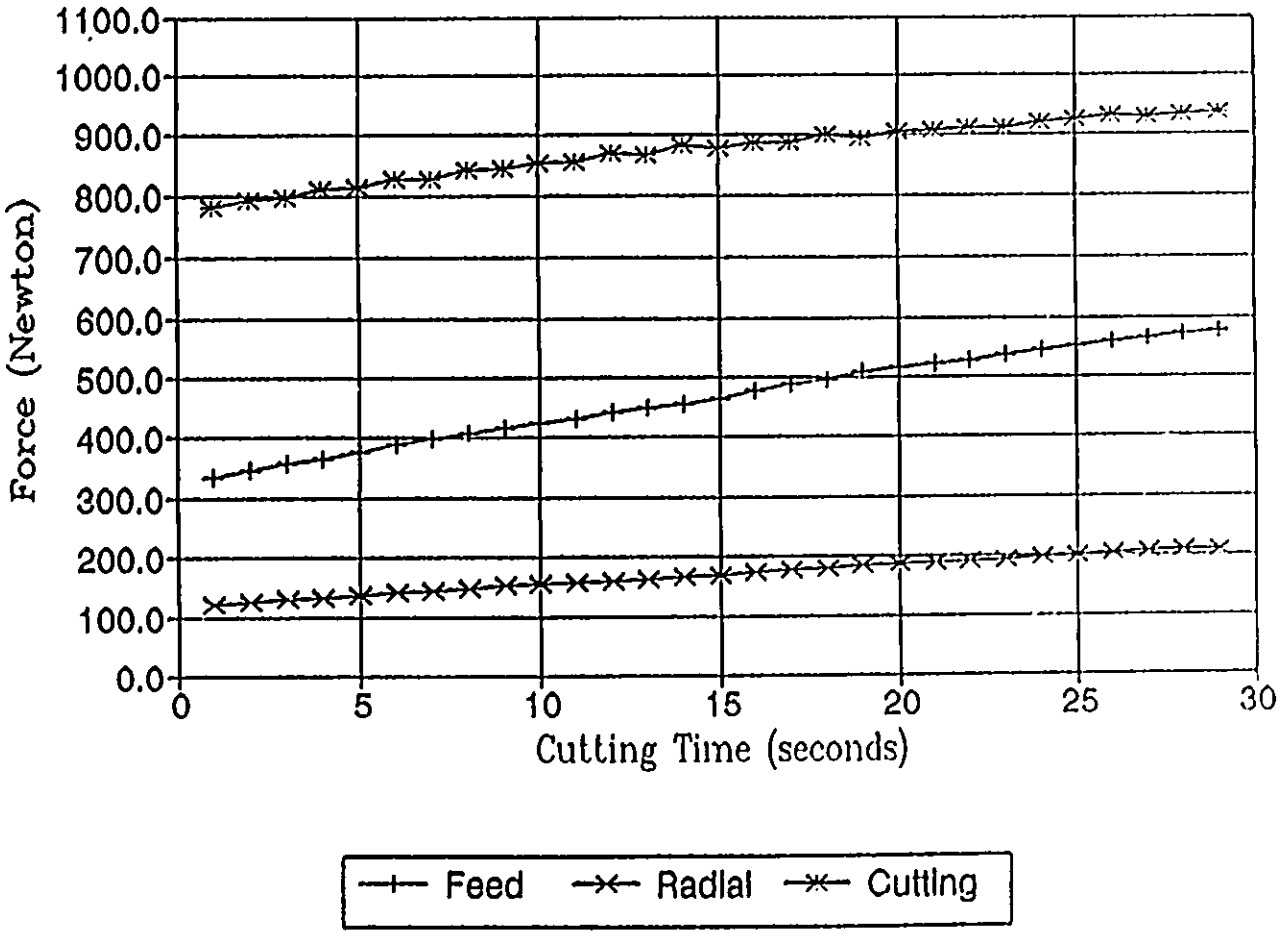
1100.0
1000.0
900.0
800.0
700.0
600.0
500.0
400.0
300.0
200.0
100.0
0.0
Force (Newton)
0
5
10
15
20
25
30
Cutting Time (seconds)
Feed
Radial
Cutting

(c) 200 m/min

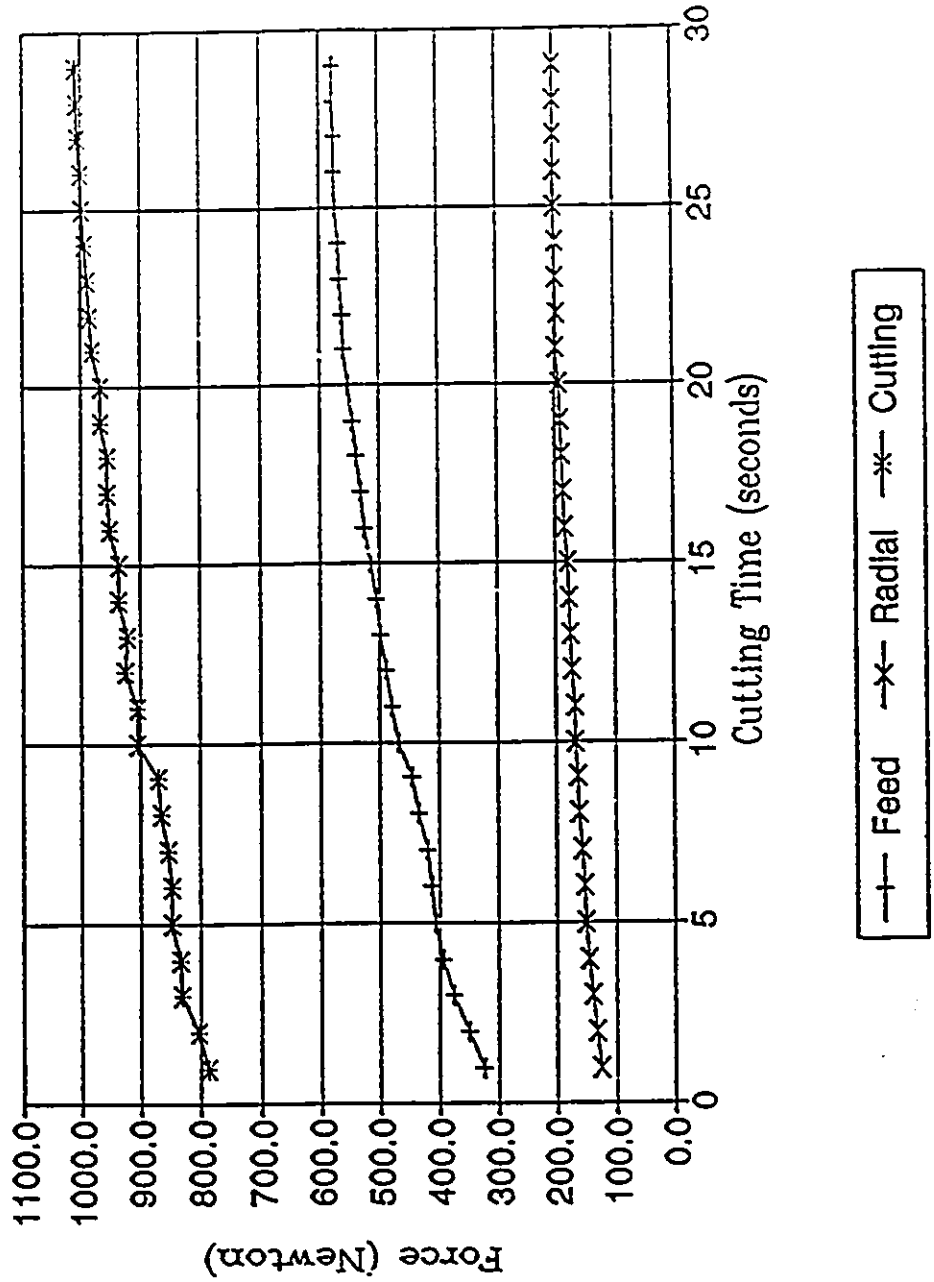
Force (Newton)
1100,0
1000,0
900,0
800,0
700,0
600,0
500,0
400,0
300,0
200,0
100,0
0,0
0
5
10
15
20
25
30
Cutting Time (seconds)
Feed
Radial
Cutting

(d) 220 m/min

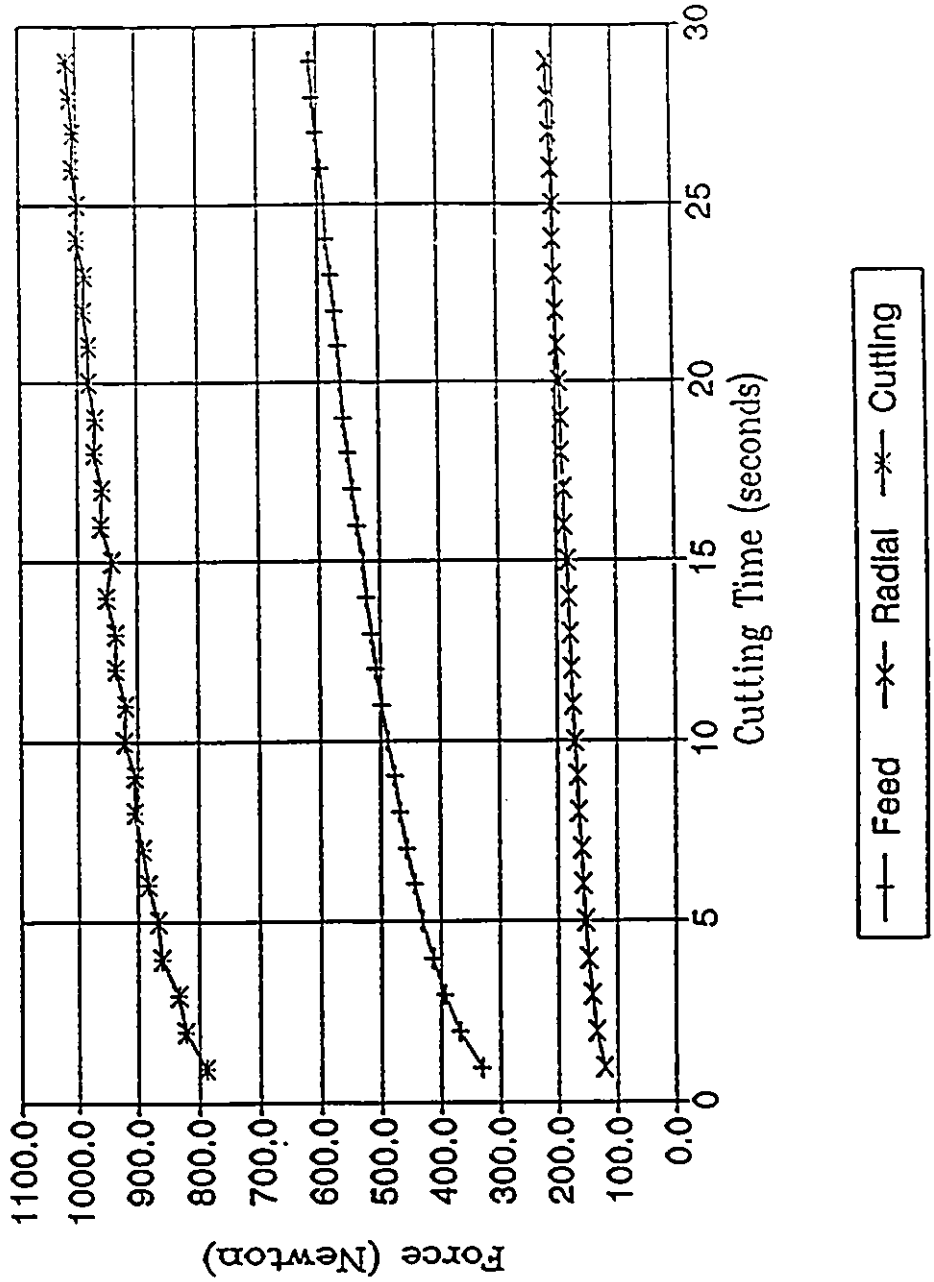
Force (Newton)
1100.0
1000.0
900.0
800.0
700.0
600.0
500.0
400.0
300.0
200.0
100.0
0.0
0
5
10
15
20
25
30
Cutting Time (seconds)
Feed
Radial
Cutting

(e) 240 m/min

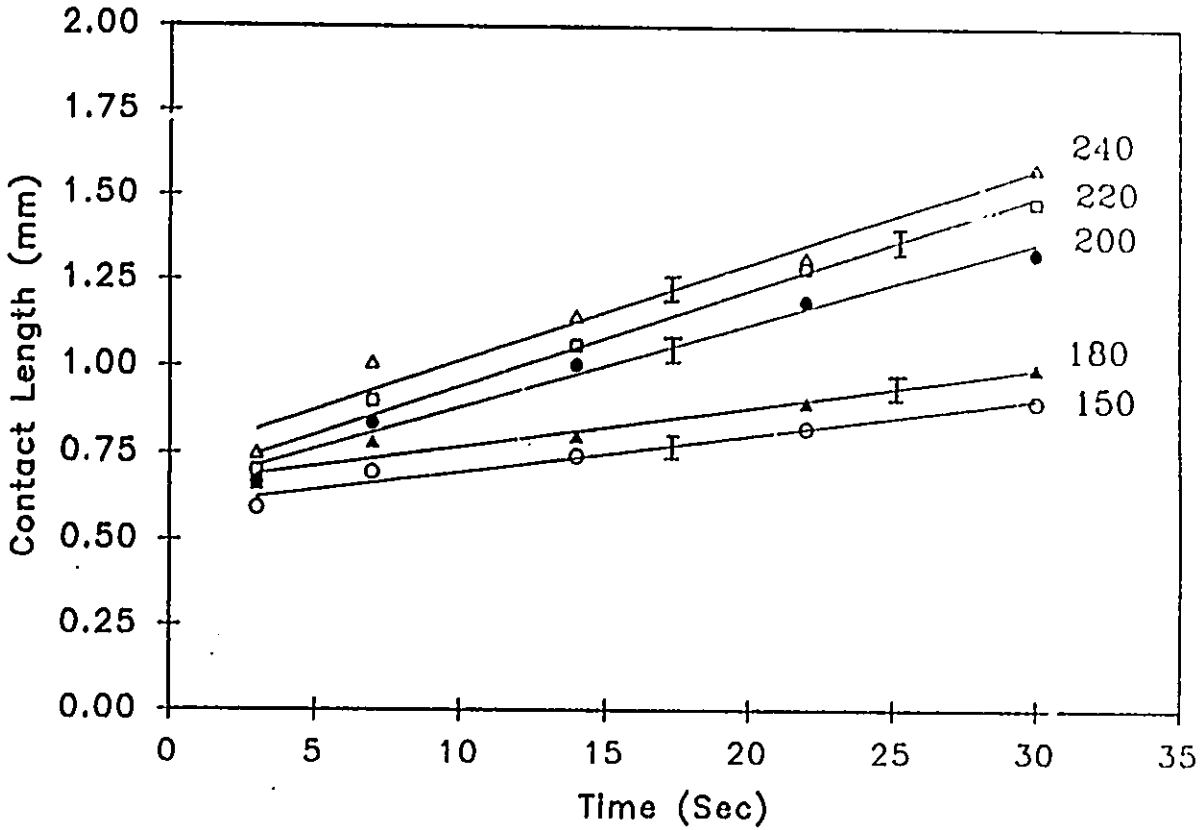

Fig.4.5 The variation of tool chip contact lengths during wear tests using K-11 grade tools and the Steel 1 workpiece.

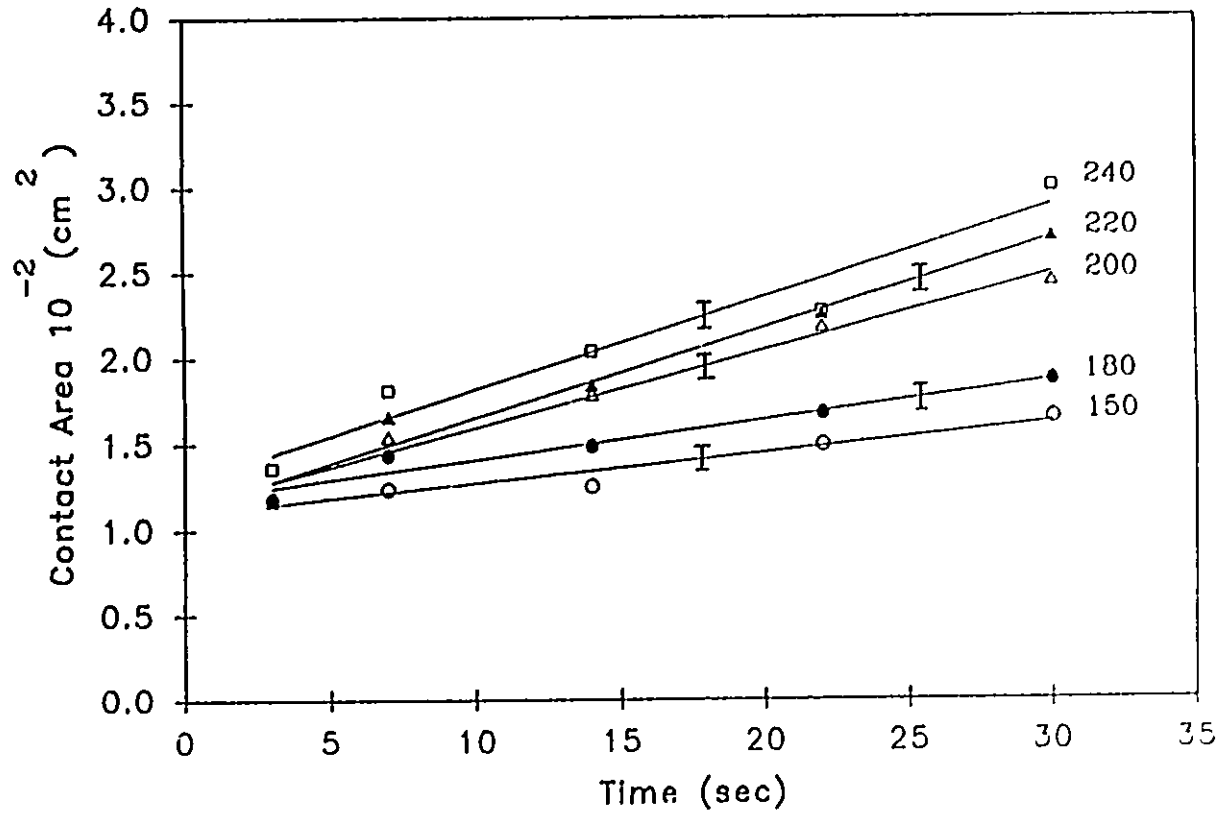

Fig.4.6 The variation of tool-chip contact areas during wear tests using K-11 grade tools and the steel 1 workpiece.

parameter influencing the tool-chip interface temperatures. Fig.4.7(a) and (b) show the cross sections of the chips generated at 150 m/min and 240 m/min respectively. The width of the secondary shear zone is taken as the depth from the tool-chip interface upto which the flow lines are curved. The value of the ratio 'δ' was found to be equal to 1/11 at all the cutting speeds employed in this investigation. It must be pointed out however, that due to the waviness of the top surface of the chips, an average value of the chip thickness as measured from the photograph has to be used in the calculations of the ratio 'δ'. As a consequence of this surface roughness, small changes in the value of 'δ' are masked and hence remain undetected.

Fig.4.8 shows the variation of average tool-chip interface temperatures during the course of a wear test at the five cutting speeds employed in this investigation. These temperatures were obtained using Boothroyd's model and the empirical relations suggested by Hastings et al. It is seen that the average tool-chip interface temperatures increase appreciably as a function of cutting time in a wear test of 30 seconds. As pointed out previously, the increase in temperatures is because of the increase in contact areas and forces resulting from the rapid crater wear of the cutting tools.

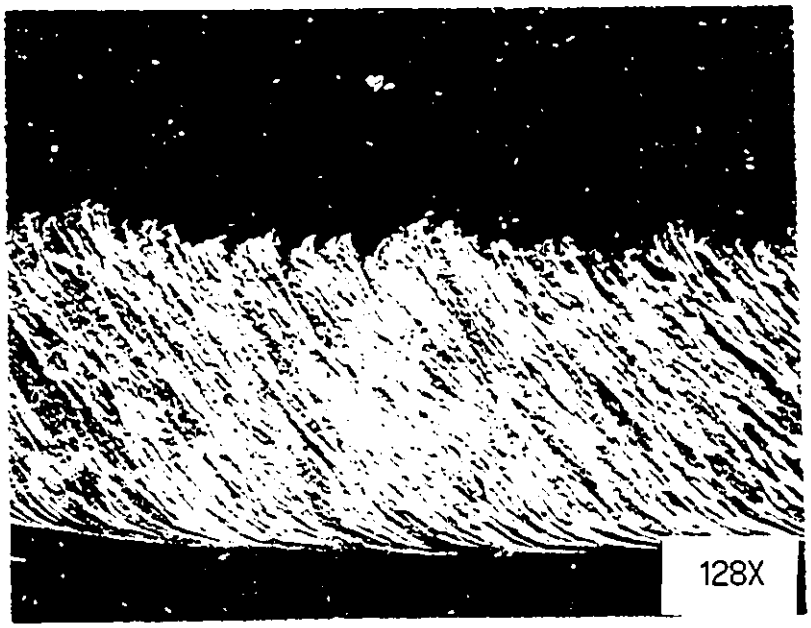

(a) 150 m/min

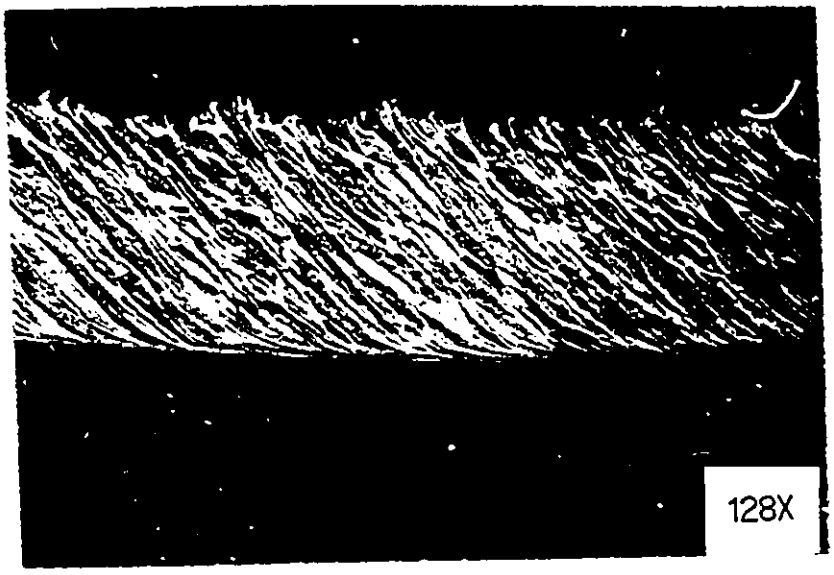

(b) 240 m/min

Fig.4.7 Cross sections of the Steel 1 chips produced in machining by the K-11 grade tools.

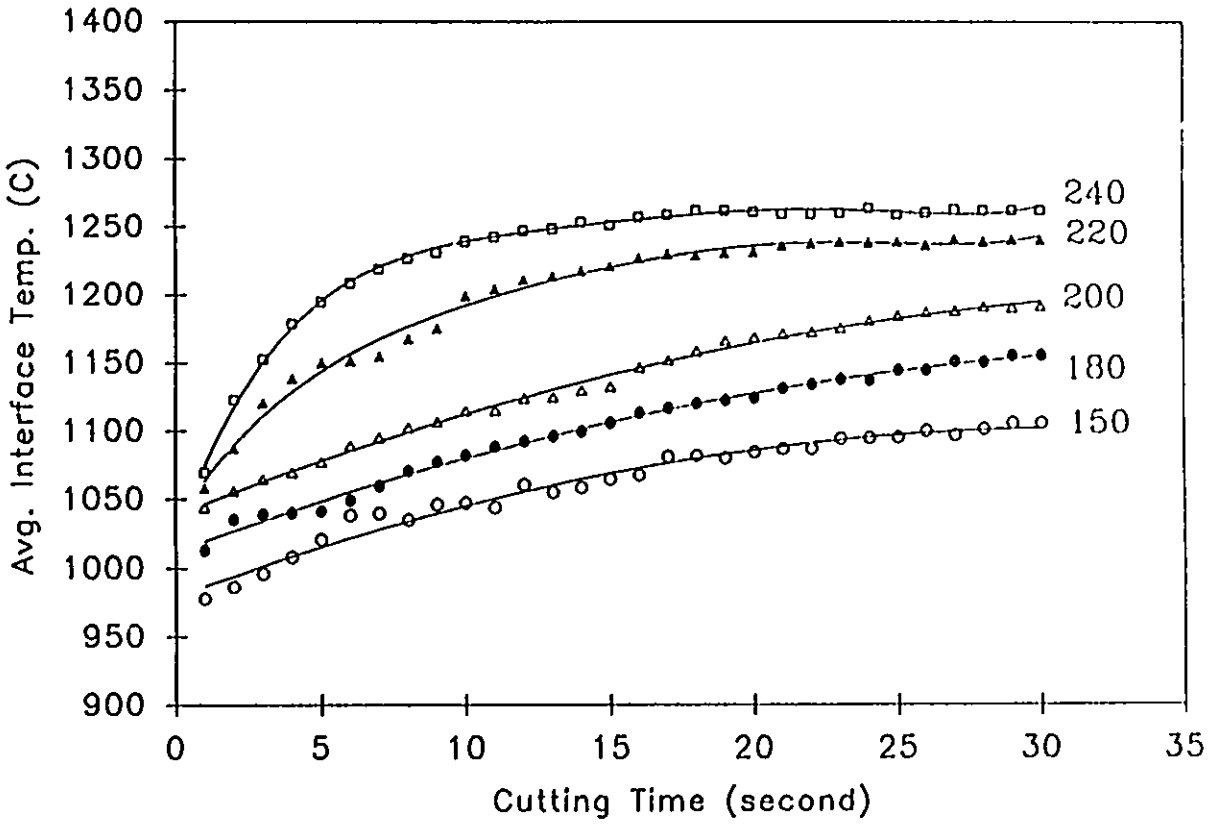

Fig.4.8 The increase in the average tool-chip interface temperatures during the machining of Steel 1 by the K-11 grade tools.

4-F : Evidence for a Dissolutional Process at the Interface

It was mentioned in Section 4-E that thermally activated processes are involved in the dissolution wear of cutting tools. Diffusional material transport away from the tool-chip interface is such a thermally activated process. Figs.4.9(a) to 4.11(a) show the concentration profiles of tungsten in the chip material near the tool-chip interface. Figs.4.9(b) to 4.11(b) show the concentration profiles of cobalt in the same chips. These chips were produced by machining at 150, 200 and 240 m/min respectively, and were quenched in water close to the tool tip. The same tool-workpiece combination as reported in the previous wear tests was used. It is estimated that the in flight time of the chips prior to quenching in water is of order of 0.5 second. In this time, the original profiles are altered due to solute redistribution. However, the profiles clearly show the presence of elemental tungsten in the chip material, thereby proving the occurrence of the process of tool dissolution. The maximum concentration of the dissolved species is observed very close to the tool-chip interface. It can be seen that the maximum concentration of tungsten as well as the depth of penetration of tungsten into the chips increase as the cutting speed (and hence the temperature) is increased. However, the maximum concentration in the case of both tungsten and cobalt profiles is not exactly at the interface, but at a depth of about 0.08 microns into the

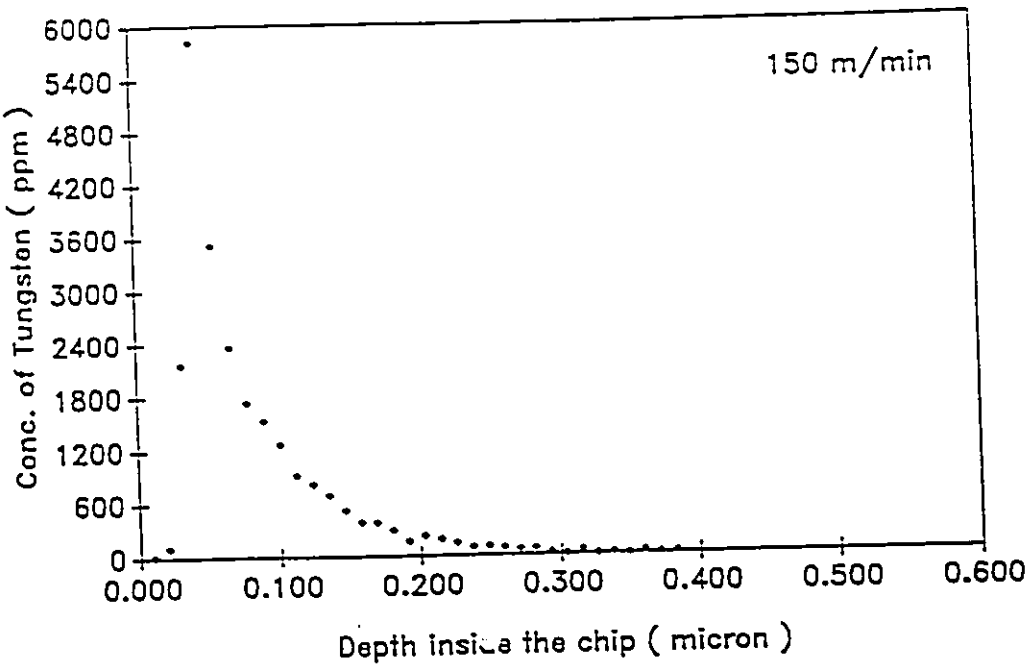

(a)

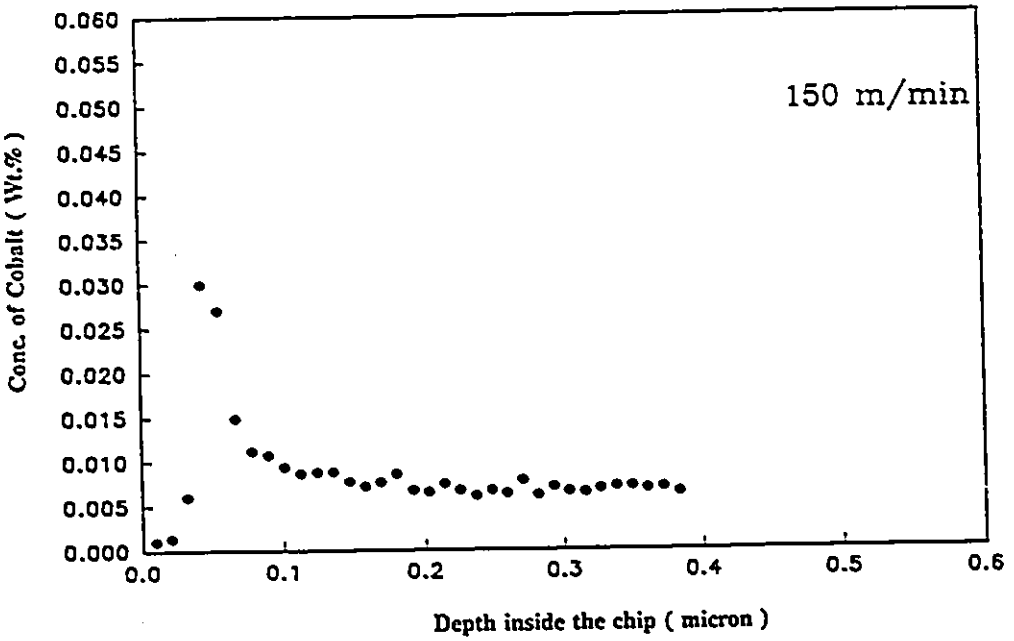

(b)

Fig.4.9 The concentration profiles of (a) tungsten and (b) cobalt in a quenched Steel 1 chip produced by a K-11 grade tool at 150 m/min.

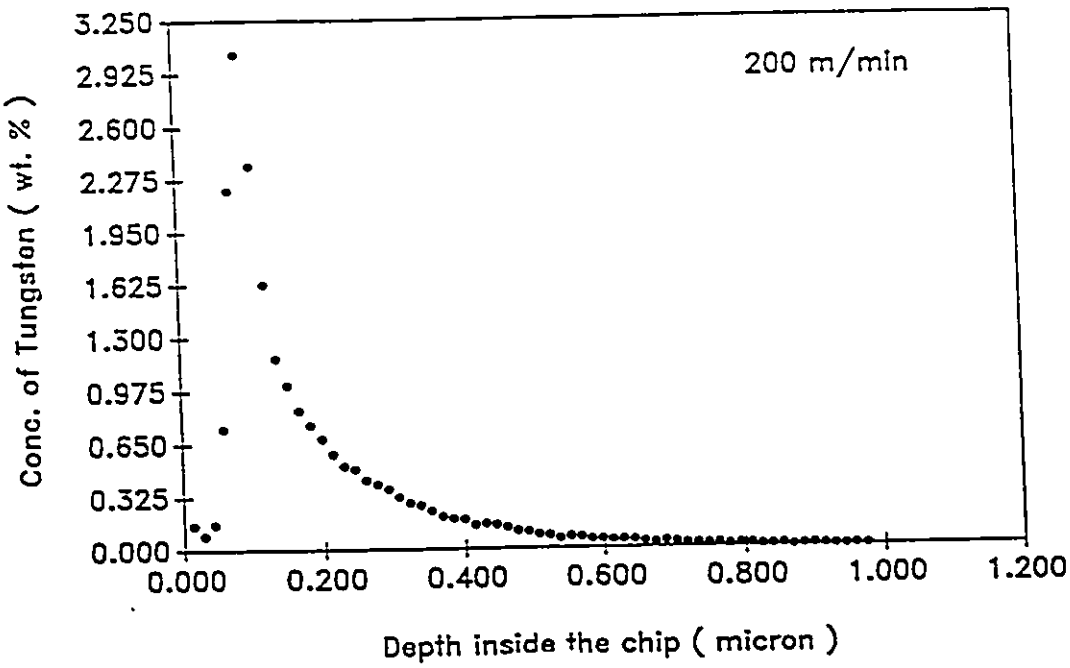

(a)

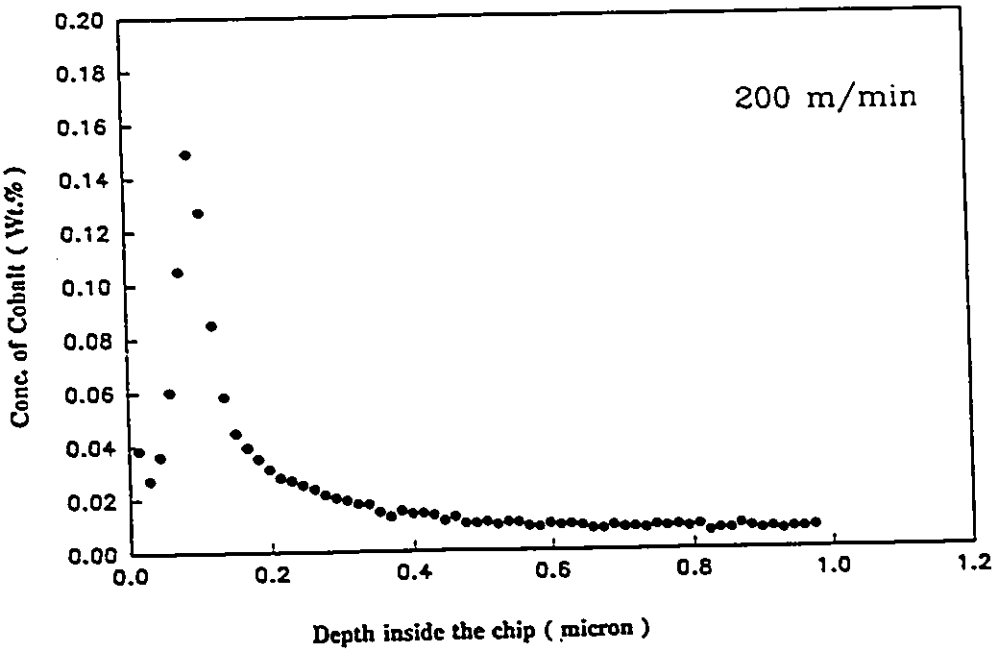

(b)

Fig.4.10 The concentration profiles of (a) tungsten and (b) cobalt in a quenched Steel 1 chip produced by a K-11 grade tool at 200 m/min.

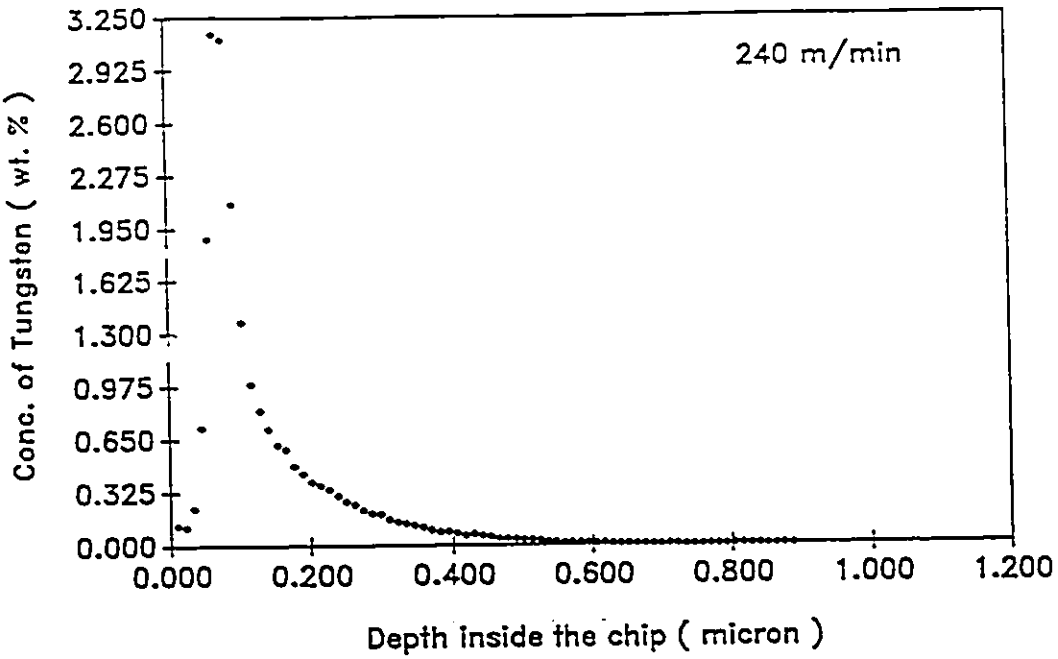

(a)

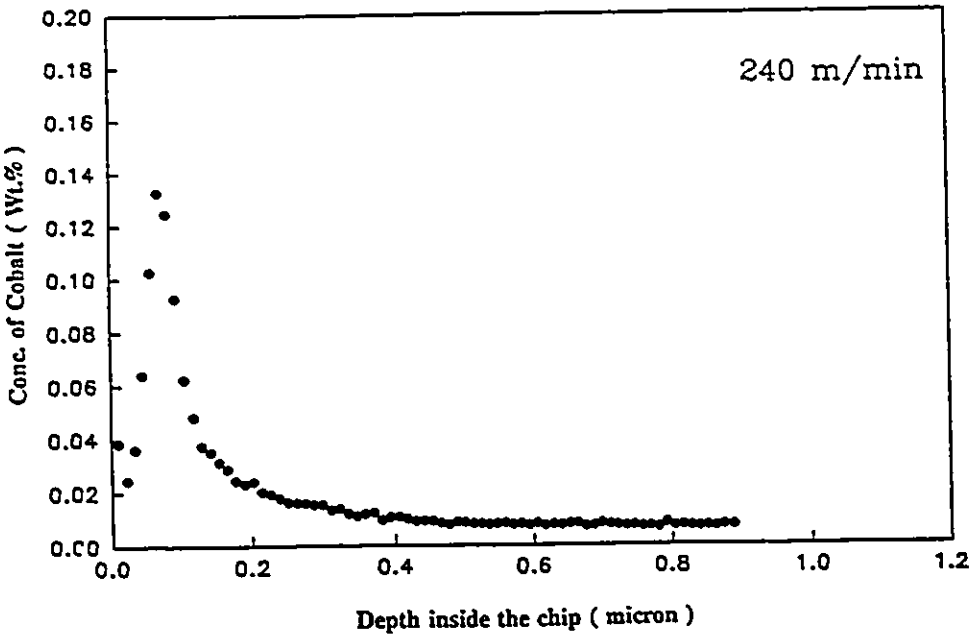

(b)

Fig.4.11 The concentration profiles of (a) tungsten and (b) cobalt in a quenched Steel 1 chip produced by a K-11 grade tool at 240 m/min.

chip. This interesting observation is analyzed further in Chapter 6.

Similar concentration profiles of tungsten were observed near the tool-chip interface of quenched austenitic stainless steel (AISI 316L) chips produced using the same tool as before. Fig.4.12(a) and (b) show these concentration profiles in chips produced at the cutting speeds of 150 and 200 m/min respectively. As before, the maximum concentration of tungsten in the chips is seen to increase with in increase in cutting speed. In the case of austenitic stainless steel chips, however, there is no drop in tungsten concentration very close to the tool chip interface. A comparison of concentration profiles in the two materials shows that at a given cutting speed,the depth of penetration of tungsten in medium carbon steel chips and in austenitic stainless steel chips is of the same order.

4-G : Microstructural Features of Secondary Shear Zone

The secondary shear zone undergoes extreme plastic deformation at strain rates in excess of 10^4per second at the higher speed machining used in this investigation. Since, diffusional mass transport also takes place in the secondary shear zone, its microstructural features must be characterized. Both Scanning Electron Microscopy (SEM) and Transmission Electron Microscopy (TEM) were employed for this purpose. The important role played by the microstructure of

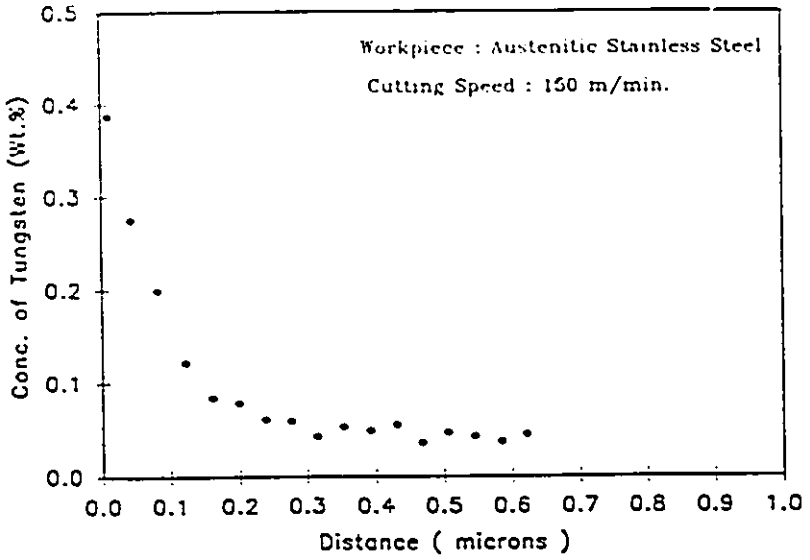

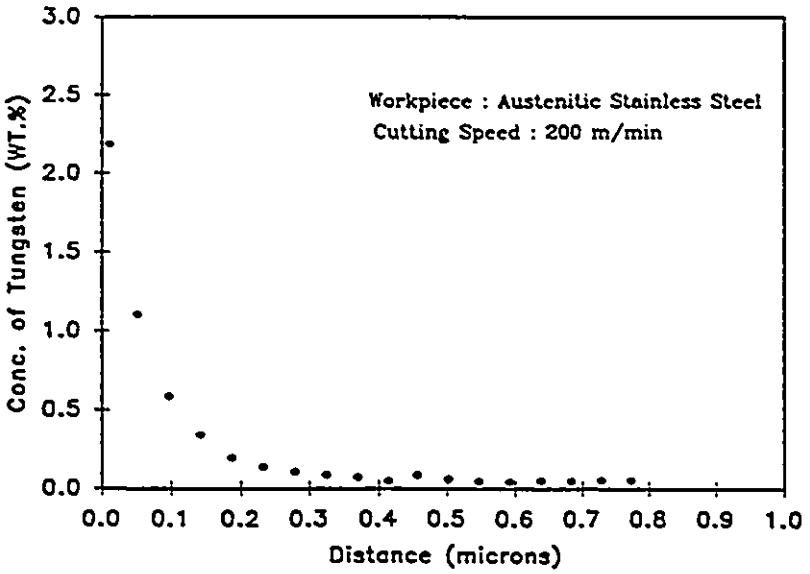

Fig.4.12 The concentration profiles of tungsten in the quenched austenitic stainless steel chips, produced by the K-11 tools at (a) 150 m/min and (b) 200 m/min.

secondary shear zone in influencing the diffusional process is discussed in Chapters 5 and 6.

Fig.4.13 (a) shows an SEM picture of the cross section of a chip taken in a plane perpendicular to its bottom surface. It can be observed that the structure in the region very close to the tool-chip interface is very fine and is difficult to resolve at a magnification of 885X. However, the severity of plastic deformation is clearly seen from the deformed and bent cementite plates seen in the secondary shear zone next to the zone of unresolved structure.

Fig.4.13 (b) shows the structure of secondary shear zone very close to the tool-chip interface. It can be observed from the micrograph that this region does not contain any cementite plates. A fine cell structure is seen with a cell size of the order of 0.2 to 0.5 micron. This lack of cementite plates was found in all the regions very close to the tool-chip interface, and indicates that a process of austenitization took place in this region.

Fig.4.13(c) is a TEM micrograph showing the structure of secondary shear zone in the region very close to the tool-chip interface. The TEM sample was prepared using the method of back polishing, as described in Chapter 3. Absence of pearlite is observed, which is in agreement with the SEM observations. Large twinned martensite areas can be seen in the micrograph. The chip was produced by

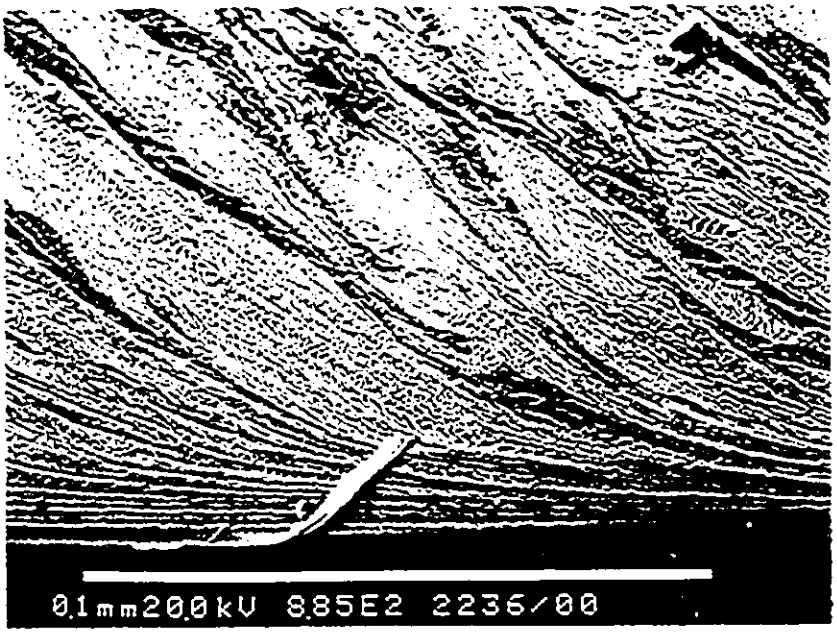

Fig.4.13(a) The cross section of a quenched chip produced by machining Steel 1 with a K-11 grade tool at 240 m/min.

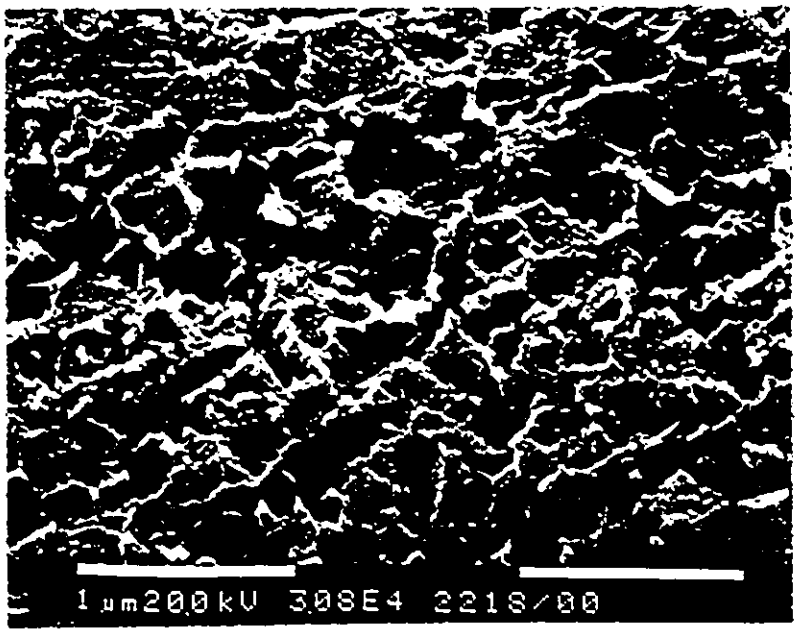

Fig.4.13(b) The ultrafine grains observed very close the tool-chip interface.

Fig.4.13(c) Twinned martensite observed inside the ultrafine grains of the water quenched chip.

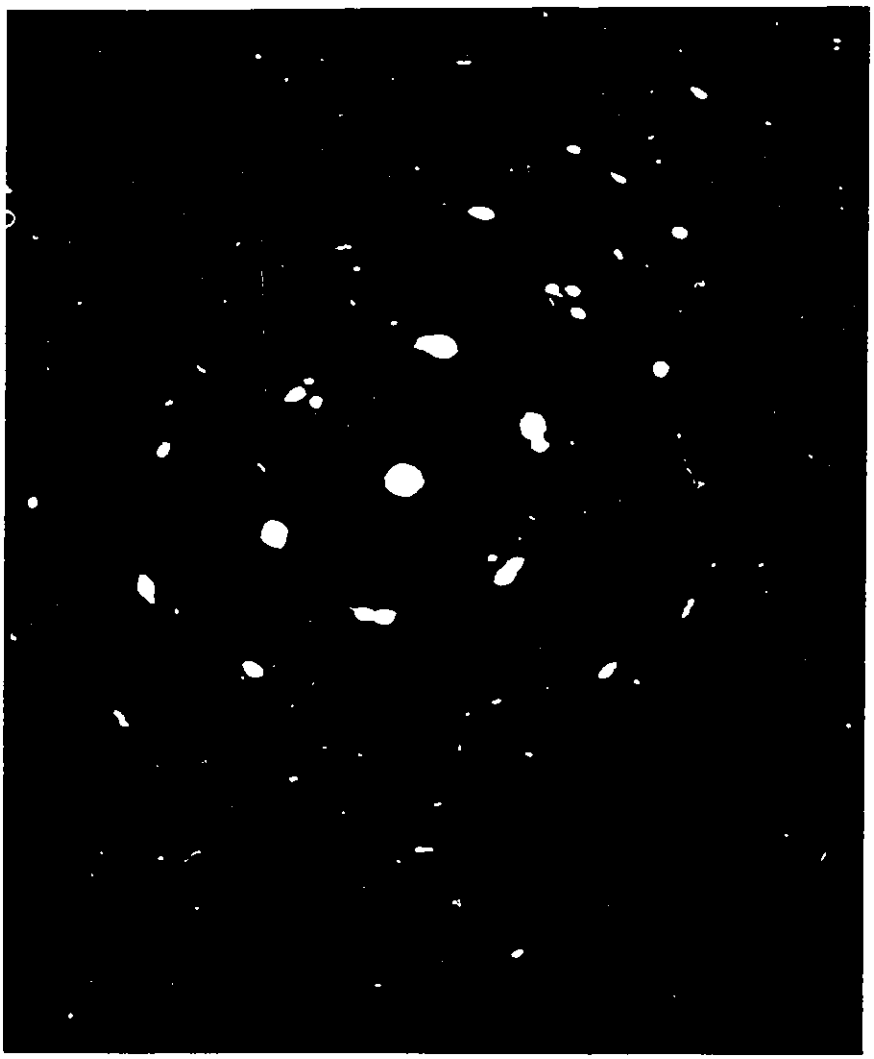

Fig.4.13(d) A selected area diffraction pattern obtained from the twinned region of the quenched chip, indicating it to be martensite.

machining AISI 1045 grade steel at 240 m/min and was quenched in water. Fig.4.13(d) is a selected area diffraction pattern taken from the twinned region and confirms that the twinned regions are martensitic. The twinned regions account for most of the area of the micrograph.

4-H : Effect of Dissolution Potential on Crater Wear

Experiments were designed to study the effect of a lower dissolution potential of the tool material (i.e. a lowered solubility in the chip material) on dissolution wear in a quantitative manner. This was achieved by :

A) Coating the tools with a 10 micron thick layer of hafnium nitride. This was achieved using a CVD process carried out at Teledyne Cutting Tools Inc., USA.

B) Using tool material alloyed with Ta(Nb)C which has a lower solubility than that of tungsten carbide in steel.

4-H.1 : Experiments with HfN Coated Tools

A 10 micron thick layer of hafnium nitride was deposited using a Chemical Vapor Deposition technique on K-11 tool (97 % WC) substrates. Wear tests were carried out at the cutting speeds of 220 and 240 m/min using the same Ca-treated AISI 1045 grade steel workpiece which was used in the previous wear tests. The duration of wear tests was 30

seconds as before. Chips were collected during each cut for quantification of tool wear using INAA.

Tool-chip contact lengths were measured after various cutting times. As can be seen from Fig.4.14, the tool-chip contact length remains the same over a period of 30 seconds. This is in sharp contrast to the behaviour observed during wear tests using uncoated K-11 tools where the tool-chip contact length increased very rapidly at the same cutting speed (See Fig.4.5).

Fig.4.15 shows the forces exerted on the coated tool during a 30 second wear test. It can again be observed that all three forces, viz. cutting, feed and radial forces, remain virtually constant during the wear test. This constancy of the forces is clearly related to the constancy of tool-chip contact lengths (and hence the constancy of tool-chip contact areas) during the wear test.

Using the data on forces and contact lengths, the average tool-chip interface temperatures were calculated. These average temperatures at the coated tool- chip interface were calculated using the procedure outlined in Appendix I. Fig.4.16 shows the temperatures reached at the interface of coated tool and and the chip. Temperatures reached at the interface of uncoated tool and the chip (reported previously) are also included for comparison. It can be seen that the temperatures existing at the interface of a coated tool and the chip remain virtually constant

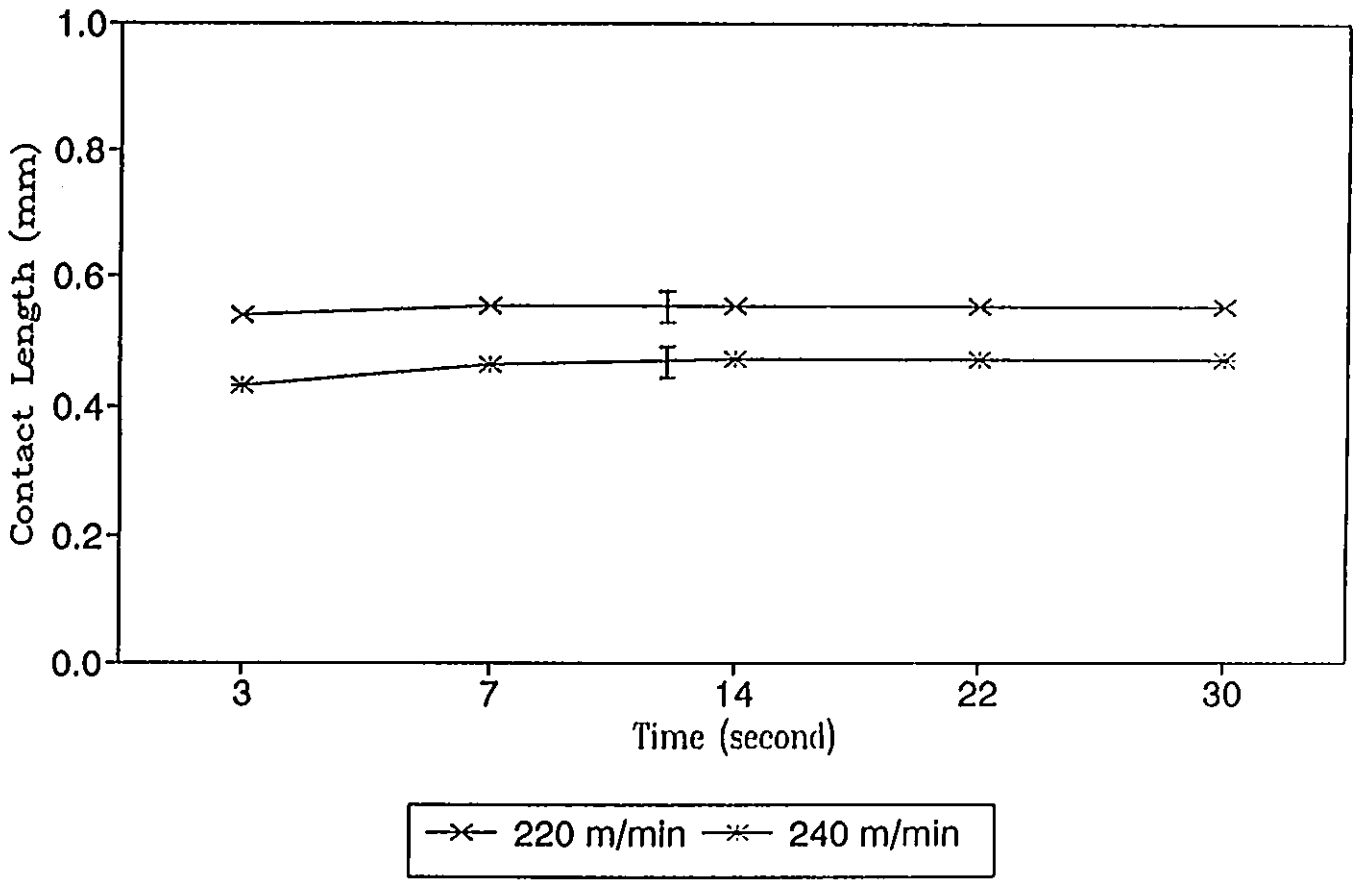

Fig.4.14 The variation of tool-chip contact lengths during wear tests using the HfN coated tools and the Steel 1 workpiece.

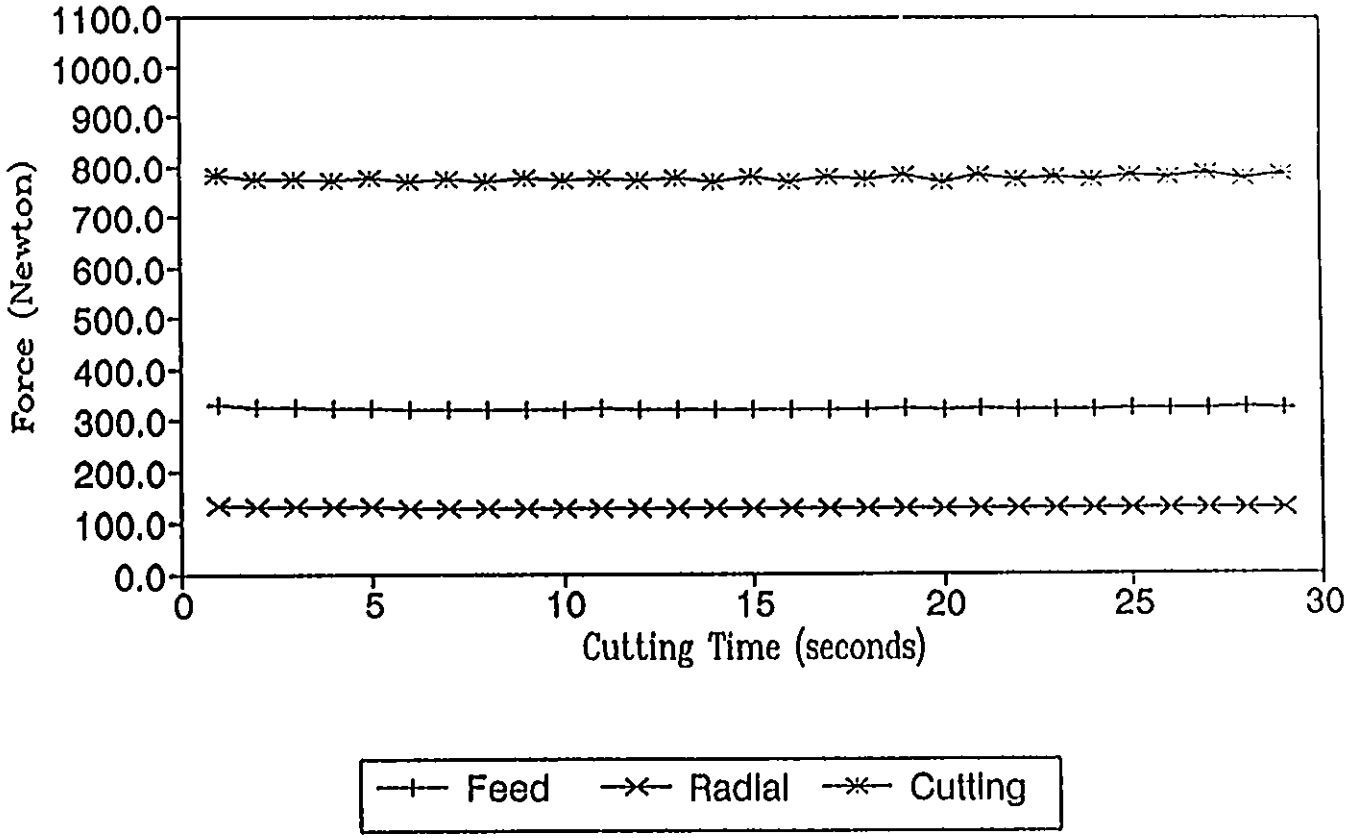

Fig.4.15 The variation of experimentally measured forces while machining Steel 1 with a HfN coated tool at 240 m/min.

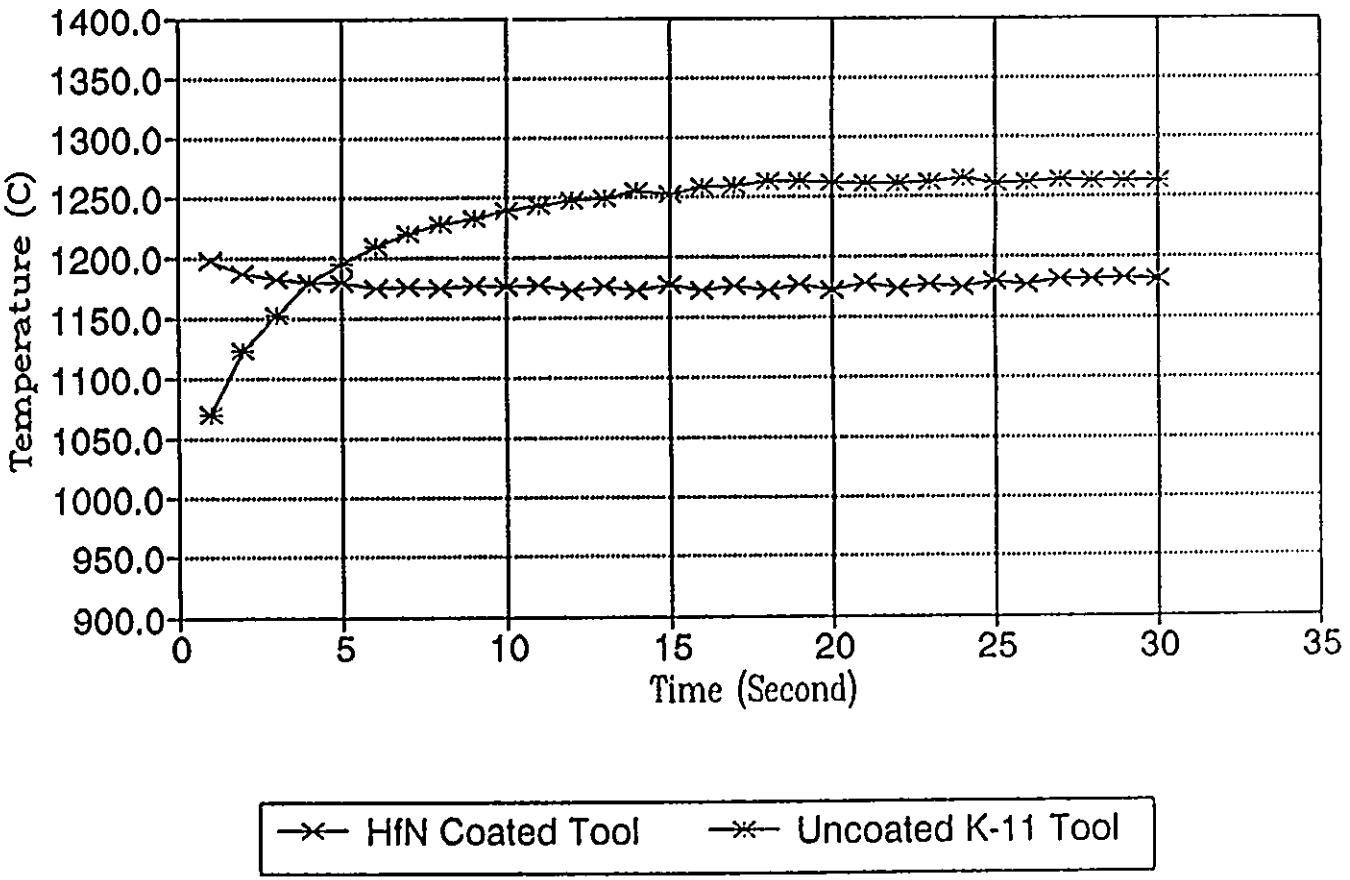

Fig.4.16 Comparison between the average interface temperatures developed using HfN coated and uncoated tools while machining Steel 1 at 240 m/min.

during the 30 second wear test. In contrast, the temperatures existing at the interface of an uncoated tool and the chip increase rapidly in the beginning and then tend to become constant. It can also be observed that the temperatures with a coated tool are lower than the saturation temperatures obtained using an uncoated tool by about 70° C.

Tool wear incurred during the wear tests using HfN coated tools at two cutting speeds was quantified using INAA. The chips were analyzed for the determination of tungsten and hafnium concentrations in the machining chips. However, at both the cutting speeds no increase in the tungsten or hafnium concentrations over and above that already present in the workpiece could be detected. It may be recalled that the concentrations of tungsten and hafnium in the workpiece, determined by taking the average of 14 samples of workpiece material, are equal to 11 ± 0.5 ppm and < 0.7 ppm respectively. The results obtained in the INAA of chips are summarized below :

Cutting Speed (m/min)	Conc. of tungsten in the chips (ppm)	Conc. of hafnium in the chips (ppm)
220	11.3 ± 0.1	< 0.7 ppm
240	11.2 ± 0.1	< 0.7 ppm

It may be recalled that in the case of wear tests using an uncoated tool, the average tungsten concentration of chips increased to 22.2 ppm, an increase of 11.2 ppm over the tungsten concentration in the workpiece. However, with a coated tool having a much lowered dissolution potential in the chips, the increase in hafnium concentration in the chips was so small that it was indistinguishable from the original signal from the workpiece material. The fact that there was no increase in the tungsten content of the chips produced using a HfN coated tool shows that the coating remained intact during machining and the substrate material underneath the coating did not come in contact with the chips.

4-H.2 : Experiments With Alloyed Tools

K-1 grade tools (4 % Ta(Nb)C, 85 % WC, 11% Co) were used in wear tests keeping the workpiece material and the cutting conditions the same as those used in the previous series of experiments performed using K-11 grade tools.(97 % WC). Crater wear was quantified using the technique of INAA. Total crater wear was again separated into mechanical wear and dissolution wear components and the results are summarized in Fig.4.17 where Fig.4.2(b) is also reproduced for the sake of comparison. A comparison between the two clearly shows that the crater wear rate with the alloyed tool material is almost half of the value obtained using the

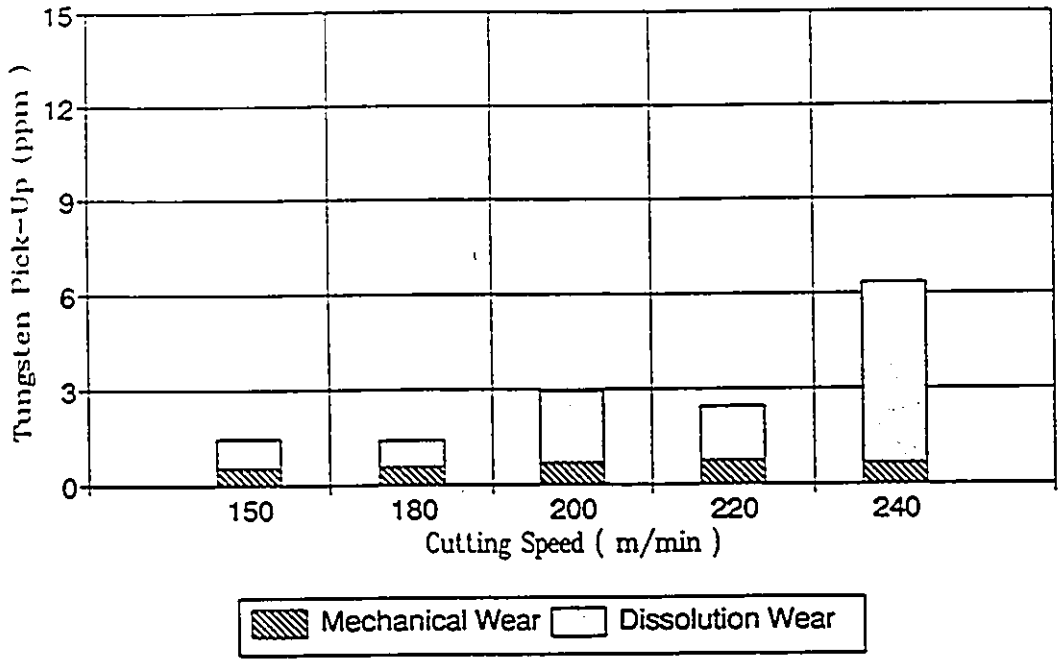

(a) K-1 grade tools

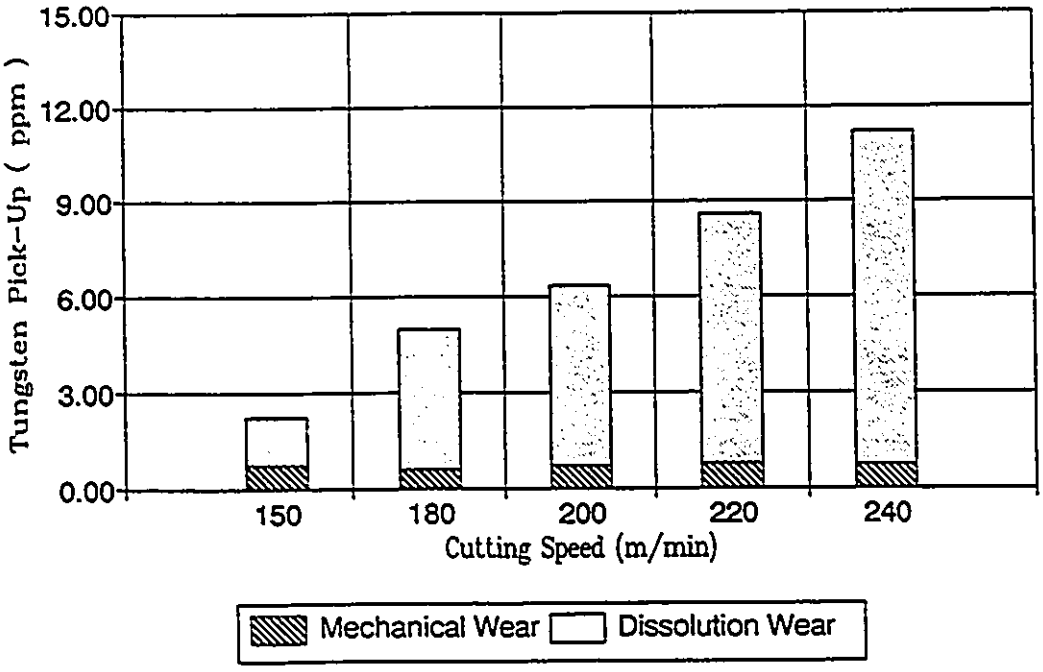

(b) K-11 grade tools

Fig.4.17 Crater wear rates of cutting tools while machining Steel 1.(expressed as tungsten pick-up)

straight tungsten carbide grade of tool. The normalized mechanical wear rate in the two cases remains the same, but the normalized dissolution wear rate has been lowered in the case of the alloyed tool material. This clearly shows that the better performance shown by the alloyed tool is due to lowered dissolution wear rates achieved by monitoring the dissolution potential of the tool constituents. This quantitative comparison between the performances of the two grades of tools demonstrates the usefulness of the INAA technique.

4-I : Inclusions and the Mechanical Wear of Tools

It has been shown previously that a change in the cutting speed (and hence the temperature) has a negligible effect on the normalized mechanical wear rates during metal cutting. In this section the effect of the presence of hard alumina inclusions in the workpiece on normalized mechanical wear rate is reported in a quantitative manner.

Wear tests were carried out using an AISI 1045 grade steel workpiece produced without calcium treatment during its balanced deoxidation procedure, i.e. Si-killed, Al-grain refined during deoxidation. The workpiece, therefore, contained some amount of hard alumina inclusions. Chemical compositions and the details about the inclusions present in the workpiece are given in the 'Materials Characterization' section of Chapter 3 where a typical alumina inclusion

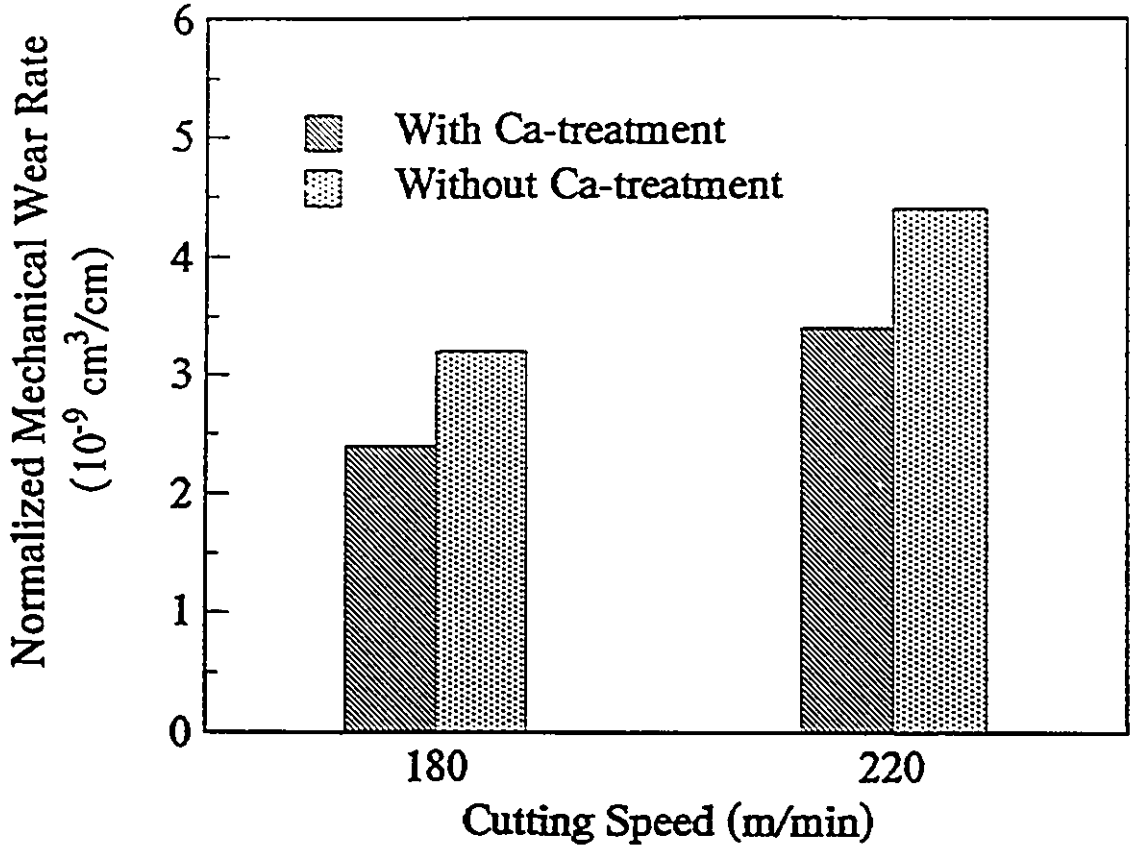

Fig.4.18 Comparison between the normalized mechanical wear rates while machining the AISI 1045 steels, produced with and without calcium treatment, by using the K-11 grade tools.

observed in this steel is shown. K-11 grade tools (97 % WC) were used to carry out the wear tests at 180 and 220 m/min. Normalized mechanical wear rates were calculated using the method described previously and are shown in Fig.4.18. For comparison, the normalized mechanical wear rates obtained during the previous series of experiments using Ca-treated AISI 1045 grade steel workpiece are also included. A comparison between the normalized mechanical wear rates obtained with the two steels at a given cutting speed shows that the normalized mechanical wear rates are about 33 % higher for the workpiece containing hard alumina inclusions.

The difference between the values of normalized mechanical rates of the tool resulting from the two steels under given cutting conditions will depend on the volume fraction of hard inclusions in the steel produced without Ca-treatment. Comments on the role of inclusions present in the calcium treated steel in reducing the crater wear of cutting tools are also included in Chapter 6.

Chapter 5 : A Quantitative Model for Dissolution Wear

The strong influence of temperature on crater wear rates and a positive correlation between the crater wear rate and the solubility of the tool material in the workpiece have led to a diffusional hypothesis for crater wear of cutting tools, Loladze [44] and Trent [71] being its chief proponents in the early 1960s. A model for crater wear based on this diffusional hypothesis was developed by Bhattacharyya, which took the non-static diffusional contact between the tool and the chip into account[45]. This model is described here in detail, followed by the refinements which are deemed necessary in light of the processes occurring at the tool-chip interface in the secondary shear zone. The refined thermokinetic model is then used to estimate dissolution wear. The results of the model are compared with the experimental results.

5-A : Bhattacharyya's Model of Diffusional Wear

Consider an element of chip moving over the rake face of the tool as shown in Fig.5.1. This element of chip is considered to be in intimate contact with the tool for a time equal to the tool-chip contact time, τ. This element of

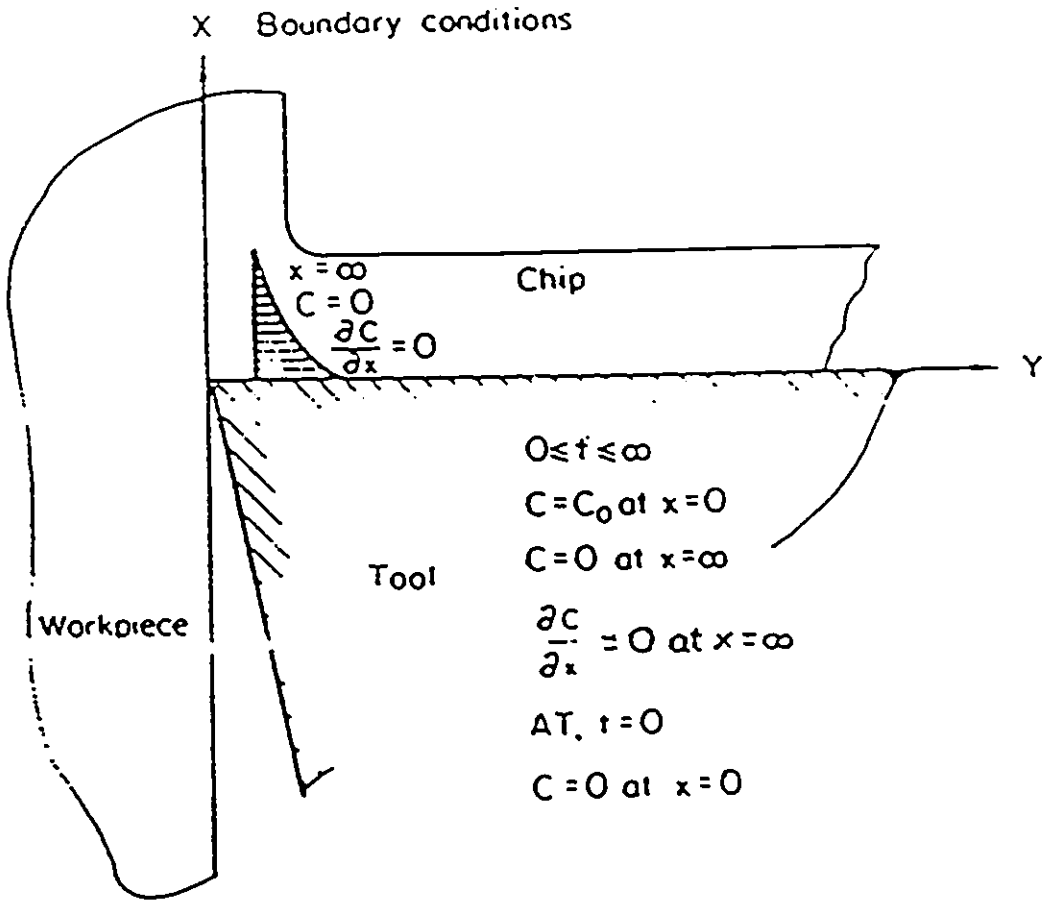

Fig.5.1 The boundary conditions at the tool-chip interface during metal cutting. (The diffusion zone is highly exaggerated)

the chip and the tool constitute a diffusion couple and diffusional mass transport is considered to take place for time τ, after which the element loses contact with the tool. This non-static nature of contact between the two components of diffusion couple was recognized by Bhattacharyya and duly incorporated into the model. The unit diffusional process lasting for a time equal to the tool-chip contact time is considered to repeat over and over till the end of the cutting operation. Thus, the amount diffused during the cutting time t could be taken to be equal to (t/τ) times the amount diffused during the tool-chip contact time, τ. The amount of diffusional transport from the tool into the element of chip in time τ was obtained by making the following assumptions :

1) The tool-chip contact is very intimate. Thus, the apparent contact area is equal to the true contact area.
2) Local equilibrium is reached at the tool-chip interface, which determines the concentration of tungsten at the interface.
3) Diffusion is one dimensional and takes place in a direction normal to the tool-chip contact area.
4) The effect of plastic deformation taking place at the tool-chip interface (secondary shear zone) on the diffusion coefficients can be neglected.
5) The tool-chip contact length, chip velocity and interface

temperatures do not vary with cutting time t.

Equilibrium concentration of tungsten is, thus reached at the tool-chip interface while machining with a tungsten carbide tool. When the solute is transported away from the interface a concentration profile is produced. The diffusion process under the given conditions is described by Fick's Second law:

$$\frac{\partial C}{\partial t} = D \cdot \left(\frac{\partial^2 C}{\partial x^2} \right) \qquad (5.1)$$

where, C is the concentration of tungsten,

D is the diffusivity of tungsten,

x is the distance from the interface, and

t is the time.

The boundary conditions for this problem are as follows :

$$\left.\begin{array}{ll} \text{At } t = 0 & C = 0 \text{ at } x = 0 \\ \text{At } 0 < t < \infty & C = C_o \text{ at } x = 0 \\ & C = 0 \text{ at } x = \infty \end{array}\right\} \qquad (5.2)$$

$$\partial C/\partial x = 0 \text{ at } x = \infty$$

Solution of the above differential equation with the applicable boundary conditions is :

$$C = C_o \cdot \left[1 - \mathrm{erf}\left(x/2\sqrt{(D.t)} \right) \right] \qquad (5.3)$$

The amount of tungsten dissolved per unit area in the tool-chip contact time, τ, is given by the area under the concentration distance curve.

$$\text{Area under the curve} = \int_0^\infty C \cdot dx \qquad (5.4)$$

$$\text{Area} = \int_0^\infty C_o \cdot \left[1 - \mathrm{erf}\left(x/2\sqrt{(D.t)} \right) \right] dx \qquad (5.5)$$

$$\text{Flux in time } \tau = 1.1284 \cdot C_o \cdot \sqrt{(D.\tau)} \qquad (5.6)$$

$$\text{Flux in total time } t = 1.1284 \cdot C_o \cdot \sqrt{(D.\tau)} \cdot \left(t/\tau \right) \qquad (5.7)$$

The total amount of tungsten dissolved, W, is given by :

$$W = 1.1284 \cdot C_o \cdot t \cdot \sqrt{(D/\tau)} \cdot (\text{Contact Area}) \qquad (5.8)$$

The interfacial concentration C_o used in this model was obtained from the Fe-W phase diagram as the solubility limit of tungsten in iron at the temperature of interest.

5-B : Refinements to the Bhattacharyya Model

The accuracy of a model depends on how realistic the boundary conditions are and how valid the assumptions are. Results on the microstructural features of the secondary

shear zone and the study of the behaviour of important metal-cutting parameters such as contact lengths, contact areas, forces and temperatures during wear tests were presented in Chapter 4. In light of these results, the boundary conditions used to solve the diffusion equation and the assumptions made in the basic formulation of the model are re-examined.

5-B.1 : Determination of Interfacial Concentration

The equilibrium concentration of tungsten at the tool-chip interface during metal cutting with a tungsten carbide tool was obtained from the Fe-W phase diagram in the Bhattacharyya model. However, in reality, the cutting tool is not made of tungsten but of tungsten carbide. Thus, tungsten and carbon together go into solution in the chip material at the interface. Therefore, the interfacial concentration of tungsten should be calculated from the solubility product of tungsten carbide in the phase of the chip material which exists at the tool-chip interface during cutting. The chip acts as a sink for tungsten and carbon.

The workpiece material used in the present investigation was an AISI 1045 grade steel with a ferrite + pearlite microstructure. However, the secondary shear zone of water quenched chips produced at a cutting speed of 240 m/min showed no cementite plates in the immediate vicinity of the tool-chip interface . TEM analysis of this region

showed large areas of twinned martensite produced as a result of quenching. These results indicate that the process of austenitization of the chip material next to the tool-chip interface indeed took place during the tool-chip contact time. It is pertinent to note here that very severe plastic deformation processes take place in the immediate vicinity of the tool-chip interface. The chip material undergoes plastic strains of the order of 150 at strain rates of the order of 25000 s^{-1} during a typical high speed machining operation. It is also known that the rates of austenitization, as a consequence of severe deformation, show an order of magnitude increase. Thus, a distinct possibility exists that a small region about 10 micron thick next to the tool-chip interface would austenitize during the tool-chip contact time. Consequently, the solubility product of tungsten carbide in austenite should be used to calculate the interfacial concentration of tungsten. This value, however, will depend on the degree of austenitization in the region close to the interface during the tool-chip contact time of about half a millisecond. Two extremes cases of austenitization are considered and the interfacial concentrations of tungsten are calculated for each of the two cases. As mentioned before, the workpiece material used for this analysis was AISI 1045 grade steel (0.45 wt % C).

Case I : Complete Dissolution of Cementite

Consider the situation where all the cementite present in a small region, extending about 5-10 microns into the chip from the tool-chip interface, dissolves completely. The austenitic phase which is formed, therefore, contains 0.45 wt.% carbon which is equivalent to 2.06 % on a mole percent scale. Tungsten carbide goes into solution in this austenite and the process can be written as follows :

$$WC \rightarrow \underline{W} + \underline{C} \tag{5.9}$$

Urhenius *et al.*[72] have studied the Fe-W-C equilibrium and have reported the γ-WC solvus curve at different temperatures. The following equation for the solubility product of tungsten carbide in austenite was fitted to their results :

$$\log\Big((\text{at.\% W})\cdot(\text{at.\% C})\Big) = 5.319 - 6404.3/T \tag{5.10}$$

For each tungsten atom going into solution in austenite, there is one carbon atom from tungsten carbide going into solution with it.

$$\text{at.\% C in } \gamma \text{ phase} = \text{at.\% W in } \gamma \text{ phase} + 2.06 \tag{5.11}$$

$$\therefore (\text{at.\% W})\cdot(\text{at.\% W} + 2.06) = \text{Solubility Product} \tag{5.12}$$

By solving this quadratic equation, the interfacial concentration of tungsten is obtained as a function of temperature, Fig.5.2. To facilitate a comparison between the

observed interfacial concentration of tungsten (SIMS results) and the predicted interfacial concentration before solute redistribution, the concentration of tungsten has been expressed as Wt.% in Fig.5.2.

Case II : No Dissolution of Cementite

Consider a situation in which the ferrite in chips undergoes a change in crystal structure from bcc to fcc. However, due to insufficient time, no cementite dissolves. Thus, the microstructure of the chip just next to the tool-chip interface consists of a mixture of austenite having the same amount of carbon as ferrite (almost zero) and cementite.

Two processes will take place simultaneously during the tcol-chip contact period.

1) Cementite will reject carbon into carbon free austenite and will try to dissolve, as it is thermodynamically unstable at this temperature.

2) Tungsten carbide from the tool will dissolve in austenite at the tool-chip interface. This can be written as :

$$WC \Rightarrow \underline{W} + \underline{C}$$

Thus, carbon is being pumped into austenite from two independent sources (cementite and tungsten carbide). To calculate the concentration of tungsten at the interface using the solubility product data, the rate at which carbon

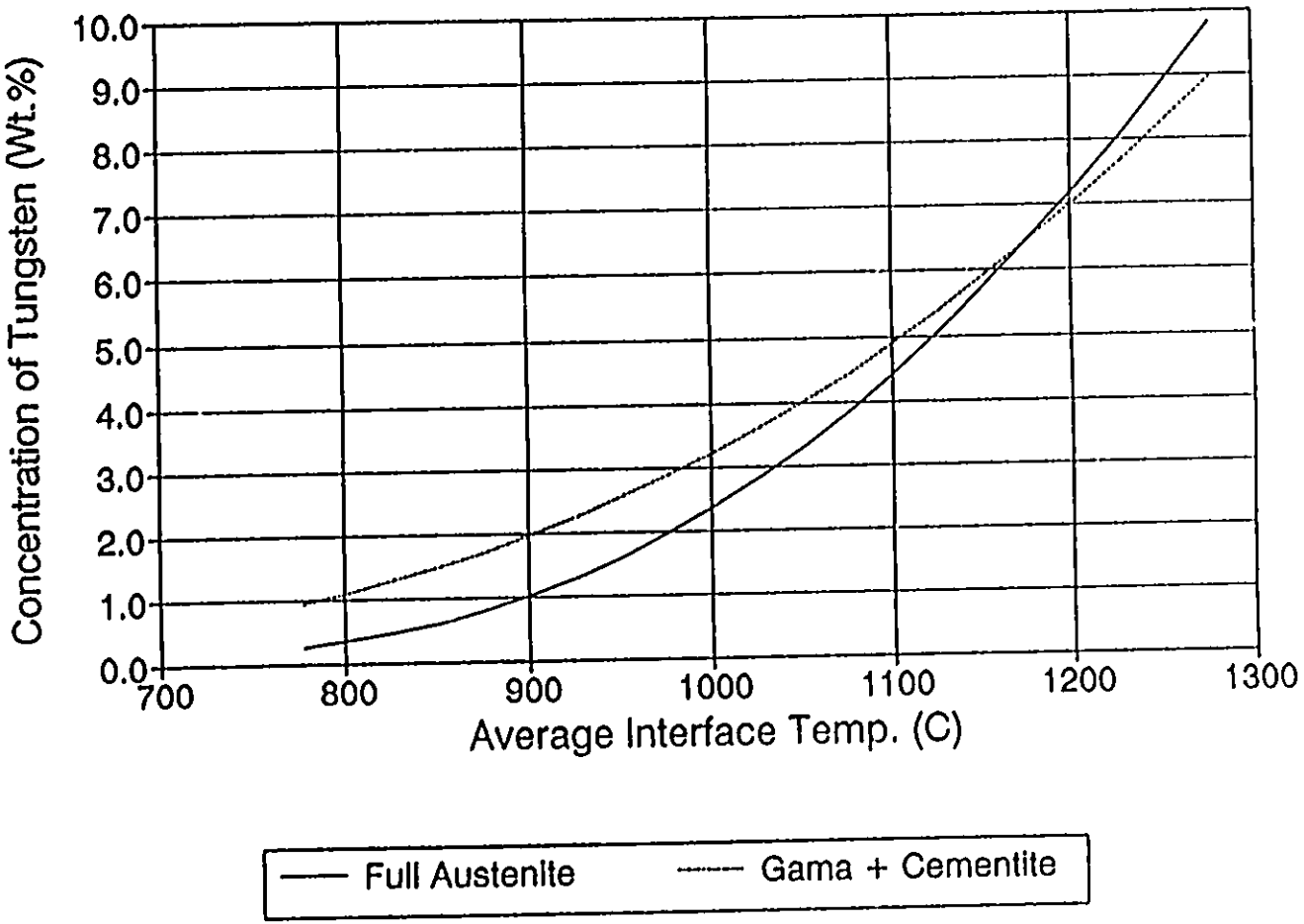

Fig.5.2 The equilibrium tungsten concentrations at the tool-chip interface.

is added to austenite from these two independent sources must be known. As a first approximation these two rates can be assumed to be equal. Again, for every carbon atom from tungsten carbide there is one tungsten atom going into solution with it. Therefore, we can write :

$$\text{Total at.\% carbon in } \gamma = 2 \times (\text{at.\% tungsten in } \gamma) \quad (5.13)$$

$$\text{Solubility Product of WC in } \gamma = 2 \times (\text{at.\% tungsten})^2 \quad (5.14)$$

Thus, the concentration of tungsten at the tool-chip interface can be obtained as a function of temperature for this possible scenario, and is shown in Fig.5.2.

5-B.2 : Consideration of Pearlite - Effective Machining Time

In Case II, it is the carbon free austenite formed from ferrite, which is considered to act as a sink for tungsten. However, in the AISI 1045 grade steel, ferrite is present in two forms :

1) Proeutectoid ferrite (volume fraction 44%)
2) Ferrite as a part of pearlite (volume fraction 49.3%)

Since cementite plates, which can block tungsten diffusion, are postulated to be present in the chip material, an important question to consider is how much of the pearlitic ferrite can serve as a sink for tungsten. Two possibilities are considered again :

Situation A : It is assumed here that only the proeutectoid

portion of ferrite can serve as a sink for tungsten diffusion (after transforming to austenite), whereas diffusion into the pearlitic ferrite would be completely blocked by the cementite plates. Volume fraction of proeutectoid ferrite in the chip is equal to 44%. Thus, according to the assumption made here only 44% of the chip material can serve as a sink for tungsten diffusion. In other words, the effective machining time is only 44% of the actual machining time of 30 seconds.

Situation B : It is assumed here that in addition to proeutectoid ferrite, pearlitic ferrite would also serve as a sink for tungsten. The volume fraction of sink in this situation can be calculated as follows :

Volume fraction of proeutectoid ferrite in chips = 44 %

Volume fraction of pearlite in chips = 56 %

Percentage of ferrite in pearlite = 88 %

Percentage of cementite in pearlite = 12 %

Volume fraction of pearlitic ferrite in chips = 49.3 %

Vol. fraction of chip serving as sink = 93.3 %

The effective machining time is obtained using the following equation:

$$\text{Effective machining time} = \phi \times \text{Actual machining time} \quad (5.15)$$

where, ϕ is the volume fraction of the chip material serving as the sink for tungsten diffusion.

Thus, the effective machining time for situation B is 93.3% of the actual machining time of 30 seconds.

5-B.3 : Influence of Plastic Deformation on Diffusivity

The effect of plastic deformation taking place in the secondary shear zone on the diffusivity of tungsten was neglected in Bhattacharyya's model. However, depending on the severity of plastic deformation and the temperature at which deformation took place, the effect on diffusivity can be significant. The factor by which the diffusivity of tungsten is enhanced can be estimated with the help of the microstructural information of the region presented in Chapter 4. [Fig.4.13]

The region of interest in the secondary shear zone of the chips (where the diffusion zone lies) showed an ultrafine grain size. The diameter of these grains, as seen under the SEM, was 0.2-0.5 microns. Such fine equiaxed grains are indeed observed as a result of adiabatic plastic deformation processes in general.[12] The severe plastic stains incurred at high temperatures, approximately equal to 0.75 T_m in this case, leads rapid recrystallization of the material next to the tool-chip interface, thereby forming the equiaxed grains.

Grain boundaries provide fast diffusion paths, and the effective diffusivity of the chip material next to the tool chip interface is enhanced. The extent of this

enhancement depends on the fraction of grain boundary area available for diffusion, which in turn depends on the grain size. The effective diffusivity in the material is given by the following well-known expression :

$$D_{eff} = f.D_{gb} + (1-f)\ D_{lattice} \qquad (5.16)$$

where, f is the fraction of grain boundary area.

The lattice diffusion coefficient of tungsten in austenite [73] and the diffusion coefficient of tungsten along the grain boundaries of alloy steel, as derived from the results of Zemskiy *et al.* [74] by Kaur and Gust [75] are shown in Fig.5.3. The effective diffusion coefficients have been calculated for three grain sizes : 0.5 micron (f= 0.0024), 0.2 micron (f=0.006) and 0.1 micron (f=0.012) and are shown in Fig.5.3. A grain boundary width of 0.3 nm has been assumed in the calculations of grain boundary area fraction. It can be seen that due to the formation of ultrafine grains, which resulted from severe high temperature plastic deformation, the effective diffusivity in the material is enhanced by an order of magnitude in the temperature regime of interest. Thus, the deformation processes taking place in the secondary shear zone are directly responsible for the increase in dissolution wear rates through diffusion enhancement.

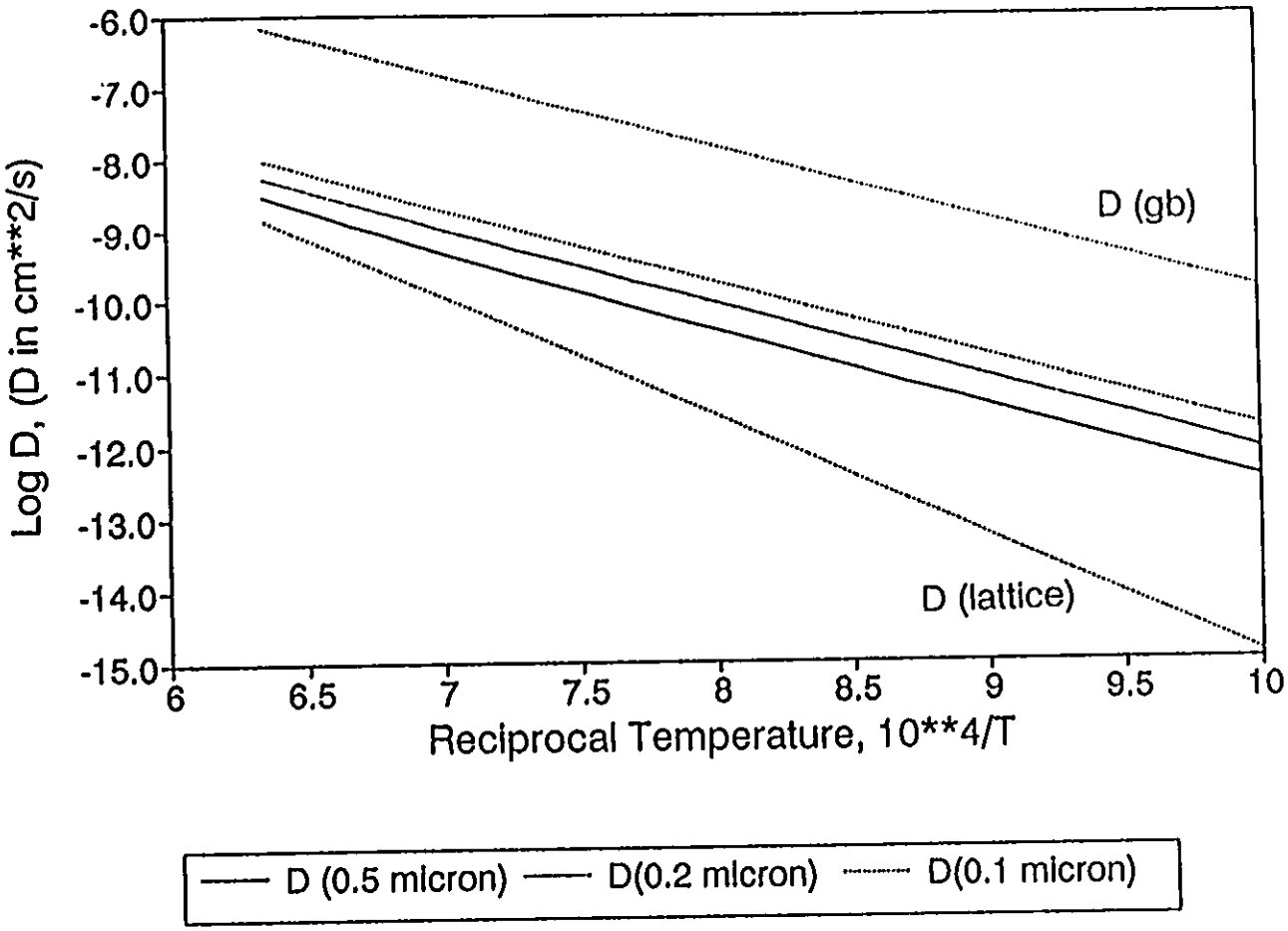

Fig.5.3 The effective tungsten diffusivities at various grain sizes of the chip material.

5-B.4 : Numerical Calculations of Dissolution Wear

Metal cutting parameters, such as tool-chip contact length, contact area, chip velocity and temperature were assumed to be constant throughout the cutting test in Bhattacharyya's model. The validity of this assumption depends on the specific tool workpiece combination. From the results presented in Chapter 4, it can be seen that for a K-11 tool (97 % WC) - AISI 1045 steel workpiece combination, the contact lengths, contact areas and the interface temperatures increased with time during the 30 second wear test. However, when the tool was coated with hafnium nitride all the metal cutting parameters remained virtually constant during the 30 second wear test.

In this investigation, a dissolution wear database has been established using a K-11 tool (97% WC) for which the above assumption is not valid. As a result, in order to use the refined thermokinetic model, instantaneous values of all the variables involved in the model must be used to obtain instantaneous amounts of dissolution wear. Total dissolution wear in time t is then obtained by summation.

The instant of time used in this analysis was chosen to be equal to 1 second. In other words, the contact lengths, contact areas and the average interface temperatures were obtained at each of the 30 seconds of machining time. These values can then be used in the model to obtain the amount of dissolution wear during each 1

Table 5.1

Variation of some metal cutting parameters during a 30 second wear test at 150 m/min using K-11 grade tool and a steel 1 workpiece.

Table 5.1

Cutting Time (s)	Contact Length (mm)	Contact Time (ms)	Contact Area (mm^2)	Average Temp. (K)
1	0.603	0.554	1.11	1251
2	0.613	0.563	1.13	1260
3	0.623	0.573	1.14	1270
4	0.634	0.583	1.16	1281
5	0.644	0.592	1.18	1294
6	0.654	0.602	1.20	1312
7	0.665	0.611	1.22	1313
8	0.675	0.621	1.24	1308
9	0.685	0.630	1.25	1319
10	0.696	0.639	1.27	1320
11	0.706	0.649	1.29	1317
12	0.716	0.658	1.31	1333
13	0.727	0.668	1.33	1327
14	0.737	0.678	1.34	1331
15	0.748	0.687	1.36	1338
16	0.758	0.697	1.38	1341
17	0.768	0.706	1.40	1354
18	0.779	0.716	1.41	1355
19	0.789	0.725	1.43	1353
20	0.799	0.735	1.45	1358
21	0.810	0.744	1.47	1360
22	0.820	0.754	1.49	1360
23	0.830	0.763	1.50	1367
24	0.841	0.773	1.52	1368
25	0.851	0.782	1.54	1368
26	0.861	0.792	1.56	1373
27	0.872	0.801	1.57	1370
28	0.882	0.811	1.59	1375
29	0.892	0.820	1.61	1378
30	0.903	0.830	1.63	1379

second interval. All such dissolution wear amounts can be numerically integrated to obtain the total amount of dissolution wear in a 30 second wear test. Table 5.1 shows one such set of instantaneous values during a 30 second wear test carried out at a cutting speed of 150 m/min.

Dissolution wear amounts can, thus, be expressed as the following sum :

$$W = \sum_{i=1}^{30} 1.1284 \cdot \phi \cdot C_{oi} \cdot A_i \cdot \sqrt{(D_i/\tau_i)} \qquad (5.17)$$

All the variables in the above equation have the same meaning as defined previously.

5-C : Comparison With Experimental Results

5-C.1 : Dissolution Wear

Using the procedure of numerical integration, dissolution wear was calculated according to the refined thermokinetic model discussed in the preceding sections. This was done for all the possibilities which were considered in the model. Table 5.2 shows the calculated dissolution wear for Case I. In Case I, the chip material next to the tool-chip interface was assumed to be fully austenitic with complete dissolution of cementite plates. The estimates of dissolution wear have been made for three grain sizes- 0.5 μm, 0.2 μm and 0.1 μm. The experimentally measured amounts of dissolution wear in each test are also

Table 5.2

Comparison between the dissolution wear predicted by model I (100% austenitization) and the experimentally determined amounts.

Cutting speed (m/min)	Estimated Dissolution wear (Thermokinetic model)			Experimentally measured amounts (10^{-6} gm)
	0.5 μm (10^{-6} gm)	0.2 μm (10^{-6} gm)	0.1 μm (10^{-6} gm)	
150	56.7	99.0	138	287±97
180	135	201	277	1088±124
200	244	356	488	1495±134
220	537	757	1026	2193±141
240	819	1139	1530	3283±158

Table 5.3
Comparison between the dissolution wear predicted by model II-a (44% effective machining time) and the experimentally determined amounts.

Cutting speed (m/min)	Estimated Dissolution wear (Thermokinetic model)			Experimentally measured amounts (10^{-6} gm)
	0.5 μm (10^{-6} gm)	0.2 μm (10^{-6} gm)	0.1 μm (10^{-6} gm)	
150	34	51.3	71	287±97
180	65	96	132	1088±124
200	110	160	219	1495±134
220	224	315	427	2193±141
240	331	461	619	3283±158

included in the same Table for comparison. It can be observed that the estimated dissolution wear amounts obtained using the model do show an increase with an increase in cutting speed. However, at each cutting speed, the estimated amount of dissolution wear using the model is lower than the experimentally measured amount.

Tables 5.3 and 5.4 show the estimated amounts of dissolution wear calculated for the two situations discussed in Case II. In Case II, the chip material next to the tool-chip interface was assumed to be a mixture of undissolved cementite plates and carbon free austenite formed from ferrite. The results obtained from a consideration of effective machining time of 44 % of the actual machining time of 30 seconds are given in Table 5.3. An effective machining time equal to 93.3 % of the actual machining time of 30 seconds leads to results presented in Table 5.4. Again, it can be seen that the estimated amounts of dissolution wear do increase with an increase in cutting speed in accordance with the experimental observations. However, the estimated amounts of dissolution wear are lower than the experimentally measured amounts using INAA. The predicted values of dissolution wear obtained by assuming no dissolution of cementite plates during the tool-chip contact are seen to be lower than those predicted by the model assuming complete dissolution of cementite. The real situation is very likely to be in between these two

Table 5.4

Comparison between the dissolution wear predicted by model II-b (93.3% effective machining time) and the experimentally determined amounts.

Cutting speed (m/min)	Estimated Dissolution wear (Thermokinetic model)			Experimentally measured amounts (10^{-6} gm)
	0.5 μm (10^{-6} gm)	0.2 μm (10^{-6} gm)	0.1 μm (10^{-6} gm)	
150	72	109	151	287±97
180	137	203	280	1088±124
200	232	339	466	1495±134
220	474	670	906	2193±141
240	703	977	1313	3283±158

Table 5.5
Comparison between the values of tungsten flux into the chip predicted by model I (100% austenitization) and the experimentally determined values.

Cutting speed (m/min)	Flux (Theoretical) (μg/cm^2)		Grain size considered in Model (μm)	Flux (observed) (μg/cm^2)
	t= 4th sec	t= 5th sec		
150	0.0874 0.0624 0.0405	0.105 0.0751 0.0489	0.1 0.2 0.5	0.201 ±0.007
240	0.64 0.468 0.324	0.772 0.566 0.395	0.1 0.2 0.5	2.02 ±0.05

extremes, but closer to the complete austenitization case, as suggested by large areas of twinned martensite observed in the microstructure of quenched chip.

5-C.2 : Instantaneous Diffusion Fluxes

The diffusion flux of tungsten (units :g/cm^2) into the chip has been calculated at two cutting speeds using the areas under the experimentally obtained concentration profiles using SIMS analysis. These areas were calculated by the procedure of numerical integration. While quenching the chips in water during the experiment, the pool of water was covered for the first 3 seconds, then the cover was removed and chips were collected in water during the next 2 seconds. Thus, the chips used for SIMS analysis were in contact with the tool sometime during the fourth or the fifth second of the cutting operation. A consistency in this procedure for collecting chips was not maintained during the operation at 200 m/min, and hence that result has not been included with the results at the other two speeds. As pointed out before, the flux so obtained represents the amount of tungsten diffused into the chip during the tool-chip contact time τ. Tables 5.5 to 5.7 show a comparison between the values of diffusion flux as predicted by the model under the three situations discussed therein with the values of flux calculated from experimentally observed concentration profiles.

Table 5.6

Comparison between the values of tungsten flux into the chip predicted by model II-a (44% effective machining time) and the experimentally determined values.

Cutting speed (m/min)	Flux (Theoretical) ($\mu g/cm^2$)		Grain size considered in Model (μm)	Flux (observed) ($\mu g/cm^2$)
	t= 4^{th} sec	t= 5^{th} sec		
150	0.052 0.037 0.024	0.061 0.044 0.029	0.1 0.2 0.5	0.201 ±0.007
240	0.279 0.204 0.141	0.330 0.242 0.169	0.1 0.2 0.5	2.02 ±0.05

Table 5.7

Comparison between the values of tungsten flux into the chip predicted by model II-b (93.3% effective machining time) and the experimentally determined values.

Cutting speed (m/min)	Flux (Theoretical) ($\mu g/cm^2$)		Grain size considered in Model (μm)	Flux (observed) ($\mu g/cm^2$)
	t= 4^{th} sec	t= 5^{th} sec		
150	0.095 0.078 0.051	0.129 0.093 0.061	0.1 0.2 0.5	0.201 ±0.007
240	0.592 0.433 0.299	0.670 0.513 0.358	0.1 0.2 0.5	2.02 ±0.05

It can again be seen that the values of diffusion flux based on the model are lower than the values of diffusion flux calculated from experimentally observed concentration profiles. Predictions based on the assumption of complete austenitization of the chip material were the highest of the three cases, but still were much below the values calculated from the experimentally observed concentration profiles. These results strongly indicate that there is a significant increase in the diffusivity of tungsten in the region. The models based on enhanced diffusion in the chip material, having a grain size of 0.1-0.5 μm, due to the contributions from stationary grain boundaries alone can not completely account for the observed enhancement. This aspect is dealt with in the next section where an internal consistency of the experimental data has been established with the help of backcalculated values of diffusivity of tungsten which would lead to the observed values of dissolution wear.

5-D : Internal Consistency of Experimental Results

In the preceding section, a comparison between the theoretical predictions and experimental results of dissolution wear process was presented at two times. Independent analytical techniques were used for experimental measurements. For a comparison between the two regarding the net result of a wear test of 30 second duration, the

dissolution wear database generated using INAA was used. On the other hand, for a comparison between the two at an instantaneous level, the results of SIMS analysis were used. Although at both levels of comparison the theoretical predictions fell short of the experimentally measured quantities, the factors by which the theoretical predictions were lower than the experimentally measured quantities were of the same order. This points to a systematic disagreement between the theory and the experimental measurements. In other words, there is a systematic enhancement in the diffusivity of tungsten in the chip material next to the tool-chip interface, which can not be fully accounted for by a model which considers stationary grain boundaries alone. This point has been discussed further in Chapter 6 (Discussion).

Diffusion coefficients of tungsten which would match the predictions of the thermokinetic model with the experimental results have been backcalculated. These are called **operative diffusion coefficients**. The factor by which the operative diffusion coefficient is higher than the expected diffusion coefficient of the chip material with a particular grain size is called the **enhancement factor**. Table 5.8 shows a comparison between the diffusional enhancement factors required for the theoretical predictions of Model I to match the results of two independent experimental techniques. At a cutting speed of 150 m/min,

Table 5.8

Comparison between the enhancement factors required to match the theoretical predictions with the results of SIMS analysis and the results of INAA.

Cutting Speed (m/min)	Enhancement Factors required to match the SIMS results			Enhancement Factors required to match the INAA results.		
	Time for back calculations	$\frac{D_{oper}}{D_{0.5\mu m}}$	$\frac{D_{oper}}{D_{0.1\mu m}}$	Time for back calculations	$\frac{D_{oper}}{D_{0.5\mu m}}$	$\frac{D_{oper}}{D_{0.1\mu m}}$
150	4^{th} sec	24.6	5.3	30sec (Total)	23.7	5.3
	5^{th} sec	16.9	3.4			
240	4^{th} sec	38.8	10	30 sec (Total)	20.2	5.7
	5^{th} sec	26.1	6.9			

there is a reasonably good agreement between the enhancement factors calculated from SIMS results, assuming that the chip used for SIMS analysis was in contact with the tool during the fourth second of cut, and the enhancement factors obtained from the total dissolution wear database generated using INAA. At a cutting speed of 240 m/min, there is a reasonably good agreement between the enhancement factors calculated from SIMS results, assuming that the chip was in contact with the tool during the fifth second of cut and the enhancement factors calculated from the total dissolution wear database generated using INAA. It follows that a similar agreement would be seen between the enhancement factors when either of the Models II(a) or (b) is used. This agreement, thus, serves to establish an internal consistency between the experimental results obtained using these two analytical techniques.

CHAPTER 6 : DISCUSSION

This chapter presents a critical examination of the following topics :

1) Choice of the technique used to generate a quantitative database on tool wear.
2) Dissolution wear as the dominant wear mechanism.
3) Development of a quantitative thermokinetic model based on enhanced diffusivities and its comparison with the convective model of solute transport.
4) Control of crater wear through solubilities of tool constituents in the chip material.

6-A.1 : Tool Wear Measurements Using INAA

It was shown in Chapter 4 that the technique of INAA can be successfully employed to establish a quantitative database on tool wear under certain conditions. These conditions are discussed in this section and it is shown that this technique has some distinct advantages over the conventional method of crater wear specification using a profilometer. The practice of activating the chips is shown to be safer and more convenient than the use of radioactive tools to generate a similar database. The quantitative database serves as a reference against which various models

of crater wear have been evaluated. Limitations of the technique used are discussed and it is shown how they have been overcome in this investigation.

6-A.2 : Irradiation of Tool Versus Irradiation of Chips

Most of the work related to the study of tool wear by radioactive techniques has been carried out by using a radioactive tool and by tracking the radioactivity transferred to the chips during machining. The activity of tool constituents in an average sample of chips has been shown to increase with an increase in cutting speed by Lunde and Anderson[76]. However, their results of tool wear are in the units of γ ray counts per min. and thus, are semi-quantitative in nature. Chawla *et al.* [77] have quantified flank wear by using the method of γ-γ coincidence counting of cobalt (the binder phase of the tool), again by using radioactive tools. Their analysis is based on the assumption that the ratio of the amount of binder phase to the amount of carbide material transferred into the chips remains exactly the same as the ratio of weight percentages of these phases in the cutting tool. This may not be true, especially if only a fraction of the total amount of chips generated during the cutting operation is actually used for analysis, instead of analyzing all the chips as done in this series of experiments.

The use of irradiated tools during machining also poses the problem of contamination of the lathe. The levels to which the tools must be irradiated to get sufficient counts corresponding to the radioactive isotopes of the tool constituents in the chips are as high as 1 R/hr at a distance of 1 ft. from the tool. Such high levels of radiation are dangerous and require very elaborate safety procedures during the machining tests. In addition to the above difficulties, this method is unsuitable for the analysis of short lived isotopes which might be of interest such as ^{51}Ti (Half life 5.8 min).

These difficulties can be overcome by collecting the chips produced during machining and irradiating them later at a convenient time. At this stage, the chips can be suitably encapsulated, irradiated to the required level and counted with the induced activities which can be handled safely in the INAA laboratory. Also, even very short lived isotopes can be analyzed by the use of prompt-gamma rays, provided that the workpiece doesn't contain elements which activate to produce other short lived isotopes which would lead to a large background masking the peak(s) of interest. Since tungsten carbide based tools were used in this investigation to generate crater wear database, the isotope ^{187}W was tracked in the activated chips. It has a sufficiently long half life of 24 hours, and hence a

counting time of 15 min. per sample could be chosen giving an excellent analytical precision of ±1 %. All the chips that could be collected during the cutting operation were irradiated and analyzed. This eliminated the errors associated with choosing a representative average sample of the chips, and gave the total amount of tungsten present in the chips.

6-A.3 : Conditions For Feasibility of Analysis of Chips

The method of generating a tool wear database by activating the chips can be used only under certain conditions, which are discussed here with reference to the appropriate experimental results.

1) The concentration of the element of interest (tungsten in this case) inherently present in the workpiece to be machined should be very low, preferably less than 10 ppm. As mentioned previously, the quantity of tool material transferred into the chips is obtained by measuring the increase in the concentration of tungsten in the chips above this base level. It was seen that at the highest cutting speed studied, i.e. 240 m/min, the increase in concentration of tungsten was equal to 11.2 ppm. Obviously, if an increase in concentration equal to 11.2 ppm is to be clearly distinguished, the inherent concentration of tungsten in the workpiece must be very low. For precisely this reason, a

quantitative database on dissolution wear of K-11 tools while machining austenitic stainless steel could not be generated. The stainless steel workpiece contained about 500 ppm tungsten.

2) The element of interest (tungsten in this analysis) inherently present in the workpiece should be homogeneously distributed. For example, in this study, the concentration of tungsten inherently present in the workpiece, as determined from the analysis of 14 samples, was found to be equal to 11.0± 0.5 ppm. Even if the analysis technique is very precise, an uncertainty of ±0.5 ppm arose due to inhomogeneity of tungsten in the workpiece material. The average concentration of tungsten in the chips generated at 240 m/min was found to be equal to 22.2± 0.06 ppm. Hence, the increase in the concentration of tungsten in the chips is equal to 11.2± 0.5 ppm. Thus, it can be seen that the major contribution to the uncertainty associated with the final result is from inhomogeneity of tungsten in the workpiece, which must be kept as low as possible.

3) In order to have a low detection limit, the sensitivity of the technique for the element of interest should be good. The neutron cross section of the element, as well as the number of γ rays produced per decay, determine the sensitivity for that element. This is usually very good for many elements of interest such as W, Hf, Ti, Co, Ta and Nb.

However, as a result of activation of the chips, depending on the workpiece material, a fairly large background is also generated on which the peaks of interest are located. The background at the energy level corresponding to the peak of interest is important in determining the detection limit for that element in the chip material, e.g. due to the iron background produced by the activated chips, the detection limit for tungsten was as high as 1 ppm for a sample containing about 12 g of chips. Since, the measured concentrations were always more than 11 ppm, this was not a limiting factor in this analysis. However, during the analysis of Hf in the chips produced by machining the same steel using HfN coated tools, the detection limit of Hf was a limiting factor. Due to the iron background, only concentrations of Hf above 0.7 ppm could be detected. Analysis of the chips showed that the Hf concentration was less than this detection limit. Thus, the concentration of Hf could be reported only to be less than 0.7 ppm, even though the interference free sensitivity for Hf is quite good. Thus, the detection limit should be considered along with the expected value of increase in the concentration of the element of interest in the chips. A comparison of the solubility products of various tool constituents in austenite at a typical temperature serves as a guide to their dissolution potential in chips.

4) Problems do arise if the workpiece contains high concentration of elements with high neutron cross sections, such as nickel.[78] These elements lead to significant flux depression during irradiation. If nickel is distributed inhomogeneously, the flux depression is not uniform and the effect is difficult to take into account during normalization. The neutron cross section of iron for thermal neutrons is much lower, however, and the flux depression in the present case is about 14 %. Since iron constitutes the matrix of the chips, the flux depression is uniform and was taken into account during normalization of results. Thus, for the analysis of tool wear during the machining of steels, the above technique can be successfully employed.

6-B.1 : Quantitative Tool Wear Database

In Chapter 4, the total amount of tool wear was quantified using the INAA technique. The results are based on the assumption that all the material lost from the tool is transferred to the chips and all of it is retained there. Given the fact that the tool-chip contact is very intimate, it is reasonable to assume that the tool material lost in the form of small fragments would be embedded firmly into the chips. Tool material lost as a result of dissolution wear process becomes an integral part of the chip at an atomic level, provided that there is no loss of tungsten in

the form of WO_3 due to oxidation when the chips are still hot after leaving contact with the tool. The possibility of tungsten oxidation is discussed in a subsequent section, where it is concluded that such losses are not significant.

Table 4.2 clearly shows that the contribution of flank wear to the total tool wear is less than 5% under the given conditions. Thus, crater wear is the dominant mode of wear for a K-11 tool (97 % WC) while machining a Ca-treated AISI 1045 grade steel workpiece at high speeds. This result quantitatively confirms the observations reported in the literature [79]. The strong influence of cutting speed on crater wear is clearly seen. This is in agreement with results reported in the literature using the conventional method of crater wear measurement. Both these observations are related to tool temperatures which are significantly higher on the rake face than at the flank wear land. The temperatures on the rake face, which were calculated from the measured values of forces and contact lengths were seen to be of the order of 1100^{o}C. This temperature is high enough for the thermally activated processes involved in dissolution wear to take place at an appreciable rate. These thermally activated processes are central to the micromechanisms of crater wear and are discussed in subsequent sections.

6-B.2 : Normalized Wear Rates

Wear rates were normalized with respect to sliding distance in order to compare crater wear rates at different cutting speeds, Fig.4.2(a). The normalized crater wear rate is seen to be influenced markedly by a change in the cutting speed. This result is in agreement with many other observations reported in the literature [33] using the conventional method of crater wear measurement. However, the normalized crater wear rates calculated here, by determining the quantities of material lost from the rake face of the tool, are not affected by any subjective error, such as that usually associated with the measurement of the depth of craters. The subjectivity in conventional method arises due to the irregular shape, as well as the shape change of the crater with cutting time.

By separating the mechanical and dissolution components of crater wear, and by studying their response to a change in cutting speed by means of the corresponding normalized wear rate components, the basic difference in the processes responsible for the two has been illustrated. Involvement of thermally activated processes in dissolution wear is indicated through a sharp increase in the corresponding wear rate with cutting speed, as the effect of cutting speed is to increase the temperature. Mechanical wear is a result of fracture processes taking place at a

microscopic level in the tool, and is seen to be relatively unaffected by temperatures in the range of temperatures encountered in this series of experiments.

6-B.3 : Micromechanisms of Crater Wear

Details of various micromechanisms of tool wear are given in Chapter 2. The study of contributions of these mechanisms to the net crater wear under given cutting conditions has remained largely qualitative. However, in this investigation, it is shown that quantification is possible, and it is illustrated that dissolution wear can contribute up to 93 % of the total crater wear under the cutting conditions used in this series of experiments (Table 4.5). This result quantitatively confirms the observations reported in literature[20].

The contributions of mechanical wear and dissolution wear to total crater wear were separated out by the procedure of dissolution of chips in hydrochloric acid followed by filtration through 0.2 micron filters as described earlier. Choice of the pore size of the filters was guided by the size of tungsten carbide particles in the tool, which varied from 1 to 5 micron. So, most of the microscopic fragments of the tool embedded in the chips can be assumed to be bigger than 0.2 micron and would be collected on the filter. A piece of workpiece, weighing 100

gm. was dissolved in hydrochloric acid and the solution was filtered out in the same way. Analysis of the residue showed no tungsten signal, which indicated that there were no tungsten carbide particles of size equal to or greater than 0.2 micron inherently present in the workpiece. Thus, all the tungsten carbide particles present on the filters clearly came from the tool material transferred to the chips. A possible source of error in the experimental determination of mechanical wear of tools was through a loss of the fragments during filtration of the large amounts of solution of chips. Due care was taken to minimize these losses as much as possible. Thus, within the limits of experimental errors, it can be concluded that the contribution of mechanical wear processes to the total crater wear is not significant for the tool-workpiece combination and the cutting conditions used in this investigation.

6-C : Activation Energy of Dissolution Wear

Since thermally activated processes are involved in dissolution wear, the dissolution wear database should follow an Arrhenius type relationship. Fig.6.1 shows that this is indeed the case, and the fit of the experimentally determined dissolution wear amounts to the reciprocal of the tool-chip interface temperatures (averaged over 30 seconds)

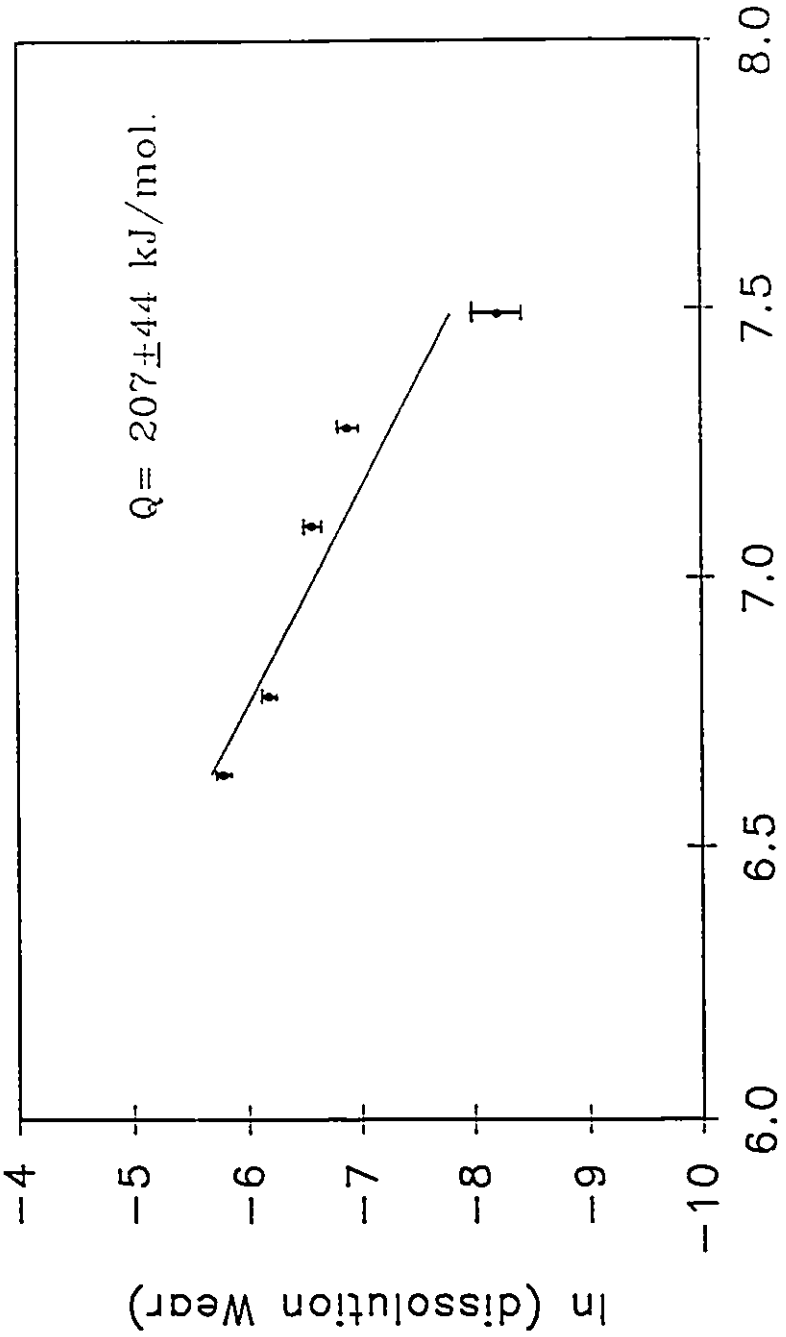

Fig.6.1 Determination of the activation energy of dissolution wear.

is reasonably good. The value of regression coefficient for the fit is found to be equal to 0.9372. The activation energy for the dissolution wear process was derived from the slope of the straight line obtained in Fig.6.1 and was found to be equal to 207±44 kJ/mol. The average interface temperature is fixed by the cutting conditions, and its range is less than 200°C for the range of cutting speeds employed in this investigation. It is recognized that the activation energy, determined over a rather small temperature range, has its limitations. However, some important observations can still be made, which are discussed below:

The importance of $C_o \cdot \sqrt{D_{eff}}$ term in dissolution wear was shown in the last chapter on thermokinetic model and it is also discussed in a subsequent section of this chapter. The values of C_o (for complete austenitization of flow zone) and D_{eff} (for 0.2 μm grain size), calculated in Chapter 5 are given by the following equations:

$$C_o = 2090.4 \exp(-Q_1/RT), \text{ (g/cc)} \qquad Q_1 = 99.7 \text{ kJ/mol} \quad (6.1)$$

$$D_{(eff)} = 0.018 \exp(-Q_2/RT), \text{ (cm}^2\text{/s)} \qquad Q_2 = 198.1 \text{ kJ/mol} \quad (6.2)$$

The activation energy for the lattice diffusion of tungsten in γ iron is 317.3 kJ/mol, and the activation energy for the diffusion of tungsten along the grain boundaries of high

Table 6.1

The experimentally determined values of the activation energy of crater wear.

Investigator	Tool Grade	Workpiece	Activation energy (kJ/mol)
Mathew, P [23]	P30 (ISO)	0.2 % C Steel	105.78
	P30 (ISO)	0.38 % C Steel	129.02
Takeyama and Murata [48]	P10 (ISO)	Cast Iron	422.02
	K20 (ISO)	Heat resistant steel	327.0
Cook [81]	WC-Co	AISI 1045	238.8
Present work	K-11	AISI 1045 Ca-treated steel	207 ± 44

speed steel (fcc phase) is equal to 194.1 kJ/mol. The $C_o \cdot \sqrt{D_{eff}}$ term calculated from the above expressions has an activation energy term equal to 198.8 kJ/mol., which is in good agreement with the value derived in the present analysis, 207± 44 kJ/mol. It can also be seen that the activation energy for grain boundary diffusion is close to the activation energy of dissolution wear, which underscores the role of grain boundaries in dissolution wear.

Similar attempts to calculate the activation energies have been made by Takeyama and Murata [48], Mathew [23] and Cook [81], and their results have been summarized along with the results of present investigation in Table 6.1. The values of activation energy depend on the specific tool-workpiece combination and hence can not be directly compared. However, they are seen to be of the same order. It is important to note here that crater wear was determined in all of these investigations by measuring the maximum depth of crater, in contrast to the methcd used in the present analysis.

It may be recalled from chapter 5 that the factors controlling the dissolutiсn wear amounts according to the diffusional theory are :

1) The interfacial concentration of tungsten.
2) The diffusivity of tungsten in the diffusion zone.

3) The tool-chip contact time, τ.

4) The tool-chip contact area.

The first two of these four parameters show an exponential dependence on the interface temperature. However, the temperature itself does not remain constant, and shows an increase with time during the 30 second wear test as shown in Fig.4.8. Also, the increase of tool-chip interface temperatures with time is not exactly in the same fashion at all cutting speeds. At a cutting speed of 150 m/min. the increase is slow but steady from 978 C to 1105 C whereas at a cutting speed of 240 m/min, the temperature quickly rises in the first 5 to 7 seconds and then tends to flatten out. An averaged value of temperatures over 30 seconds is used in Fig.6.1 to obtain the value of activation energy.

The remaining two parameters, the tool-chip contact area and the tool-chip contact time are fixed by the system at the start of a cut. Unlike the first two parameters, the tool-chip contact area and the contact time do not depend on the temperature in an exponential manner. Nevertheless, the tool-chip contact areas are influenced by the interface temperature for reasons outlined below :

As a result of tool loss leading to crater wear, a new surface is created underneath the chips, and hence the tool-chip contact area is increased. Due to an increase in

the contact area, tool-chip seizure takes place over a larger area. The sliding tool-chip contact area also increases. This leads to an increase in the force opposing the movement of the chip over the rake face of the tool. As a consequence, the tool-chip interface temperature increases resulting in an increase in the dissolution wear rate. An increased dissolution wear translates into an increase in contact areas as stated before.

Since the last two parameters controlling dissolution wear neither show an exponential dependence on temperature nor remain constant, a very good fit of the experimental data to an Arrhenius type of equation can not be expected. Despite these reasons, the observed fit is reasonably good. This suggests that the solubility and diffusivity are the dominant factors controlling the process of dissolution wear.

6-D : SIMS Analysis

6-D.1 : Diffusional Processes In Dissolution Wear

Concentration profiles of tungsten and cobalt next to the tool-chip interface of water quenched chips generated at various cutting speeds were obtained by means of SIMS analysis and were presented in Chapter 4. Similar concentration profiles were observed from the chips of medium carbon steel and austenitic stainless steel. In the

case of medium carbon steel chips, however, there was a surface depletion of tungsten up to a depth of approximately 0.08 μm. In both the cases, the maximum tungsten concentration increased with cutting speed. Similar results have been reported by Akasawa *et al.*[82], though their results show a profile of intensities of secondary ions, which need to be converted into the respective concentrations by using suitable standards. Thus, the observation that tungsten is present in elemental form in the chips corroborates the idea of dissolution of the tool into the chips leading to wear and validates the dissolution wear database generated using INAA.

The shape of the observed tungsten concentration profiles is characteristic of a diffusional process. However, one must be very careful in correlating the observed concentration profiles with the profiles which actually exist at the end of the tool-chip contact time. The experimentally determined concentration profiles, which extend to depths of about 0.5 μm inside the chip, represent the profiles after solute redistribution during the in-flight time of approximately 0.5 s prior to the entry of the chips in water. In comparison, the depth of penetration of tungsten at the end of tool-chip contact time, calculated from the operative diffusion coefficients, is of the order of 100 to 200 Å, i.e. 0.01 to 0.02 μm resulting from

tool-chip contact of about half a millisecond. Though the shape of the concentration profile is usually maintained after redistribution, it is to be emphasized that in this particular case quenching can not prevent drastic solute redistribution wherein the depth of penetration of tungsten is changed from 0.02 μm to 0.5 μm. Thus, it can not be unequivocally concluded that the profile existing during the tool-chip contact also had the same shape characteristic of a diffusional process of solute transport.

The concentration profiles existing at the end of the tool-chip contact time will have a shape characteristic of the mode of transport of tungsten away from the interface. If the mode of transport is diffusion, then the shape will be similar to the experimentally observed redistributed profile. If the mode of transport is convective flow, as suggested in the Kramer model[47], the shape will be entirely different reflecting the characteristics of the flow. However, the areas under these curves must equal the areas under the experimentally observed redistributed profiles. It was shown in Chapter 5 that the areas representing the values of diffusion flux in tool-chip contact time based on the thermokinetic model were lower than the areas under the observed concentration profiles by a certain factor. However, the value of this factor was found to be close to the factor by which the

prediction of net dissolution wear based on the thermokinetic model in 30 seconds fell short of the experimentally measured values of dissolution wear during the 30 second wear tests. Also, the activation energy of dissolution wear was found to be in good agreement with the value predicted on the basis of thermokinetic model. Thus, even though the mechanism of solute transport operative during the tool-chip contact time can not be unequivocally established, the above analysis favours the principle of diffusional transport of solute away from the interface.

6-D.2 : Surface Depletion of Tungsten in 1045 Steel Chips

The SIMS results can be used to examine the loss of dissolved tungsten from the hot chip surface after the chip leaves contact with the tool. Figs.4.9 to 4.11(a) show a depletion of tungsten to a depth of about 0.08 μm. Such depletion was seen in all the medium carbon steel chips examined. This observation may lead to the conclusion that elemental tungsten, originally present in the surface layers of a hot chip, is lost in the form of volatile WO_3. This would result in a depletion of tungsten at the surface and the establishment of a reverse diffusion profile to a depth of about 0.08 μm inside the chip[83]. However, the following observations can not be explained by this hypothesis :

1) In the same medium carbon steel chip samples, the

concentration profiles of cobalt also exhibit a similar surface depletion. Figs.4.9 to 4.11(b) show that the depth of cobalt depletion is equal to that of tungsten depletion. Since cobalt doesn't form volatile oxides, there is no possibility of cobalt depletion through direct oxidation. Thus, oxidational loss is most likely not the reason for the surface depletion of tungsten as well.

2) The concentration profiles of tungsten observed in the chips of austenitic stainless steel showed no tungsten depletion at the interface. The temperatures reached at the tool-chip interface while machining austenitic stainless steels were actually higher by about 75^{o} C than the temperatures reached while machining medium carbon steel at corresponding cutting speeds. This is a direct result of lower thermal conductivity of stainless steel. However, it is observed that despite conditions which are more favourable for oxidation, no surface depletion of tungsten occurred. This suggests that in the case of medium carbon steel chips too, tungsten oxidation did not take place to any significant extent.

The observed depletion of tungsten in the case of medium carbon steel chips can be attributed to the formation and growth of a thin iron oxide layer on the chip. FeO is formed at the high temperatures reached at the chip surface [83-b] and is known to have a highly defective structure. The

oxide is known to grow by diffusion of Fe^{++} ions outward through the oxide, which would effectively lower the concentration of tungsten in the region. Similar depletion in concentrations of tungsten and cobalt was observed by Akasawa *et al.* [82] in the chips of low and medium carbon steel. Such oxidation was most probably suppressed in the case of stainless steel chips owing to high oxidation resistance of the material. Consequently, no tungsten depletion was observed at the surface of austenitic stainless steel chips.

6-E : Critical Examination of The Thermokinetic Model

6-E.1 : Boundary Conditions

In the present model, the concentration of tungsten at the interface has been calculated from the solubility product of tungsten carbide in austenite rather than in ferrite. Kramer [49] and Trigger [24] however, have argued in favour of the ferrite-pearlite microstructure being retained in the chip material as it slides over the tool because of the short tool-chip contact times of the order of half a millisecond. On the other hand, Shelbourn *et al.* [13] and Hau-Bracamonte [14] have reported microstructural evidence from the secondary shear zone showing partial austenitization of the chip material. The large areas of twinned martensite observed in the quenched chips studied in

this series of experiments clearly indicates that austenitization does occur. Wingrove [84] has reported the similar presence of martensite in the structure of adiabatic shear bands. The dissolution of cementite plates in a matter of milliseconds was explained by Rogers [12] to be due to the severe elongation and consequent thinning of the cementite plates leading to very high surface energies at temperatures where cementite is thermodynamically unstable.

The influence of following two variables on the interface concentration of tungsten should also be considered :

1) The effect of pressure on interfacial concentration.
2) Surface segregation effects.

Pressure Effect : Pressure effect is taken into account by considering a $P \cdot \Delta V$ term with the relevant ΔG^{o} values. The ΔG^{o} values for dissolution of tungsten carbide in austenite with respect to the infinite dilution standard states are reported by Urhenius [72] and are given by the following equation :

$$\Delta G^{o} = -134630 + 40.827 \cdot T \quad \text{Joule} \qquad (6.3)$$

Values of the $P \cdot \Delta V$ term can be used to calculate the temperature difference that would bring about the same change, and then the significance of the $P \cdot \Delta V$ term can be

judged. This has been done using the ΔV value reported by Kramer [49] which is equal to 2.01 cm^3 for the dissolution of 1 mole of tungsten carbide. Typical stress distributions reported in literature [85] show that the normal stress is very high at the cutting edge, but drops rapidly and is typically less than 200 MPa over most of the contact area under cutting conditions similar to those employed here. At a pressure of 200 MPa, the $P \cdot \Delta V$ term is equal to 402 J and is equivalent to the change in the value of ΔG° due to a change in temperature equal to 10° C. The calculated values of average interface temperatures themselves are likely to have a higher uncertainty. The effect of pressure on solubility is, therefore, neglected.

Segregation Effects : The equilibrium surface solute solubility is reported to be markedly different from that in bulk for many solute elements. Buckley [86] has shown that this segregation effect can be very important in determining the friction and wear properties of solids at room temperature. Analysis of the segregation effect has been reported by Ferrante [87] who considered a lowering in (strain) free energy of the solid by solute segregation to be the driving force for solute segregation. The following equation relates the two solubilities :

$$C_s = \frac{C_o \cdot \exp(Q/RT)}{1 - C_o + C_o \cdot \exp(Q/RT)} \qquad (6.4)$$

where, C_s is the fractional surface concentration,

C_o is the fractional bulk concentration, and

Q is the activation energy for solute segregation.

The Q value depends on the difference in the atomic radii of the solute and solvent, the shear modulus of the matrix, and the interaction of excess electrons from the solute atoms with the surface. The Q value experimentally obtained by Ferrante for aluminum segregation in Cu-5% Al is equal to 1050 cal/mol. The difference in atomic radii of γ iron and tungsten is equal to 0.08 Å, compared to a difference of 0.15 Å between the atomic radii of copper and aluminium. However, the shear modulus of iron is 81.6 GPa, compared to a value of 48.3 GPa for the shear modulus of copper. Thus, the Q value for Fe-W system is expected to be of the same order as the Q value for Cu-Al system.

At a typical chip temperature of 1400 K, when wt. fraction tungsten corresponding to the bulk solubility C_o equals 0.05, a Q value of 1050 cal/mol results in a C_s/C_o ratio equal to 1.4. However, it is emphasized that the surface segregation is confined to only the first atom layer. The maximum solubility of tungsten from the second

layer onward into the bulk, is equal to C_o. As C_o and C_s represent the equilibrium solubilities, it follows that the activity of tungsten in the first atom layer is equal to that in the second atom layer, even if the two concentrations are not.

The diffusion profile of tungsten, in presence of surface segregation, is seen as a sudden drop in the concentration of tungsten from C_s at the first layer of the chip to C_o at the second atom layer of the chip. The subsequent variation of concentration is given by the error function solution described in Chapter 5. Thus, the effect of tungsten segregation is to add a spike on the tungsten profile. The spike has a height C_s-C_o, and its width is equal to the atomic diameter of iron. The diffusion profile of tungsten, generated at the end of tool-chip contact time τ, as calculated from the operative diffusion coefficients, is seen to extend into the chip up to 100-200 Å. Thus, the contribution of diffusion flux, arising from the above spike, is a negligible fraction of the total diffusion flux at the high chip temperatures.

6-E.2 : Assumptions

6-E.2.1 : Nature of Tool-Chip Contact

Only under the conditions of intimate contact between the given surfaces, are atomic level interactions

between the two possible. It was assumed in the thermokinetic model that such intimate contact does exist between the tool and the chip. The stresses at the tool-chip interface are known to be high[85], and the occurrence of seizure between the tool and the chip during metal-cutting under such high stresses has been evidenced in literature[11]. Thus, the assumption regarding the nature of tool-chip contact can be safely considered to be a valid one.

6-E.2·2 : Attainment of Local Equilibrium

The attainment of surface equilibrium is a common assumption made in the solution of thermokinetic problems. The frequency of vibrations of the atoms is very high, of the order of 10^{12} Hz. At the high temperatures encountered in metal cutting, the fraction of successful atom jumps is significant. The time required by tungsten atoms to jump by one interatomic distance and establish equilibrium concentration in the first atom layer in the surface of the chips is estimated to be of the order of tens of nanoseconds. This time period is very small compared to the tool chip contact time of about half a millisecond. Thus, the assumption regarding establishment of local equilibrium at the interface during metal cutting is valid.

6-E.2·3 : Appropriate Value of Diffusivities

The Bhattacharyya model did not consider the effect of plastic deformation on the diffusivity of tungsten in the immediate vicinity of the tool chip interface. The Kramer model also examined the contribution of diffusion to the total dissolution wear through the consideration of lattice diffusion coefficients alone, and concluded that this contribution is not significant. However, the microstructural features of the secondary shear zone observed in this investigation, indicate that the effective diffusivity of tungsten is increased greatly due to the significant contribution of grain boundary diffusion. The enhanced values of diffusivities were presented in Chapter 5.

The possible effect of two additional parameters on further influencing these enhanced D values is discussed below :

1) The Effect of Pressure on Diffusivities : The effect of pressure on diffusion coefficients is calculated through the consideration of activation volumes [88] using the following equation :

$$\ln (D_2/D_1) = - \frac{1}{RT} \cdot V_{act} \cdot (\Delta P) \qquad (6.5)$$

where, V_{act} is the activation volume of vacancies.

Activation volume of vacancies in austenite is not available. However, based on the values reported for other metals by Shewmon [89] a value of 0.5 times the molar volume can be used as an upper limit in the calculations. (Activation volume of vacancies in the grain boundary is much lower than that in the lattice.) For a pressure of 200 MPa on the secondary shear zone of the chip, at a temperature of 1100 C, $D_2 = 0.94 \cdot D_1$. Thus, the effect of pressure under typical metal cutting conditions on the diffusivity of tungsten is less than 10 % and can be neglected.

2) Effect of grain boundary migration : The enhancement in diffusion coefficients calculated previously can increase even further if the grain boundaries are not stationary during the tool-chip contact time. It has been shown by Hillert and Purdy [90] that diffusivities along migrating grain boundaries are higher than the diffusivities along stationary grain boundaries, depending on the velocity of the boundaries. Olander *et al.* [91] studied the effect of the relatively slow migration of boundaries, resulting in grain growth observed during diffusion anneal experiments carried out to determine grain boundary diffusivities. They report that the tracer diffusivity along the grain

boundaries in lead is approximately 5 times that deduced from stationary boundary theories. Boundaries within the material next to the tool-chip interface are quite likely to be the moving ones in response to high temperatures, low grain sizes, and diffusion along the boundaries. Unfortunately, there is no such database available in literature for the Fe-W system, and hence this effect could not be incorporated into the model.

6-E.2·4 : Variation of Metal Cutting Parameters With Time

The assumption made in the Bhattacharyya model regarding constancy of contact lengths, contact areas and interface temperatures during a cutting test was shown to be inappropriate during wear tests carried out using K-11 tools. As mentioned before, the rapid dissolution wear of these tools leads to a significant increase in tool-chip contact areas. Increased tool-chip contact areas translate into increased forces opposing the movement of the chip over the tool and, consequently, an increase in temperature. It must be emphasized here that even though the temperatures show a rapid increase with time, it does not represent a transient state from heat transfer point of view. It has been shown [24] that heat transfer is so rapid that steady state temperatures are reached at the tool-chip interface in

a matter of milliseconds. The observed increase in interface temperatures is, thus, due to increasing contact lengths and increasing forces. To account for this variation, dissolution wear amounts were calculated for every interval of 1 second duration, and these values were numerically integrated to obtain the final result based on the thermokinetic model.

6-F : Predictions Based on Thermokinetic Models

Three possible boundary conditions depending on the three microstructural possibilities for the state of the chip material next to the tool-chip interface were considered in Chapter 5. The predicted dissolution wear amounts in each case were presented in Tables 5.2 to 5.4. To facilitate a comparison between these models, the boundary conditions distinguishing the models are recapitulated below:

Model I : Complete austenitization of the chip material next to the interface. All the cementite plates in this region dissolve in austenite.

Model II(a) : Only the bcc to fcc transition occurs. Metastable cementite plates are present. Cementite plates block diffusion of tungsten into all the pearlitic ferrite. The effective cutting time is 44% of the actual cutting time.

Model II(b) : Only the bcc to fcc transition occurs. Metastable cementite plates are present. Cementite plates do not block diffusion of tungsten in pearlitic ferrite. The effective cutting time is 93.3% of the actual cutting time.

It can be seen from Tables 5.2 to 5.4 that the dissolution wear predicted by Model 1 are the highest of the three models followed by the dissolution wear predicted by Model 2. The third model predicted much lower values. However, the predictions of all the three models fell well below the experimentally measured values of dissolution wear. At a cutting speed of 240 m/min, considering a grain size of 0.1μm, the predictions of dissolution wear based on the three models were equal to 46.6%, 18.9% and 40% , respectively of the experimentally measured values. The ultrafine microstructure of chip material in the immediate vicinity of the tool-chip interface indicates that Model 1 is the closest to reality. However, the fact remains that even Model 1 can account for just 46.6 % of the observed values of dissolution wear. Nevertheless, it is observed that the contribution due to diffusional solute transport is equal to 46.6% of the measured values of dissolution wear amounts. A fraction of 46.6% is clearly not negligible, and thus, the results are not in agreement with the Kramer model.

An effective grain size required to match the

predictions of thermokinetic model with the experimentally measured dissolution wear can be back-calculated. Model I leads to the following back-calculated values :

Cutting Speed (m/min)	Effective Grain Size (μm)
150	0.017
180	0.004
200	0.006
220	0.015
240	0.015

It is interesting to note that the effective grain sizes during cutting at 150, 220 and 240 m/min are almost the same. This grain size is of the same order as the size of the nuclei, expected in a nucleation and growth process such as recrystallization. The observed grain sizes of 0.2-0.5 μm represent a result of grain growth during the in-flight time of the chips prior to their entry in water, which is approximately half a second. The question whether the grain size actually present during the tool-chip contact can really be equal to these back-calculated values can be analyzed with the help of the kinetics of grain growth. Grain growth is known to be very rapid at small grain sizes

and high temperatures, the conditions which typically exist in the secondary shear zone. Unfortunately, such study has not been reported in the literature. The austenite grain growth kinetics are available for long annealing times, of the order of tens of hours. However, the extrapolation of this data to very short times is not valid. Also, the grain growth rates are greatly reduced by parameters such as the presence of second phase particles (e.g., small undissolved cementite particles) and the presence of solute atoms. Therefore, the existence of nm size grains during the tool chip contact remains only a possibility, which can neither be confirmed nor ruled out.

Another mechanism of enhancement of diffusivity in the region arises due to grain boundary migration, as discussed before. The conditions existing in the immediate vicinity of tool-chip interface are conducive to the migration of grain boundaries. The submicron grains have very high surface energies, which the system will try to reduce through the process of grain growth involving grain boundary migration. The activation energy for grain growth is readily available at the high temperatures reached at the tool-chip interface. Diffusion induced grain boundary migration (DIGM) has been reported in numerous alloy systems. Though it has not been studied in the Fe-W system, the possibility of DIGM occurring can not be ruled out.

Unfortunately, due to a lack of relevant database, the diffusion enhancement by migrating grain boundaries could not be quantitatively incorporated in the thermokinetic model.

The thermokinetic model considered that diffusional mass transport took place for a time equal to the tool-chip contact time. In Model I, it was assumed that the chip would be in a fully austenitic form for the entire duration of contact time. However, this represents a simplified picture of a very complicated problem. In most of the cases, the sticking contact length is about 40-50 % of the total contact length. This is the region of severe plastic deformation and the consequent ultrafine grain formation. In other words, the ultrafine grains are formed after some tool-chip contact time has elapsed. Thus, a completely austenitic structure with ultrafine grain size is expected to be operative for only a part of the tool-chip contact time. Also, at what point in time, the grain boundaries would start moving remains to be established. Thus, there is a scope for further refinements to the thermokinetic model.

Based on the above discussion, it is proposed that a quantitative thermokinetic model, further refined to take into account the full extent of diffusion enhancement, may account for all the observed dissolution wear.

6-G : Diffusive Versus Convective Transport of Tungsten

The thermokinetic models discussed here and the Kramer model for dissolution wear assume that a specific concentration of the tool constituent (tungsten) is maintained in atomic form in the first atom layer of the chip surface at all times during tool-chip contact. During the tool-chip contact time, if some of this tungsten is transported away from the interface into the chip then more tool dissolution would take place so that the concentration at the surface is restored to C_o. Thus, the interfacial concentration and the rate of transport together determine the dissolution wear rate. The Kramer model (described in Chapter 2) argues that diffusional mass transport is negligible and proposes a bulk flow of chip material perpendicular to the tool-chip contact area thereby transporting the solute with it. The thermokinetic model, on the other hand, considers atomic diffusion in response to a concentration gradient to be the operative mechanism of solute transport. These two mechanisms are examined here by comparing the assumptions made in the two models and their predictions in light of the experimental results obtained in this investigation.

A) State of the Chip Material : The convective model assumes that the flow of chip material around the tool tip bears a

resemblance to the flow of a fluid around an obstruction. Therefore, boundary layer theory is assumed to be applicable to the problem. The thermokinetic model, on the other hand considers the chip material in the immediate vicinity of the tool-chip interface to be a crystalline solid undergoing adiabatic plastic deformation at strain rates of the order of $10^4 s^{-1}$. The temperatures calculated from the experimentally measured values of forces and the tool-chip contact lengths are around 1200 C, whereas the melting point of 0.45 wt.% C steel is around 1500^{o} C.

B) Interfacial Concentrations of Tungsten : The convective model considers the equilibrium solubility of the tool material in ferrite to be appropriate, based on the assumption that the ferrite to austenite transformation can not take place in the above material during the tool-chip contact time. The thermokinetic model assumes that this transformation does take place, and considers the solubility accordingly. TEM analysis of water quenched chips showed large areas of fine twinned martensite which indicates austenitization in the chips. SEM pictures also showed an absence of cementite in the immediate vicinity of the tool-chip interface.

C) Diffusivity of Tungsten : The Kramer model calculates the

quantity of diffusional solute transport away from the tool-chip interface based on the lattice diffusion coefficient of the solute (tungsten) in ferrite. The thermokinetic model considers tungsten diffusion in very fine grained austenite. The observed grain sizes in the chip material next to the interface were about 0.2 μm. The grain boundary area fraction under such conditions is high enough to enhance the diffusivity in the region by an order of magnitude, even without taking boundary migration into account.

D) Mechanism of Solute Transport : The convective model proposes a bulk flow in response to velocity gradients in the chip which exist during the sticking contact between the tool and the chip. The mechanism of this bulk flow has been described as 'turbulent mixing at the atomic level'. The thermokinetic model, on the other hand, proposes diffusion to be the mechanism responsible for solute transport. No other work regarding the phenomenon of bulk flow in solids could be found. In the convective model, the velocity of bulk flow was obtained from the mass balance equation applicable to fluids exhibiting a boundary layer. However, in the case of solids, the existence of this kind of flow is questionable because solids can deform in response to velocity gradients, whereas liquids do not (because they are

not rigid). The velocity gradient existing in the chip material has been correlated to the plastic shear rate by Zorev[92]. However, due to drastic solute redistribution during the in-flight time of the chips it is difficult to draw an unequivocal conclusion regarding the mechanism of solute transport based on the concentration profiles of tungsten.

E) Agreement of the Model With the Generated Database : The wear rate equation in the Kramer model involves the velocity of convective flow, V_c, which can not be readily calculated. Hence, the predictions of the Kramer model under given cutting conditions cannot be checked against the experimentally generated database. In addition, the Kramer model expresses the wear rate in terms of rate of increase of the maximum depth of crater, V_{wear}, whereas the database generated here is in terms of the total quantity of tool material dissolved away from the crater. Predictions based on the thermokinetic model were found to be much less than the experimentally measured values. However, the contribution of diffusive transport of the solute should be negligible if the model of convective flow holds good, and this was not found to be the case. An alternative explanation based on further diffusion enhancement is proposed to explain the observed differences.

F) Predicted Ratios of Wear Rates With Two Tool Materials: The Kramer model proposes that the velocity of convective flow, V_c, remains the same irrespective of the tool-workpiece combination. Thus, the predicted ratio of the wear rates for two cutting tool materials is given as follows :

$$\frac{V_{1\ wear}}{V_{2\ wear}} = \frac{(K \cdot C_o)_1}{(K \cdot C_o)_2} \qquad (6.6)$$

where, K is the ratio of molar volumes of the tool material being dissolved and the deforming workpiece material.

If the tool-chip contact areas are the same during wear tests carried out using two different tool materials, the ratio of wear rates as predicted by the thermokinetic model can be written as follows :

$$\frac{\dot{W}_1}{\dot{W}_2} = \frac{(C_o \cdot \sqrt{D})_1}{(C_o \cdot \sqrt{D})_2} \qquad (6.7)$$

These predicted ratios will not be very much different from each other if the D values for different tool constituents (especially the grain boundary diffusivities) are close.

Unfortunately these values are not available, and hence the two predictions cannot be quantitatively compared.

6-H : Controlling Dissolution Wear Through Solubilities

The importance of the $C\cdot\sqrt{D}$ term in controlling dissolution wear was highlighted in the last section. The equilibrium solubilities of potential tool materials can be obtained from their solubility products in austenite, as shown in the last chapter for the case of tungsten carbide. The values of grain boundary diffusion coefficients of many tool constituents are not known even for the case of stationary grain boundaries. Nevertheless, in the present investigation, an attempt was made to examine the performance of hafnium nitride coated tools in the light of the thermokinetic model of dissolution wear, and the results were presented in Chapter 4.

The large difference between the wear rates observed in the two cases indicates that the $C_o\cdot\sqrt{D_{oper}}$ values for the case of HfN coated tools are much lower than the corresponding values for the case of uncoated K-11 tools. A comparison between the temperatures reached at the tool-chip interface while machining medium carbon steel at a cutting speed of 240 m/min using these two tools was presented in Fig. 4.16. It can be seen that the temperatures reached at the coated tool-chip interface are lower than the

Table 6.2

Solubility products of potential tool materials at 1400K in austenite, expressed as $(wt\%)^2$.[93,94]

$[Ti]\cdot[N] = 1.34 \times 10^{-6}$	$[Ti]\cdot[C] = 7.04 \times 10^{-6}$
$[Zr]\cdot[N] = 2.34 \times 10^{-7}$	$[Zr]\cdot[C] = 1.64 \times 10^{-2}$
$[Hf]\cdot[N] = 3.15 \times 10^{-7}$	$[W]\cdot[C] = 4.08$
$[Nb]\cdot[N] = 3.54 \times 10^{-4}$	$[Nb]\cdot[C] = 5.99 \times 10^{-3}$
$[Ta]\cdot[N] = 1.26 \times 10^{-4}$	$[Ta]\cdot[C] = 7.94 \times 10^{-3}$
$[V]\cdot[N] = 2.60 \times 10^{-3}$	$[V]\cdot[C] = 8.60 \times 10^{-1}$

corresponding temperatures for the uncoated tool-chip interface by just about 75 ^{o}C. Thus, a large difference between the $C_o \cdot \sqrt{D_{oper}}$ values for the two cases has most likely arisen due to a large difference in the solubility products of WC and HfN in austenite at a given temperature. At a temperature of 1127^{o} C the solubility products of WC and HfN in austenite are equal to 4.08 $(wt.\%)^2$ and 3.15 $\times$ $10^{-7}(wt.\%)^2$ respectively. Thus, the significant difference between the dissolution wear rates observed in the two cases using the technique of INAA is consistent with the corresponding differences in the solubility products of the two materials in austenite.

The solubility products of potential tool materials in austenite at 1127^{o} C are given in Table 6.1. Materials such as TiN and HfN are seen to have very low solubility products in comparison to WC. The solubility product database, thus, constitutes the framework on which the choice of wear resistant tool coating should be based. However, in addition to controlling dissolution wear the design of wear resistant coatings involves consideration of other important factors such as adhesion between the tool and the coating, the generation of thermal stresses at the tool-coating interface due to differential thermal expansion and the possibility of formation of brittle phases at the tool-coating interface. An in-depth evaluation of the

performance of any tool coating involves the assessment of all these parameters. Such assessment is beyond the scope of this investigation.

The results of wear tests using K-1 tools instead of K-11 tools showed a reduction in crater wear rates by about 50%. At all the cutting speeds, the mechanical wear rates were not significantly affected, whereas the dissolution wear rates were reduced considerably. It may be pointed out that the Ta(Nb)C content of K-1 tools is 4 wt % as opposed to 0.4 wt % in K-11 tools. This result is in qualitative agreement with the predictions of dissolution wear theory, where an increase in the concentration of a tool constituent having a low solubility product is seen to decrease crater wear.

6-I : Inclusion Characteristics and Mechanical Wear

The deleterious effects of hard and abrasive alumina inclusions in promoting flank wear of cutting tools has been well established[30]. The calcium treatment of steel during deoxidation resulting in the formation of 'soft' calcium aluminosilicate inclusions has resulted in marked improvement in flank wear characteristics of cutting tools. These soft inclusions also lead to a lowering of crater wear. The effect of soft aluminosilicate type inclusions in

reducing crater wear is twofold. A) These inclusions are known to form protective layers on the rake face of the tool under certain conditions, [61,63] thereby reducing the dissolution component of crater wear,and B) Soft inclusions are also expected to lower the mechanical component of crater wear. A discussion of these aspects is appropriate, since Ca- treated AISI 1045 steel was used in this investigation as the workpiece material.

The conditions required for the formation of protective layers of the inclusion material while cutting in air are as follows:

1) Soft, low melting inclusions should be present in the workpiece material.

2) Tool materials should contain constituents having good wettability to these inclusions or which can react with the inclusions.

3) the cutting speed should be sufficiently high for the inclusions to become soft and deform.

In the present investigation, the first and the third conditions are fulfilled, but the second condition is not. Referring to the compositions of K-11 and K-1 tools given in Chapter 3, it is observed that tool constituents such as TiC and TiN are absent, without which the wettability of tools to the calcium aluminosilicate inclusions is known to be poor[63]. Thus, even if the right

type of inclusions is present in the workpiece, no inclusion layers are expected on the rake face of the tool. In other words, the dissolution wear rates are unaffected despite the presence of calcium aluminosilicate inclusions in the workpiece in these experiments. However, the mechanical component of crater wear was observed to be dependent on inclusion characteristics.

A comparison of the observed mechanical wear rates during the machining of AISI 1045 steels with and without calcium treatment was presented in Fig.4.18. The normalized mechanical wear rates observed while machining the steel produced without calcium treatment were higher at both the cutting speeds investigated by about 30%, which is consistent with the principle that the workpiece containing harder inclusions lead to a greater mechanical component of crater wear. However, it is emphasized that this observation represents the results of only one wear test carried out at each cutting speed. More cutting tests should be carried out to establish the effect of hard inclusions on mechanical wear in a quantitative manner. The volume fraction of hard inclusions in steel 2 should be sufficiently high to result in a significant difference in the two mechanical wear rates.

CHAPTER 7 : CONCLUSIONS

1) A quantitative database on cutting tool wear has been generated by activating the chips produced during cutting and measuring the concentration of tungsten present by Instrumental Neutron Activation Analysis. Activation of the chips is safer and more convenient than the use of radioactive tools to generate a similar database.

2) During the high speed machining of Ca-treated AISI 1045 steel using K-11 grade (97% WC) tools, crater wear, rather than the flank wear is dominant. At a cutting speed of 150 m/min, the total tool loss was equal to 444± 97 μg, of which only 11 μg loss resulted from flank wear. This dominance became particularly pronounced at a cutting speed 240 m/min, where the flank wear contributed only 52 μg to a total tool wear of 3708± 158 μg.

3) Dissolution wear is the dominant micromechanism responsible for crater wear of K-11 grade cemented carbide tools during high speed machining of medium carbon steel. At a cutting speed of 150 m/min, the percentage contribution of dissolution wear to the total amount of crater wear was equal to 66.4%. With an increase in cutting speed to 240 m/min, the contribution of dissolution wear mechanism increased to 93.4% of the total crater wear.

4) Dissolution wear data conforms to an Arrhenius type relationship. The value of the activation energy for the process derived from the experimental data is equal to 207±44 kJ/mol.

5) SIMS analysis of the regions next to the tool-chip interface of water quenched chips showed concentration profiles of tungsten and cobalt. Instantaneous dissolution wear amounts calculated from the results of SIMS analysis are consistent with the INAA results.

6) The operative diffusion coefficient of tungsten in the immediate vicinity of the tool-chip interface is greatly enhanced, e.g. at a cutting speed of 150 m/min, it is found to be 179 times higher than the lattice diffusion coefficient. The significant increase in the grain boundary area of the chip material next to the interface partly explains the enhancement in the diffusivity of tungsten, e.g. the effective diffusion coefficient of tungsten with 0.2 μm grain size is found to be 17 times higher than the lattice diffusion coefficient.

7) Thermokinetic models of dissolution wear predict amounts which fall short of the experimentally measured values, e.g. the amount predicted by a model based on complete austenitization and 0.2 μm grain size in the immediate

vicinity of the tool-chip interface at 240 m/min accounts for 34.7 % of the experimentally measured values. It is proposed that dissolution wear may be totally accounted for by a thermokinetic model, based on further diffusion enhancement by grain boundary migration and/or the presence nm size grains during the tool-chip contact time.

8) The experiments performed at a cutting speed of 240 m/min using HfN coated tool showed that the average tool-chip interface temperatures were lower by about 75 ^{o}C than those reached when an uncoated tool was used under the same conditions. Increase in the concentration of hafnium and tungsten in the collected chips was found to be less than 0.7 ppm, which was the detection limit of the technique.

9) The normalized mechanical wear rates of the K-11 grade tools were increased by about 30% at the two speeds examined (180 m/min and 220 m/min) when the Ca-treated AISI 1045 grade steel workpiece was changed to the AISI 1045 grade steel workpiece produced without calcium treatment.

APPENDIX I : CALCULATIONS OF AVERAGE INTERFACE TEMPERATURE

The cutting force (F_C), the feed force (F_T) and the radial force (F_R) were measured using a dynamometer. The following equations hold good for semi-orthogonal [1] metal cutting operation:

Force in the XY Plane (F_{XY}):

$$F_{XY} = \sqrt{(F_T^2 + F_R^2)} \qquad (I.1)$$

Cutting Ratio (r):

$$r = t_1/t_2 \qquad (I.2)$$

where, t_1 is the thickness of the uncut layer.

t_2 is the chip thickness.

Shear Angle (ϕ):

$$\tan \phi = \frac{r \cdot \cos \alpha}{1 - r \cdot \sin \alpha} \qquad (I.3)$$

where, α is the rake angle

Shear Plane Force (F_S):

$$F_S = F_C \cdot \cos \phi - F_{XY} \cdot \sin \phi \qquad (I.4)$$

Normal Rake Face Force (N):

$$N = F_C \cdot \cos \alpha - F_{XY} \cdot \sin \alpha \qquad (I.5)$$

Shear Rake Face Force (F):

$$F = F_c \cdot \sin\alpha + F_{XY} \cdot \cos\alpha \qquad (I.6)$$

Thermal Number (R_T):

$$R_T = \rho \cdot c \cdot v \cdot t_1 / k \qquad (I.7)$$

where, ρ is the density of the workpiece material,

c is the sp. heat of the workpiece material,

v is the cutting speed,

t_1 is the uncut chip thickness, and

k is the thermal conductivity of the workpiece.

Based on the study of the temperature distributions obtained from the Boothroyd model, the following empirical relationships [23] have been proposed:

The Fraction of Heat Conducted in the Workpiece (β):

$$\beta = 0.5 - 0.35 \log(R_T \tan\phi) \text{ for } 0.04 \le R_T \tan\phi \le 10 \qquad (I.8)$$

$$\beta = 0.3 - 0.15 \log(R_T \tan\phi) \text{ for } R_T \tan\phi > 10 \qquad (I.9)$$

The Average Temp. Rise in Primary Shear Zone (ΔT_{PZ})

$$\Delta T_{PZ} = \frac{(1-\beta) \cdot F_S \cos\alpha}{\rho \cdot c \cdot t_1 \cdot w \times \cos(\phi - \alpha)} \qquad (I.10)$$

where, w is the width of cut.

The Average Temp. Rise in the Chip Body (ΔT_C)

$$\Delta T_C = \frac{F \sin\phi}{\rho \cdot c \cdot t_1 \cdot w \cdot \cos(\phi - \alpha)} \qquad (I.11)$$

Boothroyd's results can be represented by the following equation:

$$\log\left(\Delta T_M/\Delta T_C\right) = 0.06 - 0.195\cdot\delta\sqrt{\left(R_T\cdot t_2/h\right)} + 0.5\log\left(R_T\cdot t_2/h\right) \qquad (I.12)$$

where, ΔT_M is the maximum temp. rise in the chip

δ is the ratio of the thickness of the secondary shear zone to the chip thickness, t_2

The Average Interface Temperature (T_{avg})

$$T_{avg} = T_o + \Delta T_{PZ} + \psi\cdot\Delta T_M \qquad (I.13)$$

where, T_o is the room temperature

ψ is an empirically determined parameter

The following empirical equations proposed by Mathew[23] were used in the calculation of ψ :

$$\left.\begin{array}{ll} \psi = 1.0 & \text{for } t_1 \leq 0.1 \text{ mm} \\ \psi = 1.075-0.75t_1 & \text{for } 0.1\text{mm} \leq t_1 \leq 0.5\text{mm} \\ \psi = 0.7 & \text{for } t_1 \geq 0.5\text{mm} \end{array}\right\} \qquad (I.14)$$

For the value of t_1 used in this study, ψ = 0.94. The average interface temperatures during a wear test conducted at 150 m/min are given in Table 5.1.

Appendix II

Effect of Surface Roughness on Depth Profiling

It is well known that the surface roughness of the sample influences the depth profiling process in SIMS[95]. The amplitude of perturbation corresponding to a given surface roughness and its wavelength, together, determine the degree of severity of the influence of surface roughness on the depth resolution achieved during depth profiling. A rough surface leads to differential sputtering on primary ion bombardment and thus, degrades the depth resolution . In addition, a polycrystalline sample has its grains oriented differently with respect to the oncoming primary ions, which also leads to differential sputtering thereby degrading the depth resolution.

Fig.II.1(a) and (b) are the typical chip surface topographies obtained using a high precision Alfa-Step profilometer. Fig.II.2 shows a three dimensional image of the chip surface obtained using the Atom Force Microscope. The amplitude of the surface perturbation is seen to be about 0.1 μm, whereas the wavelength is about 10 μm. Based on these values of the amplitude and the wavelength of the surface perturbations, it can be concluded that the surface peaks are not sharp, and consequently the degradation of

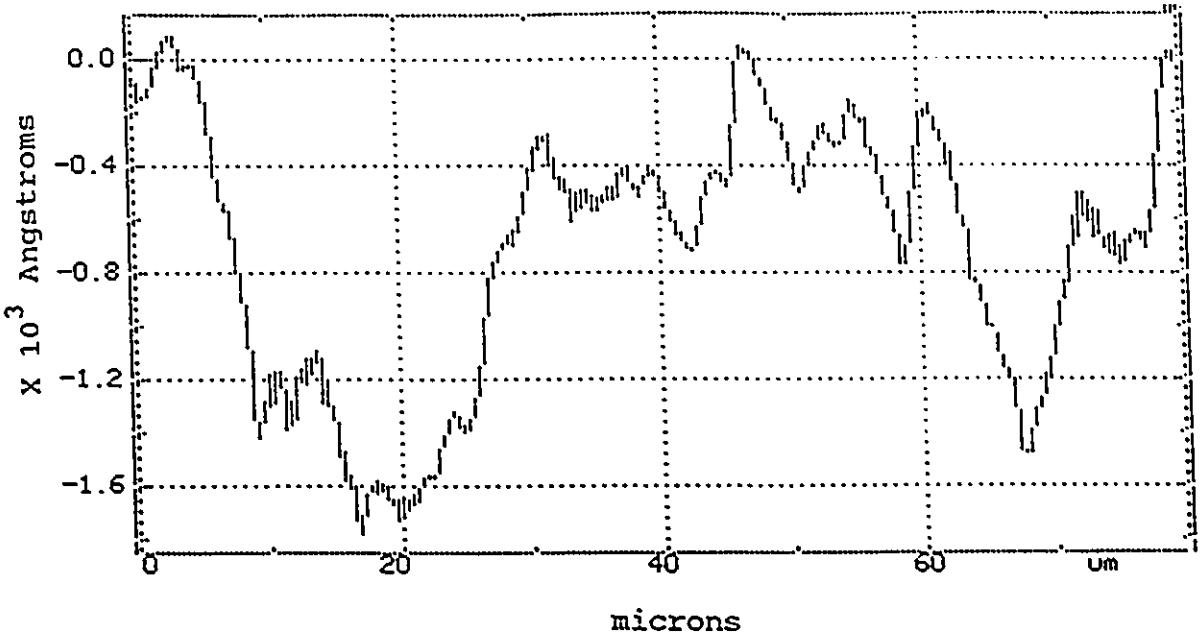

(a) 80 μm scan

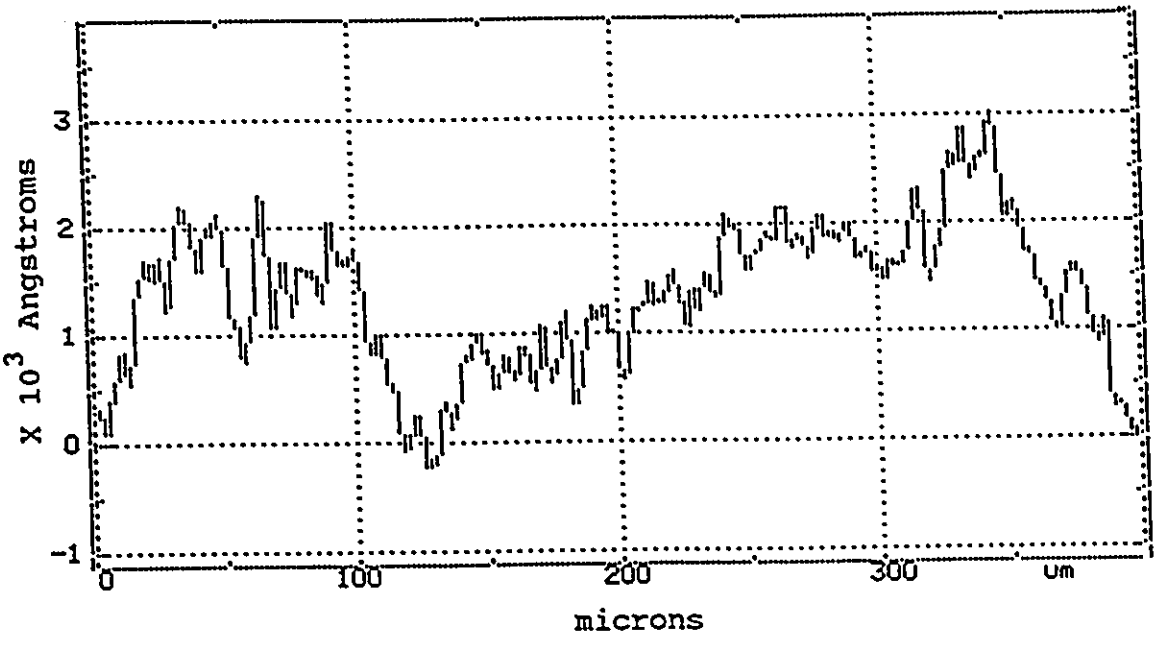

(b) 400 μm scan

Fig.II.1 Typical chip surface topography.

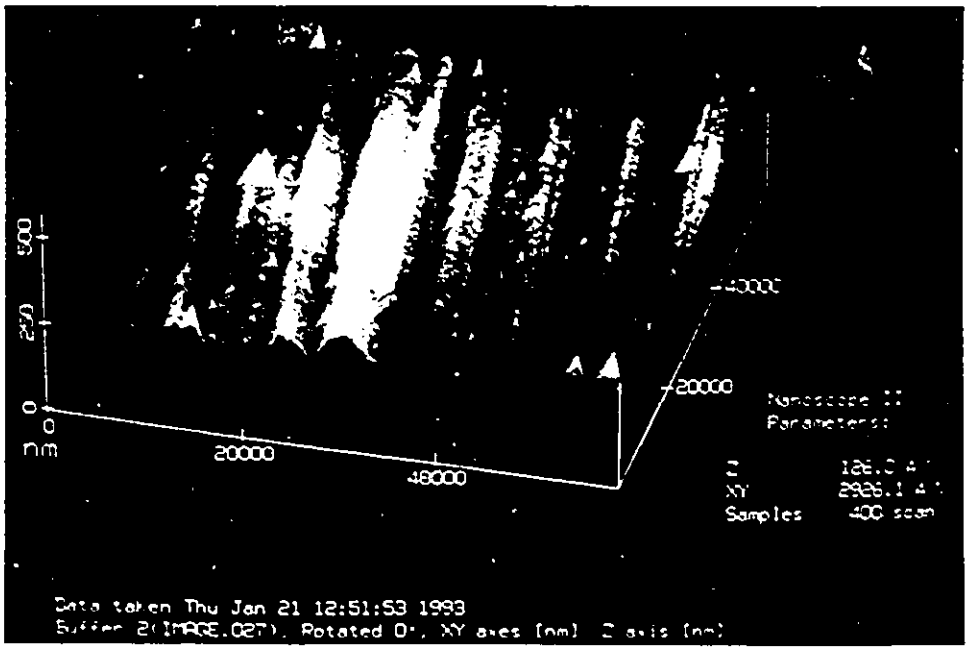

Fig.II.2 An image of the chip surface obtained by the Atom Force Microscope

depth resolution due to differential sputtering is expected to be very mild. Secondary ions were collected from a circular area of 60 μm diameter and fed to the mass spectrometer. Thus, the size of the analyzed area was also very much larger than the size of surface asperities. Grain diameter in the secondary shear zone next to the interface was previously shown to be in the sub-micron range. Thus, more that 100 grains in the chip were sputtered simultaneously. The effect of differential sputtering due to differences in grain orientation with respect to the incident beam is averaged out by this large number, and hence the degradation of depth resolution in this case is small.

During SIMS analysis, the primary ions were bombarded on the sample at 30 degrees to the surface normal. Depth resolution achieved during the analysis of a flat and well polished sample was measured and was found to be better than 10 nm. A higher estimate of the degradation in depth resolution due to roughness of the given chip samples is up to about 50% of this value. Thus, a depth resolution of better than 15 nm is expected during analysis, and changes in concentration measured beyond this depth can be considered to be solely due to the true profile itself. In the present case, depths of penetration of tungsten in the chips were about 0.4-0.5 μm. Based on these values, it can

be concluded that the experimentally measured profiles represent the true concentration profiles of tungsten in the chips.

REFERENCES

1) Bhattacharyya, A., METAL Cutting : Theory and Practice : Central Book Publishers, Calcutta. (1984)

2) Doyle, E.D., Horne, J.G. and Tabor, D., Proc.Roy.Soc., A366, 173 (1979)

3) Kececioglu, D., Trans.ASME, Vol.80, No.1, p.158, (1958)

4) Hastings, W.F., Annals of CIRP., Vol.XV, p.109 (1967)

5) Loladze, T.N., Mashgiz, Moscow (1952)

6) Williams, J.E., Smart, E.F. and Milner, D.R., Metallurgia, 81, 6, (1970)

7) Brown, R.H and Komanduri, R., Proc. 13th Ann. Mach. Tool Des.Res.Conf., Birmingham, (1972)

8) Piispanen, V, J.Appl.Phy. Vol.19, No.10, p876, (1948)

9) Okushima, K. and Hitomi, K., Mimoirs of the Faculty of Engineering, Kyoto University, Vol.20, No.2, (1958)

10) Oxley, P.L.B. and Welsh, M.J.M., Proc. 4th Ann. Mach. Tool Des. Res. Conf., Birmingham, (1963)

11) Trent, E.M., Wear, 128, pp 47-64, (1988)

12) Rogers, H.C., Ann. Rev. Mater. Sci. p.283 (1979)

13) Shelbourn, A.M., Roberts, W.T. and Trent, E.M., Materials Science and Technology, p.220 (1985)

14) Hau-Bracamonte, J.L., Metals Technology, p.447, (1981)

15) Boothroyd, G., Proc. Instn. Mech. Engrs. Vol.177, No.29 p.789, (1963)

16) Merchant, M.E., J.Applied Mechanics, Trans. ASME, Vol.2, p. A168, (1944)

17) Zorev, N.N., Metal Cutting Principles, Pergamon Press, (1966)

18) Micheletti, G.F., DeFilippi, A., and Ippolito, R., Annals of the CIRP, Vol.XVI, pp.353-360 (1968)

19) DeFilippi, A., and Ippolito, R., Annals of the CIRP, Vol.XVII, pp.377-385 (1969)

20) Trent, E.M., Metal Cutting, Butterworths, (1991)

21) Brown, C.A., Metallography, 20: 465-483 (1987)

22) Taylor, F.W., Trans. ASME, Vol.28, p.31 (1907)

23) Mathew, P., Int.J.Mach.Tools Manufact., Vol.29, No.4, p.481, (1989)

24) Trigger, K.J., Trans. ASME, Vol.70, p.91 (1948)

25) Kusters, K.J. Dissertation, T.H. Aachen (1956)

26) Bickel, E., Int.Res.Prod.Eng., ASME, New York, (1963)

27) Wright, P.K. and Trent, E.M., J.Iron and Steel Inst., p.364, (1973)

28) Dearnley, P.A. and Trent, E.M., Metals Technol., 9(2), 60 (1982)

29) Rapier, A.C., Brit. J. Appl. Phy., Vol.5, p.400 (1954)

30) Tay, A.O., Stevenson, M.G. and Davis, G.de V., Proc. Instn. Mech. Engrs., 188, 627, (1974)

31) Tay, A.O., Stevenson, M.G., Davis, G. de V., and Oxley, P.L.B., Int.J.Mach.Tool Des.Res. Vol.16, p.335 (1976)

32) Hastings, W.F., Mathew, P., Oxley, P.L.B. & Taylor, D., Proc. 20th Int.Mach.Tool.Des.Res.Conf., p.313 (1979)

33) Shaw, M.C., Metal Cutting Principles, Oxford, (1984)

34) Usui, E., Shirakashi, T. and Kitawaga, Wear, 100, p.129 (1984)

35) Wright, P.K., Horne, J.G. and Tabor, D. Journal of Wear, Vol.54, p.371, (1979)

36) Trent, E.M., ISI Report No 94, pp. 11, 77, 179 (1967)

37) Ramalingam, S. and Wright, P.K., J.Engineering Materials and Technology, 103(2):151-156 (1981)

38) Sigl, L.S. and Fischmeister, H.F., Acta Metallurgica, Vol.36, No.4, pp.887-897 (1988)

39) Brandt, G., Wear, 112, pp.39-56 (1986)

40) Evans, A.G. and Charles, E.A., J.Amer.Cer.Soc., Vol. 59, pp.7-8 (1976)

41) Brandt, G. and Mikus, M., Wear, 118, pp 99-112 (1987)

42) Milovic, R., Ph.D. Thesis, University of Birmingham, UK. (1983)

43) Milovic, R. and Wallbank, J., J. Appl. Metalworking, 2(4), 249 (1983)

44) Loladze, T.N., Journal of Institution of Engineers (India), Vol.43, No.3, (1962)

45) Bhattacharyya, A. and Ghosh, A., Proc. 5th Int. Mach. Tool Des. Res. Conf. (1962)

46) Naerheim, Y. and Trent, E.M., Metals Technol, 4(12), 548 (1977)

47) Kramer, B.M. and Suh, N.P., J. Engineering for Industry, Vol. 102, p.303, (1980)

48) Takeyama, H. and Murata, R., Trans. ASME, Series B, J. Engineering for Industry, 85, 33 (1963)

49) Kramer, B.M., Ph.D. Thesis, MIT, USA (1979)

50) Van Vlack, L.H., Trans. ASM, Vol.45, p.741 (1953)

51) Stevenson, M.G. and Duncan, K.R., Journal of the Iron and Steel Institute, p.710, (Oct. 1973)

52) Richardson, B.D. and Chisholm, A.W., Proc. IME, 129, (1965)

53) Trent, E.M., The Iron and Steel Institute, London, 77, (1967)

54) Williams, J.E. and Rollason, E.C., J. Inst. Met., 98, 144, (1970)

55) Wilber, W.J. et al., proc. 12th Int. Mach. Tool Des. Res. Conf., paper 208, (1971)

56) Dines, B.W., Ph.D. Thesis, University of Birmingham, UK. (1975)

57) Fenton, R.G. and Oxley, P.L.B., Proc.IME, 184, 927 (1969-70)

58) Naylor, D.J., Llywellyn, D.T. and Keane, D.M., Metals Technology, 3(5,6), 254 (1976)

59) Opitz, H., Gappisch, M., Konig, W., Pape, R. and Wicher, A., Arch. Eisenhuttenwesen, 33, 12 pp.841-851, (1962)

60) Kay, D.A.R., Subramanian, S.V., Sowerby, R. and Chandrasekaran, N., 'Metallurgical Aspects of

Machinability in Medium Carbon Steels', D.S.S. File No. 205T-23440-5-9055, October 1987

61) Narutaki, N and Yamane, Y., J.JSPE, 48, 4, p.463 (1982)

62) Wicher, A. and Pape, R., Stahl und Eisen, 20, p.1169, 87 (1967)

63) Helisto, P., Helle, A.S. and Pietikainen, J., Wear, 139, pp. 225-234 (1990)

64) Subramanian, S.V., Kay, D.A.R., Chandrasekaran, N. and Sowerby, R., Proc. ASM Int. Conf. on 'Strategies for Automation of Machining : Materials and Processes', Orlando, Florida (1987)

65) Properties and Uses of Kennametal Tools : Kennametal Catalogue (1987)

66) Lai, C.T., M.Eng. Thesis, McMaster University, Hamilton, Ontario (1986)

67) Parry, S.J., Activation Spectrometry in Chemical Analysis, Wiley Publication, New York. (1991)

68) Westphal, G.P., Radioanalytical Chem., 70, 387 (1982)

69) Westphal, G.P. in ND599 Loss Free Counting Module Operator's Manual, Nuclear Data Inc., (1987)

70) Williams, P., Ann. Rev. Mater. Sci., 15: 517-548 (1985)

71) Trent, E.M., J.Iron and Steel Inst., p.847 (1963)

72) Urhenius, B. in Hardenability Concepts with Applications to Steels, Editors : Doanne, D.V. and Kirkaldy, J.S. (1977)

73) Fridberg, J., Torndahl, L.E. and Hillert, M., Jernkont. Ann. 153, p.263 (1969)

74) Zeminsky, S.V. and Kupalova, I.K., Phys. Met. Metallogr. 27(2), 315 (1969)

75) Kaur, I., Gust, W. and Kozma, L., Handbook of Grain and Interphase Boundary Diffusion Data, Vol.2, Ziegler Press, Stuttgart (1989)

76) Lunde, G. and Anderson, P.B., Int. J. Mach. Tool Des. Res., Vol.10, pp.79-93 (1970)

77) Chawla, R. and Bhattacharya, S.L., Wear, 43, p.175 (1977)

78) Handbook of Chemistry and Physics, 53rd edition, Chem. Rubber Book, New York. (1972)

79) Flom, D.G., Komanduri, R. and Lee, M., Ann. Rev. Mater. Sci., 14: 231-278 (1984)

80) Wright, P.K., Bagchi, A. and Horne, J.G. in Cutting Tool Materials, ASM

81) Cook, N.H., Journal of Engineering for Industry, p.931 (1973)

82) Akasawa, T., Hashiguti, Y. and Suzuki, K., Wear, 65, pp.141-150 (1980)

83) Private Communication from Dr.E.M. Trent (1992)

83-b) Von Fraunhofer, J.A. and Pickup, G.A.: in High Temperature Materials Coatings and Surface Interaction, pp.5-45, Freund Publishing House, Tel-Aviv (1980)

84) Wingrove, A.L., J. Aust. Inst. Met. 16: 67-70 (1971)

85) Usui, E., Shirakashi, T. and Kitawaga, T., Journal of Engineering for Industry, Vol.100, p.236 (1978)

86) Buckley, D.H., Prog. Surf. Sci., 12(1): 1-153 (1982)

87) Ferrante, J., Acta. Metall., 19, p.743 (1971)

88) Kirkaldy, J.S. and Young, D.J., Diffusion in the Condensed State, The Institute of Metals (1987)

89) Shewmon, P.G., Diffusion in Solids, 2nd edition, TMS Publication. (1989)

90) Hillert, M. and Purdy, G.R., Acta Metallurgica, Vol. 26, pp.333-340 (1978)

91) Olander, D.R. and El-Saied, U.M., Acta Metallurgica, Vol.40, No.6, pp.1329-1336 (1992)

92) Zorev, N.N., Mashgiz, Moscow (1952)

93) Balasubramanian, K., Unpublished Work, (1985)

94) Narita, K., Trans. ISIJ, Vol.15, pp.145-151 (1975)

95) Briggs, D. and Seah, M.P., Practical Surface Analysis , by Auger and X-Ray Photoelectron Spectroscopy, Wiley Publications, New York (1983)

96) Kurimoto, T. and Barrow, G., Annals of CIRP, 31,(1), 19, (1982)